Mechanical Control of Quantum Transport in Single-wall Carbon Nanotubes

Linxiang Huang

A Thesis
In the Department
of
Physics

Presented in Partial Fulfillment of the Requirements
For the Degree of
Doctor of Philosophy (Physics) at
Concordia University
Montréal, Québec, Canada

November 2025

Concordia University
School of Graduate Studies

This is to certify that the thesis prepared

By: **Linxiang Huang**

Entitled: **Mechanical Control of Quantum Transport in Single-wall Carbon Nanotubes**

and submitted in partial fulfillment of the requirements for the degree of

Doctor of Philosophy (Physics)

complies with the regulations of this University and meets the accepted standards with respect to originality and quality.

Signed by the final examining commitee:

_____ Chair
Dr. Louis Cuccia

_____ External Examiner
Dr. Thomas Szkopek

_____ Arms-Length Examiner
Dr. Pat Forgione

_____ Examiner
Dr. Saurabh Maiti

_____ Examiner
Dr. Ingo Salzmann

_____ Supervisor
Dr. Alexandre Champagne

Approved by _____
Dr. Saurabh Maiti, Graduate Program Director

Dec. 17, 2025 _____
Dr. Pascale Sicotte, Dean of the Faculty of Arts and Science

Abstract

Mechanical Control of Quantum Transport in Single-wall Carbon Nanotubes

Linxiang Huang, Ph.D.
Concordia University, 2026

Single-wall carbon nanotubes (SWCNTs) are narrow ribbons of graphene with atomically precise boundary conditions and a single quantum transport channel at realistic dopings. Together with their extreme mechanical strength, wide elastic deformation range, and strong electron-mechanical coupling, these properties make them ideal systems to harness quantum transport straintronics (QTS), i.e. using mechanical strain to control quantum transport.

We first adapted an applied theoretical model to study QTS in uniaxially strained quasi-metallic-SWCNT transistors. Mechanical strain adds both scalar ϕ_ε and vector $\boldsymbol{A}$ gauge potentials to the transistor's Hamiltonian. We demonstrate that these potentials tune the charge carriers' propagation angle (the helix angle with respect to the nanotube axis) and create a rich spectrum of quantum interferences in conductance, which can be described as a mechanical Aharonov-Bohm effect. The charge carriers' quantum phase can be controlled by purely mechanical means.

We then fabricated suspended SWCNT transistors with channel lengths of $\approx$ 30 nm and acquired QTS data over a broad range ($\approx$ 0 to 4 %) of *in-situ* tunable and reversible uniaxial mechanical strain. We analyze these detailed charge transport data showing a large mechanical-gating effect of the SWCNT quantum dots (QDs). The precise reversibility of the data, and their agreement with QTS theory, confirm that the nanotubes are strained elastically. We demonstrate that this mechanical control of the QD doping is not due to capacitive-gating effects, but to predictable bandstructure changes described by ϕ_ε and $\boldsymbol{A}$.

We also present measurements of quantum transport in strained graphene transistors that agreed quantitatively with models based on ϕ_ε and $\boldsymbol{A}$. Finally, we observed strain-tunable electro-mechanical coupling in both graphene and SWCNT mechanical oscillators.

Our work opens new opportunities to harness quantitative strain effects in quantum transport of low-dimensional materials and could find applications in qubits, oscillators and other quantum devices.

Acknowledgements

I would not have been able to complete my PhD without persistence, and the support of my supervisor and colleagues.

I would first like to thank myself for the effort and time devoted to this research project. I worked through many long nights and weekends, at home, in the lab, the cleanroom, and the office, when it felt as though there was only the research and myself. This kind of complete focus is a gift available only for a limited time, as there will be many more responsibilities beyond research in the future.

I would then like to thank my supervisor, Dr. Alexandre Champagne, for his guidance and support. He guided me through the research project and shared his philosophy of dealing with challenges both in research and in life. I am truly grateful to have had the opportunity to be supervised by him and to grow under his mentorship.

I would also like to thank my colleagues, particularly Israel, Amin, Rami, and Wyatt. It was a pleasure working with them during my PhD journey, and I greatly appreciated their professionalism and kindness.

Every journey eventually comes to an end, and this thesis marks the end of my PhD. I wish all of us a wonderful journey ahead in our lives.

Contribution of Authors

This section clarifies my individual contributions to the research presented in this thesis, following the order of the chapters.

In Chapter 2, I adapted an existing applied theory of ballistic charge transport in strained graphene to extend it to strained single-wall carbon nanotubes (SWCNTs). The major changes and additions addressed the new boundary conditions, one-dimensional band structures, quantum capacitance, and tube chiralities. I calculated ballistic transport in SWCNTs of different chiralities under varying uniaxial strain and using realistic experimental parameters. I demonstrated the impacts from the strain-induced scalar and vector potentials on the charge carriers' propagation angle (the helix angle with respect to the tube's axis) in the SWCNT channel and predicted a mechanical Aharonov-Bohm effect, leading to a rich spectrum of quantum interferences in SWCNT conductance. This work was published in Physical Review Applied, and I am the lead (first) author of the paper: L. Huang *et al., Quantum transport straintronics and mechanical Aharonov–Bohm effect in quasimetallic single-wall carbon nanotubes*, Physical Review Applied **23** (1), 014030 (2025).

In Chapter 3, I applied and refined previous fabrication techniques developed in our research group to build suspended SWCNT quantum dot (QD) transistors and packaged them for use in a quantum transport straintronics (QTS) platform established by our previous group members, particularly Andrew McRae. I carried out the fabrication steps, including locating and identifying SWCNTs, aligning and depositing Au clamps, suspending junctions, wire-bonding devices, and loading the devices. I improved some fabrication recipes, such as e-beam lithography, wire-bonding, and chip loading, to achieve higher precision and yield. I created strain-tunable SWCNT-QDs for first time in the physics community, to the best of my knowledge, providing new opportunities to explore QTS in SWCNTs and other low-dimensional materials.

In Chapter 4, I acquired all charge transport data presented for the SWCNT-QDs over a broad range of *in-situ* tunable and reversible uniaxial strain. I then organized and analyzed these data to study the mechanical control of quantum transport in SWCNT-QDs.

I demonstrated that strain tunes the QD doping (mechanical gating) and confirmed that this originates from predictable strain-induced scalar and vector potentials rather than from capacitive-gating effects. This work is in the final stage of submission for publication and I am the lead (first) author: L. Huang *et al., Experimental straintronics in nanotube quantum dots*, to be published (2025).

In Chapter 5, I calculated ballistic transport data for uniaxially strained graphene and contributed to the paper published in Advanced Materials: A. C. McRae, G. Wei, and L. Huang *et al., Mechanical Control of Quantum Transport in Graphene*, Adv. Mater. **36** (23), 2313629 (2024). I acquired and analyzed the data showing strain-tunable electromechanical resonances and electron-vibron coupling in SWCNT-QDs. I also fabricated strain-tunable graphene QDs, where similar transport driven electromechanical resonances were observed. My colleagues, Israel and Amin, acquired the data for the graphene QDs and will continue the data analysis. I anticipate to be a co-lead author of the forthcoming paper on this work.

Contents

List of Figures

List of Tables

List of Abbreviations

1DMs	One-dimensional Materials.
2DMs	Two-dimensional Materials.
AFM	Atomic Force Microscopy.
BC	Boundary Condition.
BOE	Buffer Oxide Etch.
CNT	Carbon Nanotube.
CVD	Chemical Vapour Deposition.
EBL	E-beam Lithography.
FBZ	First Brillouin Zone.
FP	Fabry-Pérot.
H.c.	Hermitian Conjugate.
NN	Nearest-Neighbor.
NNN	Next-Nearest-Neighbor.
QD	Quantum Dot.
QTS	Quantum Transport Straintronics.
SEM	Scanning Electron Microscopy.
SWCNTs	Single-wall Carbon Nanotubes.
TMDs	Transition Metal Dichalcogenides.

Chapter 1

Introduction to Quantum Transport Straintronics (QTS) in SWCNTs

Precise control of quantum transport in low-dimensional materials allows the manipulation of quantum phases and charge conductance that are crucial for both fundamental research and emerging quantum technologies. Achieving such an experimental control and quantitative agreement with theory requires exceptionally low and uniform disorder across an entire device [1,2]. While such control over electrostatic dopant disorder has been achieved [3], comparable mastery has not yet been attained for mechanical disorder (strain-field disorder) [4] in most one-dimensional materials (1DMs/nanotubes) and two-dimensional materials (2DMs). The field of quantum-transport straintronics (QTS) aims to both mitigate the disruptive effects of uncontrolled strain fields on quantum transport and exploit precisely engineered strain fields in 2DMs and nanotubes to tune their properties, including band gap, charge doping, potentials, and quantum phases. The QTS approach offers broad opportunities to advance quantum technologies (e.g., qubits [5–10], spintronics [11–16], and valleytronics [17–20]) and to explore many-body quantum phases (e.g., superconductivity [21–23], topological transitions [21, 24–29], and magnetic transitions [30–32]).

Ideal quantum-straintronics transistors would permit complete control of both the magnitude and phase of their quantum current, mechanically as well as electrostatically, i.e. a full electro-mechanical control of the electrons' Hamiltonian. Graphene and single-wall carbon nanotubes (SWCNTs) are particularly promising due to their exceptional mechanical and electronic properties. They exhibit remarkable mechanical strength and a wide elastic deformation range [1, 20, 33, 34], originating from the sp^2 bonds between neighboring carbon atoms. Their Hamiltonian is straightforward to describe because of their simple honeycomb lattice composed solely of carbon atoms. SWCNTs, in particular, possess perfect periodic boundary conditions (i.e. zero edge disorder) and allow ultra-short channel lengths, enabling

large strain tunability in experiments. Their few-nanometer diameter results in a large energy spacing between sub-bands. This confines transport to a single channel with four-fold degeneracy, making it much easier to identify and interpret the effects of mechanical strain on the Hamiltonian and transport.

While there are many exciting theoretical proposals in QTS of SWCNTs [21, 29, 35], experimental progress has been slow. Two major challenges are, which we will address in this thesis, the lack of a realistic quantum-transport model for strained SWCNTs, and the absence of an experimental platform that enables *in-situ* tuning of uniaxial mechanical strain and low-temperature quantum transport measurements.

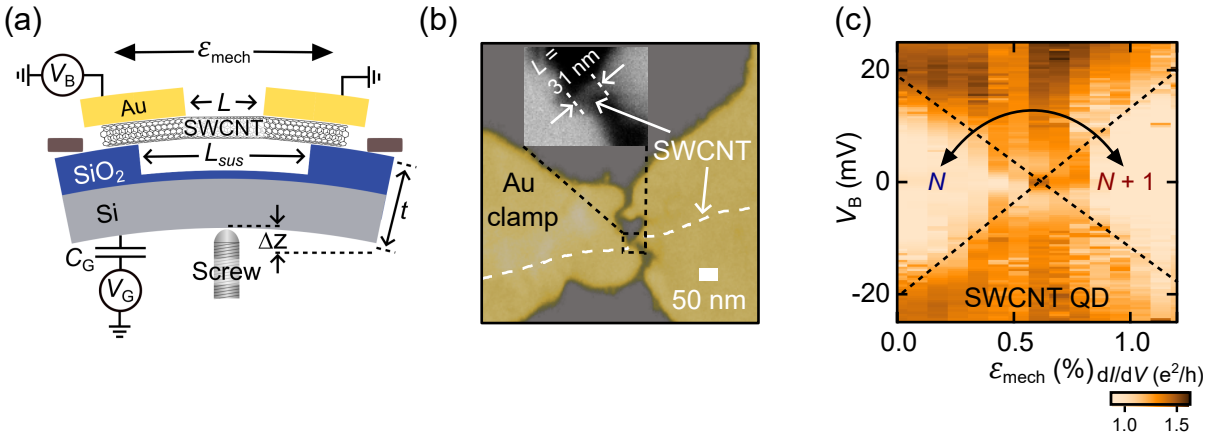

Figure 1.1: Our experimental platform and representative QTS data in SWCNTs. (a) A push screw bends the Si substrate, applying a mechanical strain $\varepsilon_{\text{mech}}$ to the suspended SWCNT channel. Transport measurements are performed using a standard DC circuit. (b) Top-view of a SWCNT device with a channel length of $\approx$ 30 nm (inset). The white dashed line marks the position of the SWCNT beneath the Au electrodes. (c) Mechanical strain tunes the doping level in the SWCNT channel, switching the average electron number between N and $N + 1$.

To bridge the gap between theory and experiment, we first adapted an existing model to study quantum transport in uniaxially strained SWCNT transistors [36]. We used realistic device parameters based on our experimental platform, as illustrated in Fig. 1.1(a). We demonstrated that strain can control the charge carriers' trajectories in the channel. It also modulates their quantum interferences, which was interpreted as a mechanical Aharonov–Bohm effect. We then fabricated suspended SWCNT transistors with channel lengths of $\approx$30 nm, as shown in Fig. 1.1(b), and performed transport measurements over a broad range of *in situ* tunable and reversible uniaxial strain. Figure 1.1(c) shows that strain could tune the

doping level in a SWCNT-QD. This mechanical gating originates from predictable strain-induced scalar and vector potentials and could find applications in nanotube-based qubits [6] and quantum devices [7], as well as provide a reliable way to gate single-molecule electronic devices [37].

In this chapter, we first review recent literature progress in QTS for SWCNTs and graphene. We then briefly summarize our key results and conclude by outlining the organization of this thesis.

1.1 Recent literature review of QTS

In this section, we review recent theoretical proposals and experimental platforms for quantum transport in strained SWCNTs and graphene. We then present the latest experimental results in this field.

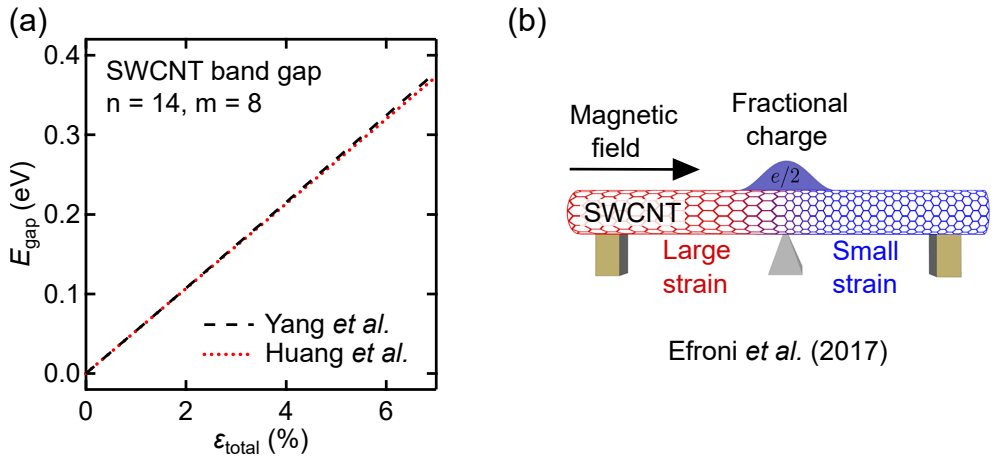

Figure 1.2: Selected QTS applications in SWCNTs. (a) Strain opens a band gap in a quasi-metallic SWCNT. Figure adapted from Refs. [38, 39]. (b) A wedge-shaped pillar placed beneath a quasi-metallic carbon nanotube produces different strain on the left and right sides of the pillar. When an axial magnetic field is applied, a fractional charge forms in the middle region. Figure adapted from Ref. [29].

There are many exciting theoretical proposals about QTS in nanotubes and 2DMs [13, 18, 21, 29, 33–35]. For instance, a tunable uniaxial strain could open a band gap in a quasi-metallic SWCNT, as shown in Fig. 1.2(a). Fabricating two regions of a quasi-metallic SWCNT with different strain (e.g., by placing a pillar beneath the nanotube) can induce topological transitions and fractional charges in the presence of an axial magnetic field, as illustrated in Fig. 1.2(b). Graphene conductance could be reduced to zero using mechanical

strain without creating a bandgap (Fig. 1.3(a)), resulting in graphene quantum strain transistors [36]. By stretching only the top layer of a twisted magic-angle bilayer graphene, as shown in Fig. 1.3(b), one could tune its superconducting and flat-band physics [40].

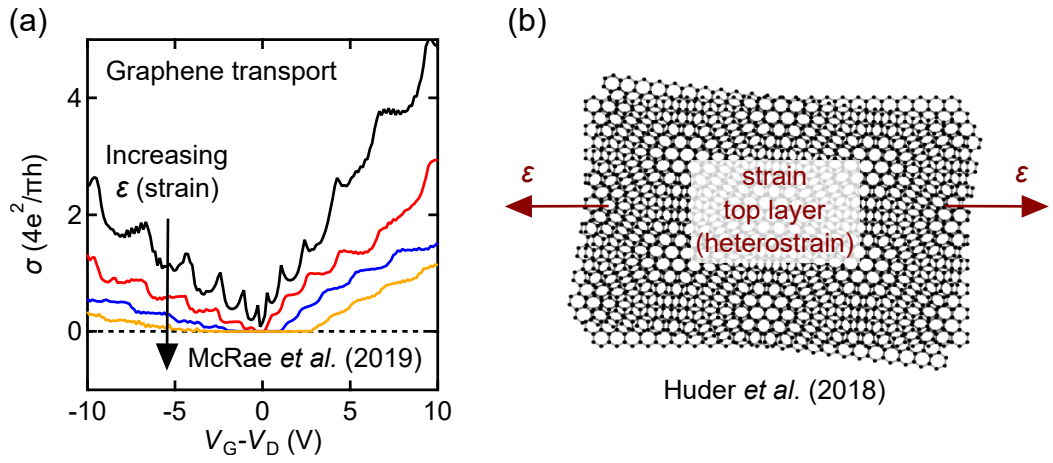

Figure 1.3: Selected QTS proposals in graphene. (a) With an increase of strain, conductance of graphene decreases to zero without creating a bandgap. Figure adapted from Ref. [36]. (b) Heterostrain in a twisted bilayer graphene, i.e. only the top layer is being stretched, could tune flat band physics. Figure adapted from Ref. [40].

However, very few experiments successfully realized these proposals [42–44]. One major reason is the lack of an experimental platform with *in situ* tunable mechanical strain suited for low-temperature quantum transport measurements.

Four existing QTS platforms are shown in Fig. 1.4. Panel (a) shows that AFM tips can be used to fold a graphene layer [41], thereby creating strain in the folded region. This method is not reproducible, and only local transport measurements with fixed strain can be performed in graphene. By pushing an AFM tip on a suspended nanotube [42], varying strains can be applied and room-temperature transport measurements can be performed, as shown in panel (b). However, the strain is non-uniform and cannot be calibrated precisely. A strain cell based on three parallel piezo stacks has been developed to apply strain to materials placed on a gapped substrate mounted on top of the flexure [30, 45]. While this platform allows in-situ uniaxial strain, it is not compatible with quantum-transport measurements but is used for optical measurements. Panel (d) employs a three-point bending setup to stretch an encapsulated graphene device [43]. The main drawback of this platform is the strain disorder from the substrate and the limited strain range, which restricts the quantitative and extensive observation of strain effects on graphene transport.

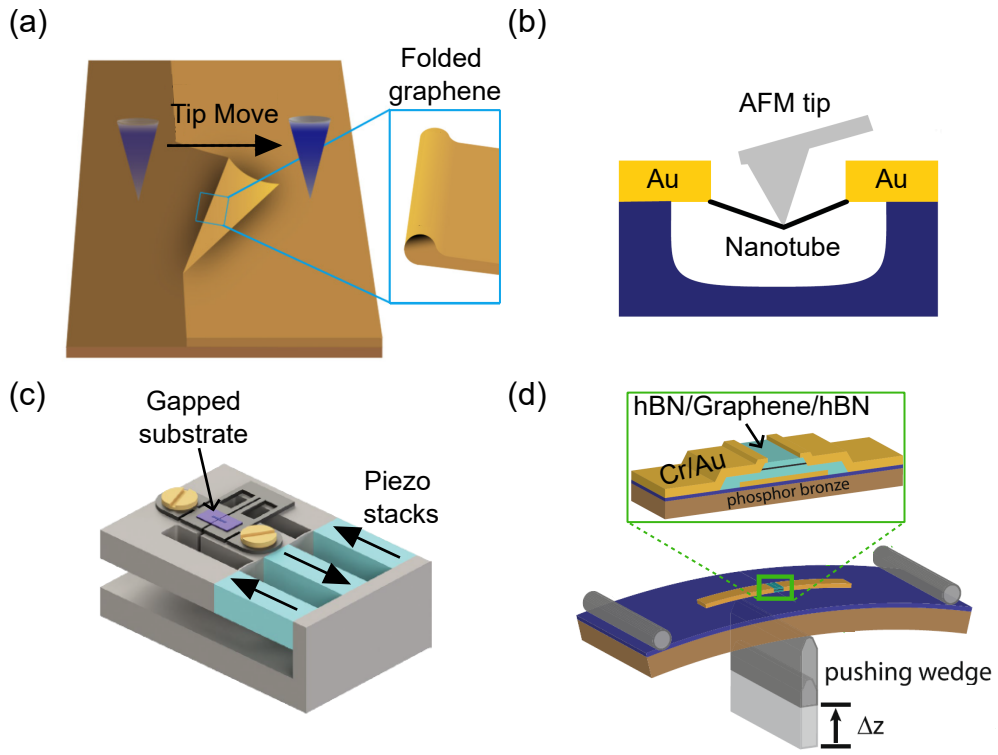

Figure 1.4: Common QTS platforms reported in the literature. (a) Graphene is folded to form a strained region [41]. (b) An AFM tip pushes a carbon nanotube, inducing mechanical strain [42]. (c) A strain cell based on three parallel piezo stacks glued to a titanium backing and flexure applies strain to vdW materials placed on a gapped SiO_2/Si substrate mounted on top of the flexure [30]. (d) A three-point bending setup is used to apply strain to an encapsulated graphene device [43].

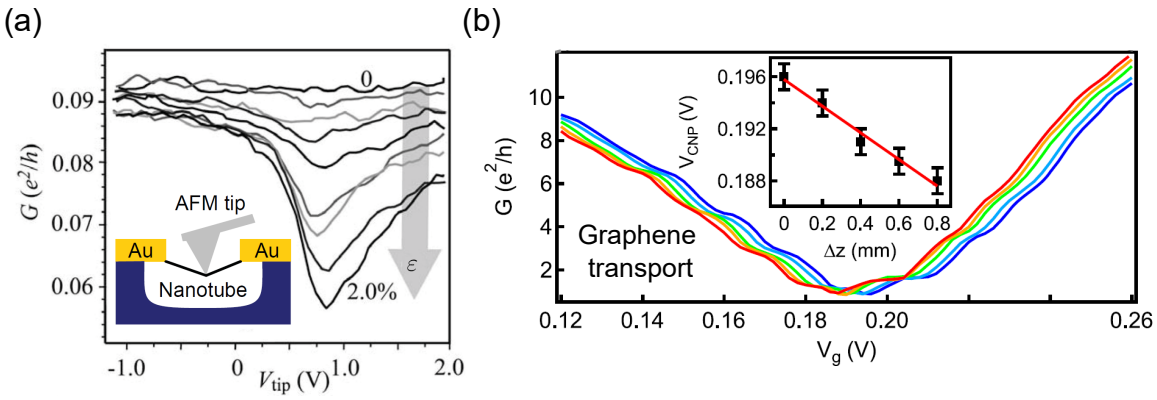

Figure 1.5: Recent experimental results from literature. (a) Charge neutrality point shifts as a function of mechanical strain, demonstrating the existence of strain-induced scalar potential [42]. (b) SWCNT conductance decreases with the AFM tip voltage, indicating strain-tunable band gap [42].

Using the above experimental platforms, some progress has been made in QTS in SWCNTs and graphene. Here, we briefly mentioned two representative experimental results from the literature. First, SWCNT conductance was observed to decrease with increasing mechanical strain [42], indicating a bandgap opening, as shown in Fig. 1.5(a). Secondly, it was demonstrated that the transconductance $G-V_{\mathrm{G}}$ of graphene under uniaxial strain reflects the impact of a scalar potential arising from changes in next-nearest-neighbor hopping [34,43], as shown in Fig. 1.5(b). The effect of strain-induced vector potentials, caused by modifications to nearest-neighbor hopping and distances [34, 46], could not be observed because of the substrate disorder and limited strain range.

Our custom-built platform enables large, precisely controlled, *in-situ* uniaxial strain while allowing low-temperature quantum-transport measurements. We describe our platform and key QTS results in the next section.

1.2 Key results and opportunities for SWCNTs in QTS

Single-wall carbon nanotubes (SWCNTs) can be regarded as rolled-up monolayer graphene sheets. They can be rolled along different directions defined by $C_{\mathrm{h}} = na_1+ma_2$, where a_1 and a_2 are the lattice vectors, as shown in Fig. 1.6(a). The integers n and m define the SWCNT chirality. SWCNTs with $n \neq m = 0$ are called zigzag SWCNTs, those with $n \neq m \neq 0$ are called chiral SWCNTs, and those with $n = m \neq 0$ are called armchair SWCNTs [47, 48]. Figure 1.6(b) shows examples of each type.

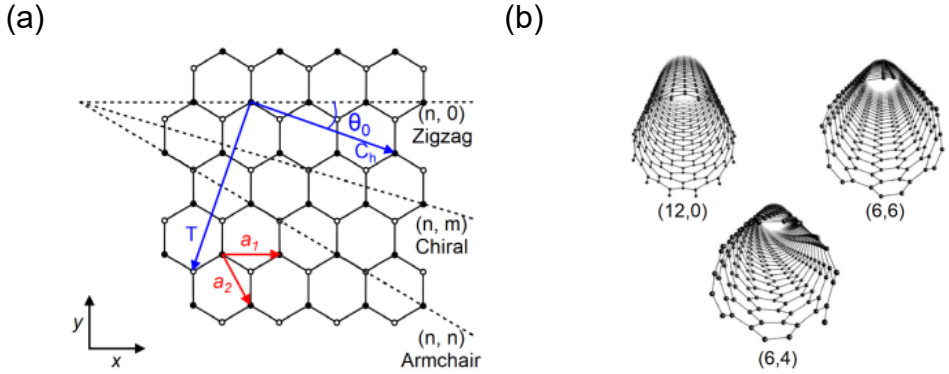

Figure 1.6: Lattice structures of SWCNTs. (a) The chiral vector C_{h} defines the wrapping direction (chirality) of SWCNTs. (b) Cartoons of zigzag (12,0), armchair (6,6) and chiral (6,4) SWCNTs. Figure adapted from Ref. [47].

Among all these nanotubes, armchair SWCNTs are metallic, with a zero bandgap that

remains unchanged under uniaxial strain. Figure 1.7(a) shows their band structure, which features a linear dispersion of the energy E as a function of momentum k intersecting at a single Dirac point. Nanotubes with $n-m$ not equal to a multiple of three are semi-conducting and have a finite bandgap E_g. Their bands have a parabolic shape near the band edge and a linear relationship at higher energy levels (Fig. 1.7(a)). Nanotubes with $n-m$ equal to a multiple of three (excluding armchair nanotubes) are called quasi-metallic. To first-order, they have zero bandgap like arm-chair ones, but in practice, they are inevitably subject to corrections such as trigonal warping and mechanical deformation, leading to small bandgaps. Hence, they are called quasi-metallic SWCNTs and possess a widely strain-tunable bandgap.

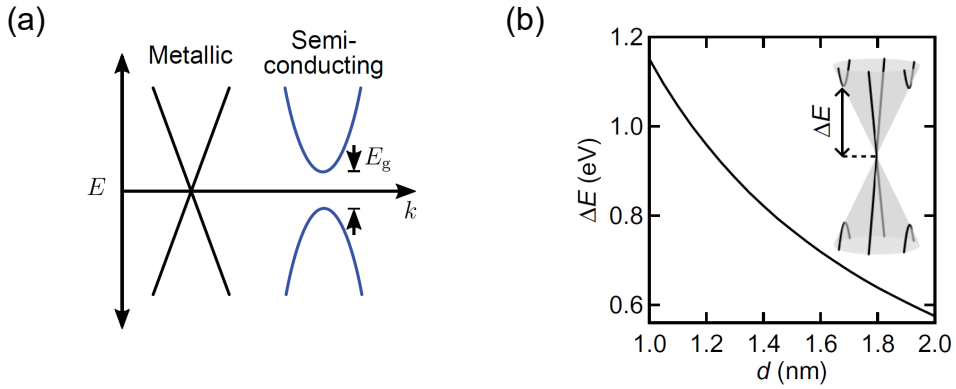

Figure 1.7: Band structures of SWCNTs. (a) Band structures of quasi-metallic and semiconducting SWCNTs with zero and finite bandgaps, respectively. Figure adapter from Ref. [49]. (b) The sub-band energy spacing ΔE in unstrained quasi-metallic SWCNTs as a function of their diameter d.

We focus specifically on quasi-metallic nanotubes because their band structures respond to uniaxial strain and have low-energy states, offering more interesting quantum transport behavior under strain. Figure 1.7(b) shows the minimum energy, ΔE, required for electrons to reach the second subband in a quasi-metallic SWCNT as a function of nanotube diameter. For SWCNTs with diameters typically below 2 nm, this minimum energy is approximately 600 meV, which is much larger than realistic Fermi level achieved in low-temperature transport. Thus, in SWCNTs, only one conduction mode contributes to transport, unlike in graphene where many modes participate in transport. This simplifies both calculations and data analysis, facilitating quantitative interpretation of QTS experiments.

Another difference between SWCNTs and graphene is the absence of edge disorder in SWCNTs, owing to their perfect periodic boundary condition. This disorder is why graphene devices are typically fabricated with large width-to-length ratios to minimize edge effects and

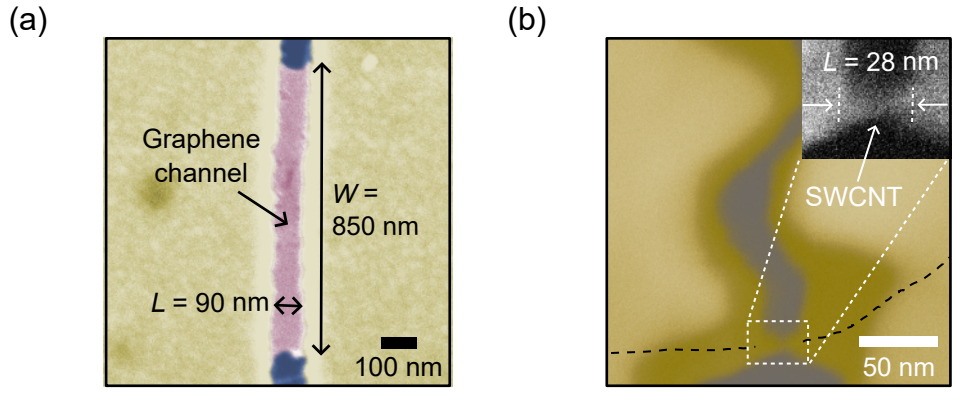

Figure 1.8: Graphene and SWCNT devices for QTS. (a) Top-view of a suspended graphene device with a channel length ≈ 90 nm. (b) Top-view of a suspended SWCNT device with a channel length ≈ 28 nm.

simplify modeling [36, 50]. Figure 1.8(a) shows one of our graphene devices whose channel width is approximately 850 nm and channel length ≈ 90 nm. For SWCNT devices, the channel length can be even shorter (30 nm), as shown in Fig. 1.8(b). The shorter channel length permits for a larger tunable strain range, enabling the observation of more significant strain-induced effects in SWCNTs.

To accelerate progress in QTS of SWCNTs, we developed both an applied theory incorporating realistic experimental parameters and an experimental platform. Figure 1.1(a) shows a schematic of our experimental platform, where a push screw bends a Si substrate to apply mechanical strain to a SWCNT channel. Suspended SWCNT devices eliminate substrate-induced disorder, and the Au clamps act as cantilevers amplifying the applied strain. A standard DC circuit is used for transport measurements. Based on this platform, we develop an applied theory of quantum ballistic transport in strained SWCNTs using realistic parameters. We demonstrate that mechanical strain can tune the propagation angle Θ (the helix angle with respect to the nanotube axis) of charge carriers in the SWCNT channel, as shown in Fig. 1.9(a). In the calculated G–$\Delta\mu_{\mathrm{G}}$–$\varepsilon_{\mathrm{total}}$ data for a quasi-metallic SWCNT (Fig. 1.9(b)), we clearly observed bandgap opening, highlighted by the white region, along with periodic quantum interferences of spacing ΔE_{FP} that can be described with a mechanical Aharonov–Bohm effect.

We then fabricated suspended SWCNT-QD transistors and measured their transport at low temperature under strain. Figure 1.10(a) shows a SWCNT quantum dot with a channel length of $L = 31$ nm, and the inset presents the QD schematic. We find that mechanical strain can tune the work function of the SWCNT channel. Figure 1.10(b) shows that the

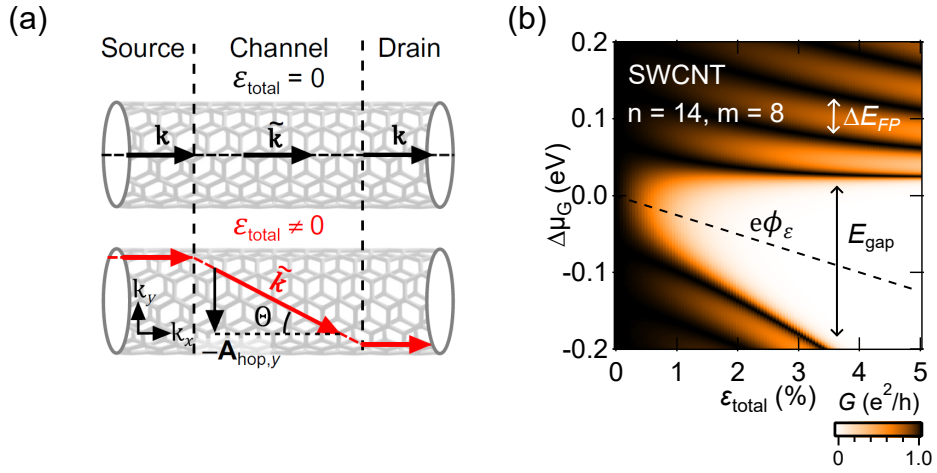

Figure 1.9: Key results of the applied theory for quantum transport in uniaxially strained SWCNTs. (a) Trajectory of the charge carriers in quasi-metallic nanotubes under zero (black line) and finite (red line) strain. The charge carrier propagation angle Θ is strain tunable. (b) $G - \Delta\mu_G - \varepsilon_{\text{total}}$ data simulated for a (14,8) quasi-metallic tube. Strain opens a band gap, as shown by the white region. A linear shift is created by the scalar potential energy $e\phi_\varepsilon$ (black dashed line). Clear FP resonances, with spacing ΔE_{FP}, are visible. Figures adapted from Ref. [38]

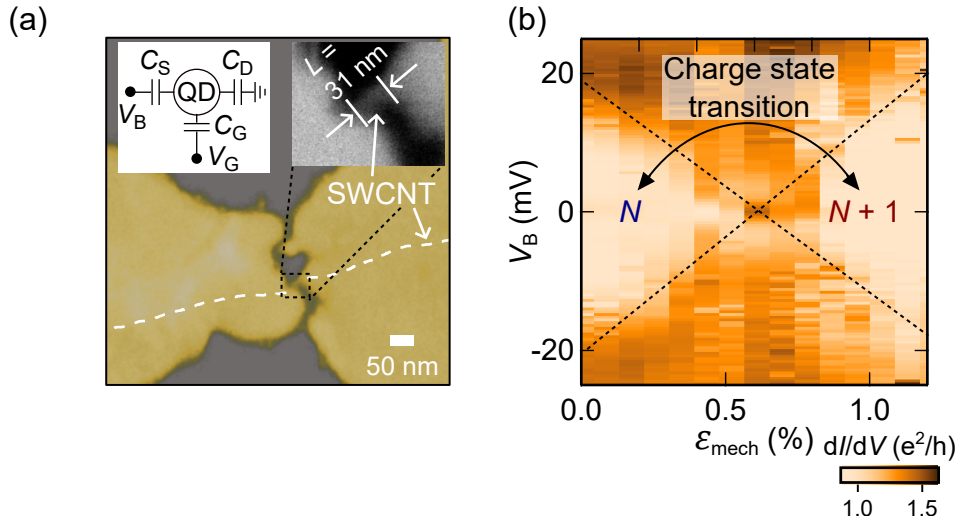

Figure 1.10: Key results of SWCNT quantum dots under tunable uniaxial strain. (a) Top-view SEM image of a SWCNT device. White dashed lines mark the positions of the SWCNT beneath the Au electrodes. The channel length is determined from the SEM image (top-right inset) as 31 nm, and the top-left inset shows the QD circuit. (b) The average charge state in the SWCNT-QD shown in (a) transitions from N to $N + 1$ with increasing strain.

charge state of the SWCNT-QD switched from N to $N+1$ with increasing strain. This strain-induced doping tunability depends on the nanotube chirality, which can in turn be used for chirality identification. We also saw scalar and vector potentials in quantitative graphene QTS experiments. Additionally, we observed that mechanical strain can tune electromechanical resonances in both suspended SWCNT and suspended graphene QDs.

1.3 Organization of this thesis

This chapter provided a brief overview to the field of quantum transport straintronics (QTS) and to our research project on QTS in SWCNTs. In Chapter 2, we discuss our applied theoretical model for quantum transport in uniaxially strained SWCNTs, incorporating realistic experimental parameters. In Chapter 3, we present the experimental methods used to fabricate nanotube devices and integrate them in the QTS platform. In Chapter 4, we show our experimental transport measurements on SWCNT QDs over a broad and reversible range of mechanical strain, demonstrating mechanical gating in QDs. In Chapter 5, we discuss the mechanical control of quantum transport in graphene and strain-tunable self-oscillations in graphene and SWCNTs. Finally, in Chapter 6, we conclude the thesis and discuss future research directions in this field.

Chapter 2

QTS and Mechanical Aharonov-Bohm Effect in Quasi-metallic SWCNTs

SWCNTs are effectively narrow ribbons of 2D materials with atomically precise edges. They are ideal systems to harness quantum transport straintronics (QTS), i.e. using mechanical strain to control quantum transport. Their large subband energy spacing ($\sim$ 0.8 eV) leads to transistors with a single quantum transport channel. We adapt an applied model to study QTS in uniaxially-strained quasi-metallic-SWCNT transistors. The realistic device parameters are based on an existing experimental platform, with channel lengths of $L =$ 50 nm, diameters $d \approx 1.5$ nm, and strains up to $\varepsilon_{\text{total}} \approx 7$ %. We demonstrate that the charge carrier's propagation angle (the helix angle with respect to the tube's axis) Θ is fully tunable with $\varepsilon_{\text{total}}$. When Θ reaches 90^o, the conductance G is completely suppressed. A strain-generated band gap can be tuned up to ≈ 400 meV. Mechanical strain adds both scalar ϕ_ε and vector $\mathbf{A}$ gauge potentials to the transistor's Hamiltonian. These potentials create a rich spectrum of quantum interferences in G, which can be described as a mechanical Aharonov-Bohm effect. The charge carriers' quantum phase can be controlled by purely mechanical means. For instance, a full 2π phase shift can be induced in a (12,9) tube by a 0.7 % strain change. This work opens opportunities to add quantitative quantum transport strain effects to the tools box of quantum technologies based on 2D materials and their nanotubes.

The work presented in this chapter is adapted from L. Huang *et al.*, Quantum transport straintronics and mechanical Aharonov-Bohm effect in quasimetallic single-wall carbon nanotubes, Physical Review Applied **23** (1), 014030 (2025), for which I am the lead author.

2.1 Introduction

Quantum transport straintronics (QTS) aims to engineer quantum-coherent charge transport using mechanical deformations (strains) in materials [20,33,35,36,51–53]. An ideal quantum straintronics transistor should permit a complete electro-mechanical control of the electrons' Hamiltonian. For example, its charge current's quantum phase should be fully tuneable both mechanically and electrostatically. This would offers a wide range of possibilities to optimize quantum effects in 2D materials (2DMs) such as graphene, transition metal dichalcogenides (TMDs), twisted 2DMs, and 1D nanotubes/nanoribbons [42,54–57] made from these 2DMs. Technological applications include qubits and quantum circuits [5–10], spintronics [11–16], valleytronics [17–20], superconductivity [21–23], topological transitions [21,24–29], and magnetic transitions [30–32].

The experimental validation of many exciting QTS theoretical predictions [21, 35] has been a major challenge. To verify quantitatively QTS proposals, experiments require a precise control of *all* sources of strain over an entire coherent-transport transistor device. This has only recently been achieved in graphene devices [52]. Graphene is a nearly ideal system to first bridge the existing experiment-theory divide in QTS. Its extreme mechanical strength, flexibility, and elastic deformation range make graphene's electronics vastly tunable via mechanical deformations, while its defect-free lattice supports ballistic (quantum) transport [58, 59]. Moreover, in graphene the effects of mechanical strain on charge carriers can naturally be described as a scalar potential ϕ_ε, arising from changes in the next-nearest-neighbour hopping, and vector gauge potentials $\boldsymbol{A}$, from modifications to the nearest-neighbour hopping and distances [1, 20, 33, 36, 46].

However, two experimental limitation remains to fully explore *quantitative* QTS. First, graphene and 2DM crystals do not usually have atomically ordered edges and this scrambles the quantum phase of their charge carriers. One solution is to use device geometries with large width/length aspect ratios to minimize edge effects [43, 52]. Still, a large width of the transistor's channel implies that many subbands (transverse momentum modes) contribute to charge transport. Because the quantum phase of each mode is impacted differently by strain [52], it makes a precise control of QTS complex. Single-wall carbon nanotubes (SWCNTs) and other nanotubes [54, 60] naturally resolve these issues.

SWCNTs have perfect transverse (periodic) boundary conditions, and their very narrow width (circumference) naturally leads to a single transport mode (subband) being available at experimentally relevant charge dopings. Until now, only the most basic QTS properties of SWCNTs, such as bandgaps, have been studied [42, 61]. Thus, they represent a major

unexplored opportunity for QTS experiments and models. For instance, we foresee that transistors made with a SWCNT will permit a full *mechanical* control of the quantum phase of their coherent charge current, and a broad strain tuning of their electron-phonon coupling [62] and spin-orbit coupling [16].

In the following sections, we first present a comprehensive applied theoretical model that describes the ballistic conductance in uniaxially strained SWCNTs. What we call an applied model is a theory which integrates all constraints and parameters from an existing experimental platform, and thus can simulate realistic transport features. This model is based on a previous model for graphene [36, 46, 51], and an experimental QTS platform for low-dimensional materials [52]. The range of uniaxial strain we studied, $\varepsilon_{\text{total}} \leq 7.3\%$, is experimentally feasible based on transistor dimensions of $L = 50$ nm and tube diameters of $d \approx 1.5$ nm. We used realistic charge doping levels for the metal-covered SWCNTs contacts [63–66], $\mu_{contact} = 0.12$ eV - 0.25 eV, and for the gate-induced Fermi level in the suspended SWCNT channel $\Delta\mu_G \lesssim 0.5$ eV. This model incorporates all of the dominant effects of uniaxial strain. The four main effects include vector potentials $\boldsymbol{A}$ resulting from alterations to the nearest-neighbor (NN) hoppings [67], strain modification of the SWCNT bandgap E_{gap} [68], a scalar potential ϕ_ε arising from the modulation of next-nearest-neighbor (NNN) hopping [46], as well as modifications to the Fermi velocity v_{F} [69] due to strain.

We then discuss the calculated transport conductance G in quasi-metallic SWCNT transistors under strain. First, we show that G is tuned mechanically because $\varepsilon_{\text{total}}$ precisely controls the propagation angle (helix angle with respect to the tube's axis), Θ, and transmission, T, of the charge carriers across the transistor channel. We demonstrate the ability to adjust mechanically Θ up to 90 degrees which leads to a complete suppression of G. A bandgap is strain-generated and widely tunable. Moreover, the strain-engineering of the quantum phase of charge carriers in the SWCNT channel leads to sharp G interferences. We explain how $\varepsilon_{\text{total}}$ controls both the amplitude ΔG and phase $\Delta\Phi_{\text{FP}}$ of these interferences. We interpret this effect as a mechanical analog of the electrostatic Aharonov-Bohm effect [70, 71]. The use of this mechanical degree of freedom to tune quantum transport, in addition to the usual electro-static ones, will expand the range of capabilities in quantum circuits and technologies.

2.2 QTS in SWCNT transistors

2.2.1 Main results

In this section, we first present the conceptual QTS instrumentation and transistor geometry we used in this model. Then, we highlight the key physical concepts and quantities needed to understand the effects of strain on quantum transport in SWCNTs. We also explain how these are modified compared to the case of graphene [36]. Finally, we summarize the derivation of the ballistic conductance G as a function of experimental parameters, such as $\varepsilon_{\text{total}}$ and V_{G}. A more detailed derivation is presented in Sec. 2.2.2, and a related model for strained-graphene transistors was reported previously [36, 52].

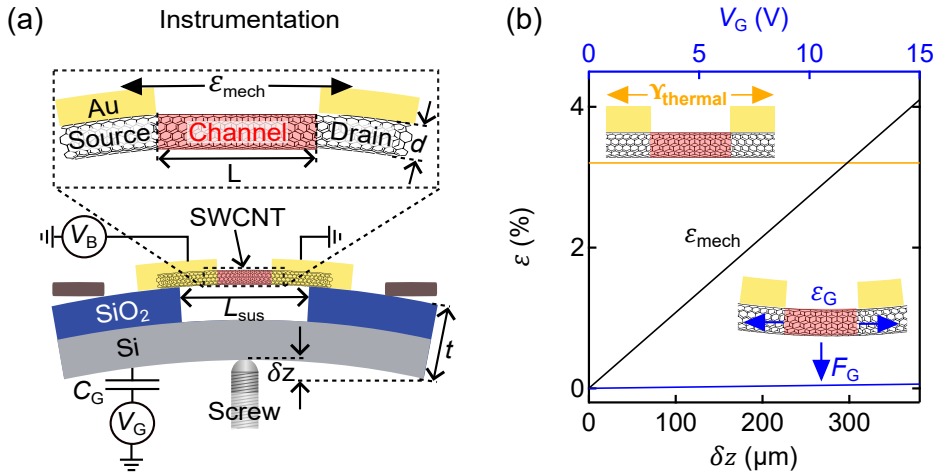

Figure 2.1: Experimental platform for quantum transport straintronics in SWCNTs. (a) Side-view diagram of the QTS platform We describe in our model. A push screw bends the Si substrate, which applies a $\varepsilon_{\text{mech}}$ to the suspended SWCNT channel. A standard dc circuit is used for transport measurements. (b) Mechanical strain (black trace), $\varepsilon_{\text{mech}}$, and thermal strain (gold trace), $\varepsilon_{\text{thermal}}$, versus δz. The gate-induced strain ε_{G} is shown in blue as a function of V_{G} (top-axis).

Figure 2.1(a) shows the experimental situation described by our model, where a SWCNT is freely suspended above a Si substrate (the suspension height is 150 nm) and its two ends are mechanically held by gold films (clamps). Two important points must be noted about these gold clamps. First, they are themselves suspended over an extended distance, thus forming cantilever beams. Secondly, the gold film dopes electrostatically the SWCNT sections which it covers [63, 66] (top inset of Fig. 2.1(a)). These gold-covered sections of SWCNT form the source and drain contacts [72] connecting the naked SWCNT channel in Fig. 2.1(a). The electrostatic gate voltage V_{G} controlling the channel's Fermi energy, and the very small bias voltage $V_{\text{B}} \sim 0.1$ meV used experimentally to measure G are applied as shown in Fig. 2.1(a).

The three main sources of strain acting on the suspended SWCNT channel are shown in Fig. 2.1(b). In the lower inset, the electrostatic force $F_{\rm G}$ [36, 52] leads to a strain $\varepsilon_{\rm G}$ (blue trace) which depends on $V_{\rm G}$ (top axis). Over the experimentally relevant range of $|V_{\rm G}| \leq \pm$ 15 V, we calculate a negligibly small $\varepsilon_{\rm G} \lesssim 0.05\%$ due to the very short channel length (Sec. 2.2.2). As shown in the top inset of Fig. 2.1(b), the thermal contraction (expansion) of the gold clamps (SWCNT channel) when cooling down the device to cryogenic temperatures leads to a significant, but constant, $\varepsilon_{\rm thermal}$. For our device dimensions, we calculate $\varepsilon_{\rm thermal} \approx$ 3.2 % as shown by the gold trace (Sec. 2.2.2). Thus, the only tunable strain in the device's channel is due to the substrate's bending as shown in Fig. 2.1(a). We label this strain component as $\varepsilon_{\rm mech}$.

This mechanically tunable $\varepsilon_{\rm mech}$ is along the tube's axis and applied by slightly bending the silicon substrate (ultra-thin Si) using a precision push screw. The applied strain is given by [73] $\varepsilon_{\rm mech} = (3L_{\rm sus}t/D^2)\delta z/L$, where δz is the vertical displacement of the screw, $L_{\rm sus}$ is the total suspension length of the gold beams and transistor's channel, L is the channel length, t is the substrate thickness and D is the distance betIen two mechanical anchoring points. We used realistic experimental values [52] of $L = 50$ nm, $L_{\rm sus} = 600$ nm, $D = 8.2$ mm, $t = 200$ μm and δz up to 380 μm (limited by the failure of the Si substrate). This gives a tunable strain range of $\varepsilon_{\rm mech} = 0$ - 4.1% as a function of δz, as shown by the black trace in Fig. 2.1(b).

Adding all sources of strain, the total strain $\varepsilon_{\rm total}$ applied in our devices is tunable (approximately) from 3.2% to 7.3%, in experiments at low temperature. It is remarkable, and useful technologically, that $\varepsilon_{\rm mech}$ is completely independent from the charge doping in the channel which is controlled via $V_{\rm G}$.

When describing straintronics in SWCNTs there are some important conceptual and quantitative differences with the case of graphene. A first distinction is the transverse boundary condition (BC). The BC is periodic for SWCNTs, and it depends of how the underlying graphene layer is rolled-up to form the tube. The periodic BC for the transverse momentum k_y can be written as $k_y = (2\pi/|\boldsymbol{C}_{\rm h}|)(N + \alpha)$, where N is an integer, and $\boldsymbol{C}_{\rm h} = n\boldsymbol{a}_1 + m\boldsymbol{a}_2$. The vectors $\boldsymbol{a}_1$ and $\boldsymbol{a}_2$ are the hexagonal lattice vectors, while n and m are integers denoting the chirality of the tube. The length of the chirality vector $|\boldsymbol{C}_{\rm h}|$ is the width W of the unrolled graphene ribbon. The factor α is zero for the quasi-metallic tubes (i.e. $(n - m)/3$ = integer [74]), and around 1/3 in non-metallic tubes [75]. As shown in Fig. 2.2(a), the consequence of this BC is the creation of a subband energy spacing $\Delta E = \hbar v_F(2\pi/W) \approx$ 0.8 eV when $d \approx 1.5$ nm.

To understand transport across the transistor correctly, ΔE must be compared with μ_{contact}. The Fermi level in the contacts is set by the charge transferred from the gold films (clamps) to the tube sections they cover. Its value ranges from ~ 0.05 to 0.25 eV [66] and can be controlled by Joule annealing the device [52, 63]. The inset of Fig. 2.2(a) shows the bandstructure of an unstrained quasi-metallic tube (n=14 m=8), whose $d \approx 1.5$ nm. The solid black lines indicate the allowed k_y's set by the periodic BC. We see that in quasi-metallic tubes, the dispersion for the first subband is linear and does not have a bandgap without strain, $E_{\text{gap}} = 0$. The dispersion of the second subband has a band gap $E_{\text{gap},2}$, and $\Delta E = (E_{\text{gap},2} - E_{\text{gap}})/2$. The main panel of Fig. 2.2(a) shows ΔE vs. d for quasi-metallic SWCNTs.

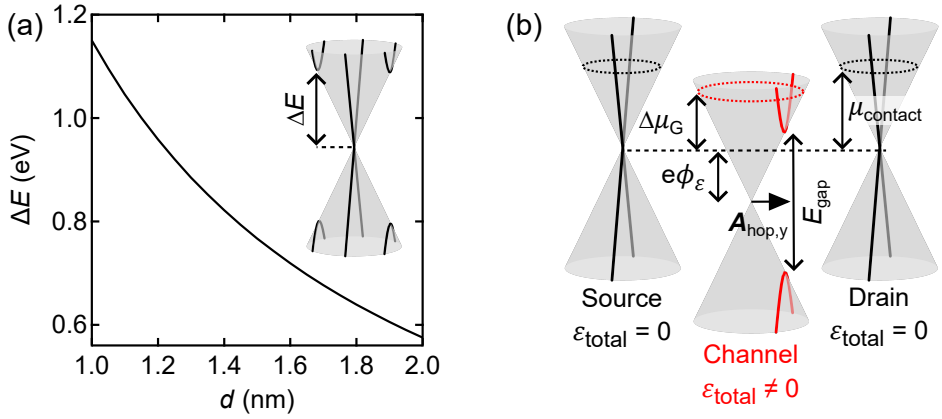

Figure 2.2: Band structure in strained quasi-metallic SWCNT transistors. (a) The subband energy spacing ΔE in unstrained quasi-metallic SWCNT versus their diameter d. The inset shows the bandstructure in one valley of an unstrained (n=14 m=8) tube. (b) Band structure in the source, channel, and drain sections of a strained quasi-metallic nanotube with $d \approx$ 1.5 nm. For clarity, the three band structures are shown as if they Ire disconnect (not equilibrated). We label the strain-induced scalar potential energy $e\phi_\varepsilon$ and vector potential component $A_{\text{hop},y}$, the gate-induced scalar potential energy $\Delta\mu_{\text{G}}$, the strain-induced band gap E_{gap}, and the Fermi energy in the SWCNT contacts μ_{contact}.

Figure 2.2(b) shows the band structure across the different sections of a quasi-metallic SWCNT transistor under strain. The source (left) and drain (right) section are unstrained and their dispersion is as shown in the inset of Fig. 2.2(a). The dashed circles indicate the position of an experimentally realistic μ_{contact} (Fermi level). We see that μ_{contact} is always much less than ΔE. This is true over a broad range of SWCNT diameters (Fig. 2.2(a)). Therefore, our SWCNT transistors always have a single quantum transport channel. This is important for quantum technological applications, since a single subband wavevector k means that *a single quantum phase describes the entire current.* We will see below how this

phase can be manipulated mechanically.

The central section of Fig. 2.2(b) shows the band structure in one valley, K_i, of a quasi-metallic channel under a strain $\varepsilon_{\text{total}}$. It highlights the key quantities needed to derive the ballistic conductance across the device. Using these quantities, the Hamiltonian of the charge carriers in the K_i valley of the strained-SWCNT channel and the unstrained-SWCNT contacts are given by Eqs. 2.11 and 2.12, respectively [34, 36, 50, 69]:

$$H_{K_i,\text{channel}} = \hbar v_F \boldsymbol{\sigma} \cdot (\bar{I} + (1-\beta)\bar{\boldsymbol{\varepsilon}}) \cdot \tilde{\boldsymbol{k}} + e\phi_\varepsilon + \Delta\mu_{\text{G}} \tag{2.1}$$

$$H_{K_i,\text{contact}} = \hbar v_F \boldsymbol{\sigma} \cdot \boldsymbol{k} + \mu_{\text{contact}} \tag{2.2}$$

where $\tilde{\boldsymbol{k}} = \boldsymbol{k} - \boldsymbol{A_i}$ and $\boldsymbol{k}$ are the electron's wavevectors in the channel and contacts, respectively. The Fermi velocity is $v_F = 8.8 \times 10^5$ m/s, $\bar{I}$ is the identity matrix, and $\bar{\boldsymbol{\varepsilon}}$ is the strain tensor. The parameter $\beta \approx 2.5$ [34] is the electronic Grüneisen parameter. The factor $\bar{I} + (1-\beta)\bar{\boldsymbol{\varepsilon}}$ describes the strain-dependent correction to the Fermi velocity, the terms $e\phi_\varepsilon$ is the strain-induced scalar potential, $\Delta\mu_{\text{G}}$ is the gate-induced electrostatic potential, and μ_{contact} is the Fermi level in the source and drain graphene contact regions set by the charge transfer from the physisorbed gold [66]. In the device's $x-y$ coordinates, x is along the tube's axis and y is along its circumference. The strain tensor $\bar{\boldsymbol{\varepsilon}}$ has elements $\varepsilon_{xx} = \varepsilon_{\text{total}}, \varepsilon_{yy} = -\nu\varepsilon_{\text{total}}$, and $\varepsilon_{xy} = \varepsilon_{yx} = 0$, where $\nu = 0.165$ is the Poisson ratio [34].

The pseudospin operator $\boldsymbol{\sigma}$ is represented by the 2D Pauli matrix vector. The strain-induced vector potentials $\boldsymbol{A_i}$ shift the position of the Dirac (charge neutrality) points in momentum space, and will be discussed in detail below. The strain-induced scalar potential ϕ_ε rigidly shifts down in energy the overall band structure in the channel. Its value is [52, 67] $\phi_\varepsilon = g_\varepsilon(1-\nu)\varepsilon_{\text{total}}/e$, where $g_\varepsilon \approx 2.6$ eV. The quantity $\Delta\mu_G$ is the electrostatic energy induced by V_{G} which sets the charge doping and Fermi level in the channel.

The two key strain-induced energy terms in the Hamiltonian have comparable energy scales and are shown in Fig. 2.2(b), $e\phi_\varepsilon$ and $\hbar v_{\text{F}} v_{\text{yy}} A_y = E_{\text{gap}}/2$. Where the parameter v_{yy} = 1 - (1 - β)$\nu\varepsilon_{\text{total}}$ is simply the y-direction strain modification to the Fermi velocity. The energy shift $e\phi_\varepsilon = g_\varepsilon(1-\nu)\varepsilon_{\text{total}}$ reaches up to ≈ 0.16 eV for the maximum $\varepsilon_{\text{total}}$ of 7.3%. As a reminder, this maximum $\varepsilon_{\text{total}}$ was calculated above based on realistic experimental parameters (Sec. 2.2.2).

The magnitude of the strain-induced energies are to be compared with $\Delta\mu_G$ in the channel, see Fig. 2.2(b). This latter quantity is quantitatively different in SWCNTs compared to graphene, because the density of states $g(E)$ differs in 1D and 2D. For the first subband

of a SWCNT, $g(E) = (4/\pi\hbar v_{\mathrm{F}})(1 - (E_{\mathrm{gap}}/(2\mu_{\mathrm{channel}}))^2)^{-1/2}$. Additionally, due to the presence of the bandgap, the so-called quantum capacitance C_{DOS} [76] can be quite small in SWCNTs, and thus modify significantly the total capacitance of the channel C_{total}. This later is the combination in series of C_{DOS} and the geometric gate capacitance per unit length $C_{\mathrm{G}} = 2\pi\epsilon_o/(cosh^{-1}(t_{\mathrm{vac}}/r))$, where $t_{\mathrm{vac}} = 150$ nm and $r \approx 0.75$ nm. This means that $dV_{\mathrm{G}} = (C_{\mathrm{DOS}} + C_{\mathrm{G}})/(C_{\mathrm{G}}) \times (d\mu_{\mathrm{channel}}/e))$, see Sec. 2.2.2 for details. For an experimental V_{G} range of $\pm$ 15 V, the typically the values of $\Delta\mu_{\mathrm{G}}$ in SWCNTs are up to 0.5 eV depending on the chirality and strain, compared to $\sim$ 0.1 eV in graphene. This enhanced ability to tune $\Delta\mu_{\mathrm{G}}$ gives a broader spectroscopic range (tunability) to SWCNT strain-transistors.

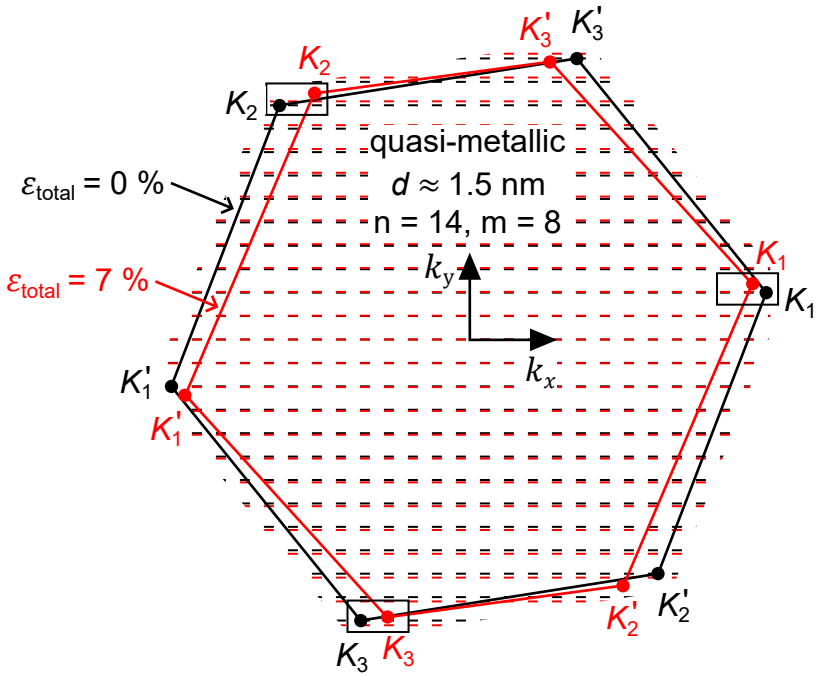

Figure 2.3: The first Brillouin zones (solid lines) and sub-bands (dashed lines) for a (14,8) SWCNT are shown in black and red for $\varepsilon_{\mathrm{total}} = 0$ and 7 %, respectively.

Figure 2.3-2.5 describes the strain-generated vector potentials $\boldsymbol{A_i}$ in Eq. 2.11, and how they open and tune bandgaps in quasi-metallic SWCNTs. Figure 2.3 shows in black ($\varepsilon_{\mathrm{total}} = 0$) and red ($\varepsilon_{\mathrm{total}} = 7$ %) the first Brillouin zone (FBZ) for a quasi metallic (14,8) tube. The horizontal dashed-black and dashed-red lines indicate the positions of the allowed k_y quantized values. We immediately notice that the Dirac points (charge neutrality points at K, K' indicated by circle markers) move in k-space with strain. Moreover, the three-fold degeneracy of the K and K' valleys is lifted by strain, and We label each valley as K_i and K'_i, with $i = 1, 2, 3$. In Fig. 2.4, We show zoomed-in views of the K_1, K_2, and K_3 valleys

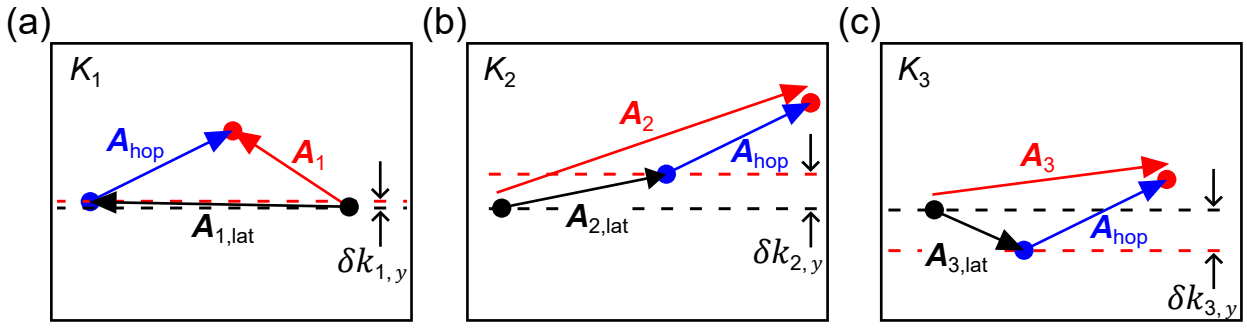

Figure 2.4: Strain-induced shifts of Dirac points and sub-bands in a quasi-metallic SWCNT. (a), (b), (c) Zoomed-in views of the K_1, K_2, and K_3 valleys shown in Fig. 2.3. Vector potentials ($\mathbf{A}_{\rm lat}$) arising from the stretching of nearest-neighbour distances are canceled out by sub-band shifts ($\delta k_{\rm y}$).

to better visualize the $\boldsymbol{A_i}$. The $\boldsymbol{A_i}$ are defined as the displacement between the original (black) and new (red) locations of the Dirac points of the underlying graphene lattice. By symmetry, $\boldsymbol{A_i'}$ in the K_i' valleys are equal to $-\boldsymbol{A_i}$.

The strain modification of the NN carbon atom distances and of the electron hopping amplitudes on the hexagonal carbon lattice can be described by, $\boldsymbol{A}_{i,\rm lat}$ and $\boldsymbol{A}_{\rm hop}$, respectively [46]. These two components and their sum, $\boldsymbol{A_i}$, are shown in Figs. 2.4. Equation 2.24 gives the expression to calculate these vector potentials in SWCNTs.

$$\boldsymbol{A}_{\rm hop} = \frac{\beta\varepsilon(1+\nu)}{2a}\begin{pmatrix}\sin 3\theta_h \\ \\ \cos 3\theta_h\end{pmatrix} \tag{2.3a}$$

$$\boldsymbol{A}_{1,\rm lat} = \frac{2\pi\varepsilon}{3a}\begin{pmatrix}-\cos\theta_h - \frac{1}{\sqrt{3}}\sin\theta_h \\ \\ \frac{1}{\sqrt{3}}\nu\cos\theta_h - \nu\sin\theta_h\end{pmatrix} \tag{2.3b}$$

$$\boldsymbol{A}_{2,\rm lat} = \frac{2\pi\varepsilon}{3a}\begin{pmatrix}\cos\theta_h - \frac{1}{\sqrt{3}}\sin\theta_h \\ \\ \frac{1}{\sqrt{3}}\nu\cos\theta_h + \nu\sin\theta_h\end{pmatrix} \tag{2.3c}$$

$$\boldsymbol{A}_{3,\rm lat} = \frac{4\pi\varepsilon}{3\sqrt{3}a}\begin{pmatrix}\sin\theta_h \\ \\ -\nu\cos\theta_h\end{pmatrix} \tag{2.3d}$$

Here, a =1.42 Å is the NN carbon-carbon distance without strain. θ_h is the angle between the chiral vector $\boldsymbol{C}_h$ and the zigzag lattice direction [47]. We note that the definition of θ_h differs from the definition of the lattice orientation used in graphene devices [52].

Stretching tubes longitudinally also decreases their circumference due to the Poisson ratio, i.e. $\varepsilon_{yy} = -\nu\varepsilon_{\text{total}}$. Because the subband energy spacing ΔE depends on the circumference, a special attention must be paid to this change. Under strain, the periodic BC along the circumference becomes:

$$\tilde{k_y}(1+\varepsilon_{yy})C_h = 2\pi N \tag{2.4}$$

where N is an integer. As can be seen in Figs. 2.3-2.4, in the absence of strain the dashed-black subbands pass through the black Dirac points in quasi-metallic nanotubes. This translates to a zero bandgap as shown in Fig. 2.5(a). When strain is applied, the diameter of the tubes shrinks and ΔE increases. The strained (dashed-red) subbands in Figs. 2.3-2.4 no longer pass through the red Dirac points. A close inspection of Fig. 2.4 reveals that the change in ΔE shifts the allowed k_y values. The k_y shifts are exactly equal to $A_{i,lat,y}$, and thus always cancel them out. Meaning that the allowed y-component of the generalized wave vector in the strained channel are $(k_y + A_{i,\text{lat},y}) - (A_{i,\text{lat},y} + A_{\text{hop},y}) = k_y - A_{\text{hop},y}$. Thus, only the $A_{\text{hop},y}$ part of the vector potentials matters in determining the allowed electron states.

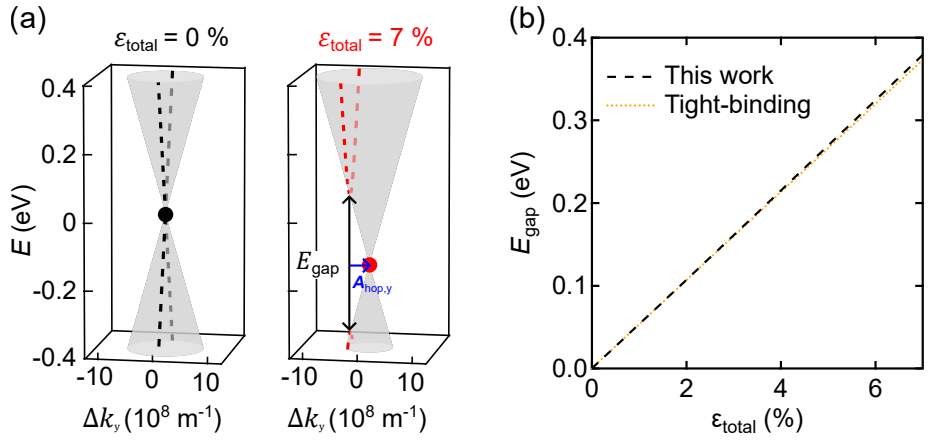

Figure 2.5: Strain-tunable band gap in a quasi-metallic SWCNT. (a) Energy-momentum dispersion around the Dirac points for $\varepsilon_{\text{total}} = 0$ (left) and 7 % (right). Strain creates a band gap E_{gap} due to the vector potential. (b) The calculated E_{gap} vs. $\varepsilon_{\text{total}}$ for a (14,8) SWCNT in our work (dashed black) and in previous work [68] (dotted gold).

Figure 2.5(b) shows that the $A_{\text{hop},y}$ also lead to strain-tunable band gaps. The calculated values for $E_{\text{gap}} = 2\hbar v_{\text{F}} v_{yy} A_{\text{hop},y}$ as a function of $\varepsilon_{\text{total}}$ are shown in Fig. 2.5(b), and are in complete agreement with previous work [68].

The next step towards our objective of calculating G across the transistors is to solve for the transmission amplitude t_ξ of the carriers. We do this by using the longitudinal BCs for the wavefunction at the source-channel and channel-drain interfaces in each valleys $\xi = \pm 1$, where the $+$ and $-$ refer to K_i and K_i', respectively. This step is detailed in Sec. 2.2.2, and in previous works [36, 50, 52]. The transmission probability is $T_\xi = |t_\xi|^2$, and its expression is given in Eq. 2.27.

$$T_\xi = \frac{(k_x \tilde{k_x} v_{xx})^2}{(k_x \tilde{k_x} v_{xx})^2 \cos^2(\tilde{k_x} L) + (k_F \tilde{k_F} - k_y(k_y - \xi A_{\mathrm{hop},y}) v_{yy})^2 \sin^2(\tilde{k_x} L)} \tag{2.5}$$

where $k_F = \mu_{\mathrm{cont}}/(\hbar v_{\mathrm{F}})$ and $\tilde{k_{\mathrm{F}}} = \mu_{\mathrm{channel}}/(\hbar v_{\mathrm{F}})$. The strain modified Fermi velocity factor along x and y are $v_{xx} = 1 + (1-\beta)\varepsilon_{\mathrm{total}}$ and $v_{yy} = 1 - (1-\beta)\nu\varepsilon_{\mathrm{total}}$. Therefore, $k_x = \sqrt{{k_F}^2 - {k_y}^2}$, and $\tilde{k_x} = v_{xx}^{-1}\sqrt{\tilde{k_F}^2 - (v_{yy}\tilde{k_y})^2} = v_{xx}^{-1}\sqrt{\tilde{k_F}^2 - (k_y - \xi A_{\mathrm{hop},y})^2 v_{yy}^2}$.

Finally, the ballistic conductance is

$$G = \frac{4e^2}{h}\frac{1}{2}\sum_\xi T_\xi \tag{2.6}$$

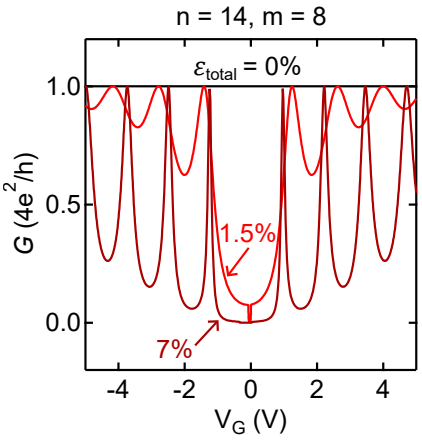

Figure 2.6: Conductance of a quasi-metallic SWCNT under various strain. Calculated conductance G versus $\mathrm{V_G}$ at strains of 0 %, 1.5 %, and 7 % for a (14,8) SWCNT.

We used this expression to calculate the $G - V_{\mathrm{G}}$ data plotted in Fig. 2.6 for a quasi-metallic (14,8) device with strain $\varepsilon_{\mathrm{total}} = 0$ (black), 1.5 % (pale red), and 7 % (dark red). The effect of the strain-induced ϕ_ε is to shift to lower V_G the G minimum as strain increases. A bandgap is clearly visible in the $\varepsilon_{\mathrm{total}} = 7$ % data. Beyond the complete suppression of G inside the bandgap, We observe that $A_{\mathrm{i,y}}$ reduces G at all V_G's and creates interferences. We stress that these Fabry-Pérot interferences take place in a single quantum transport channel. Section 2.3 discusses how they can be precisely strain-engineered *in-situ*.

2.2.2 Supporting material

As shown in Figs. 2.1(a)-(b), the proposed SWCNT transistors are subject to three sources of strain: thermal, electrostatic, and mechanical. The mechanical strain is generated by bending the substrate on which the sample is fabricated. The thermally-induced strain arises during the cooling of the device from room temperature to cryogenic temperatures. The electrostatic strain is caused by the electrostatic force between the gate and the suspended channel. Here, we calculate realistic estimates of the thermal strain and the electrostatic strain based on the device parameters presented in Sec. 2.2.1.

The thermal strain $\varepsilon_{\text{thermal}}$ in the channel has two main sources: the thermal contraction of the Au cantilever beams $\varepsilon_{\text{th,Au}}$ and the thermal expansion of the carbon nanotube channel $\varepsilon_{\text{th,CNT}}$. The impact from the contraction of the Si/SiO_2 substrate is negligible [36]. $\varepsilon_{\text{thermal}}$ is given by:

$$\varepsilon_{\text{thermal}} = \varepsilon_{\text{th,SWCNT}} + \varepsilon_{\text{th,Au}} = \int_{295K}^{1K} \alpha_{\text{SWCNT}}(T)\mathrm{d}T - \frac{u-L}{L}\int_{295K}^{1K} \alpha_{\text{Au}}(T)\mathrm{d}T \tag{2.7}$$

where α_{SWCNT} [77] and α_{Au} [78] are the expansion coefficients of graphene and Au, respectively. The total suspension length $u = 600$ nm is the sum of the suspended cantilever beam lengths plus the channel length, and the channel length $L = 50$ nm. At $T = 1$ K, $\varepsilon_{\text{thermal}} \approx 3.2\%$.

The electrostatic strain ε_{G} is caused by the electrostatic force F_G between the gate and the nanotube channel. An electrostatic force also exists between the gate and the Au cantilevers. However, given the 50 nm thickness of the Au cantilevers, their bending is completely negligible [79].

$\varepsilon_{\text{thermal}} \approx 3.2\%$ ensures that there is no slack in the SWCNT channel independently of the gate voltage applied. Thus, the carbon nanotube remains in the elastic stretching regime. One can then calculate the electrostatic force and the tension as [80]:

$$F_{\text{G}} = \frac{1}{2}C'_{\text{G}}V_{\text{G}}^2 \tag{2.8}$$

$$T_{\text{G}} = \left(\frac{YS}{8}\right)^{\frac{1}{3}} F_{\text{G}}^{\frac{2}{3}} \tag{2.9}$$

where $C'_{\text{G}} = \mathrm{d}C_{\text{G}}/\mathrm{d}t_{\text{vac}}$ is the derivative of the gate capacitance with respect to the vacuum

spacing between the gate and the channel t_{vac}, $Y = 1$ TPa is Young's modulus of a SWCNT, S is the tube cross-sectional area. The capacitance can be modelled as a wire over a plane [63]:

$$C_{\text{G}} = \frac{2\pi\varepsilon_{\text{vac}}}{\cosh^{-1}(2t_{\text{vac}}/d)}L \tag{2.10}$$

where ε_{vac} is the vacuum permittivity, d is the tube diameter and L is the channel length. In our proposed SWCNT devices: $t_{\text{vac}} = 150$ nm, $d = 1.5$ nm, $L = 50$ nm, thus, $C_{\text{G}} \approx 4.64 \times 10^{-19}$ F, and $C'_{\text{G}} \approx 5.16 \times 10^{-13}$ F/m. Using the maximum experimentally realistic gate voltage (in a suspended device) of 15 V, $F_{\text{G}} \approx 5.81 \times 10^{-11}$ N, $T_{\text{G}} \approx 8.73 \times 10^{-10}$ N, $\varepsilon_{\text{G}} = T_{\text{G}}/(YS) \approx 0.06$ %. Comparing to the $\varepsilon_{\text{thermal}} \approx 3.2\%$, ε_{G} is completely negligible at all values of gate voltage.

After determining the contributions from all sources of strain, we now derive step-by-step the applied theoretical model we used to calculate the conductance in strained SWCNT transistors. We begin by incorporating all realistic experimental parameters and strain-induced effects into the Hamiltonian. Then, we solve the Dirac equation (graphene) with uniaxial strain to obtain the plane wave solutions. Next, we use the boundary conditions at the source-channel-drain interfaces to determine the expression for the transmission amplitude. We impose the periodic boundary conditions in the transverse (y) direction appropriate for SWCNTs. It allows us to calculate the strain-induced shifts of the Dirac points and sub-band positions in the SWCNT-channel's First-Brillouin zone. We then identify which subband contributes to charge transport and calculate the value of G.

The Hamiltonian in the strained-SWCNT channel and unstrained-SWCNT contacts are given by Eq. 2.11 and Eq. 2.12:

$$H_{\text{channel}} = \hbar v_F \boldsymbol{\sigma} \cdot (\bar{I} + (1-\beta)\bar{\boldsymbol{\varepsilon}}) \cdot \tilde{\boldsymbol{k}} + \Delta\mu_{\text{G}} + e\phi_{\varepsilon} \tag{2.11}$$

$$H_{\text{contact}} = \hbar v_F \boldsymbol{\sigma} \cdot \boldsymbol{k} + \mu_{\text{contact}} \tag{2.12}$$

where $\tilde{\boldsymbol{k}} = \boldsymbol{k} - \boldsymbol{A_i}$ and $\boldsymbol{k}$ are the electron's wavevectors in the channel and contacts, respectively. The Fermi velocity is $v_F = 8.8 \times 10^5$ m/s, $\bar{I}$ is the identity matrix, $\bar{\boldsymbol{\varepsilon}}$ is the strain tensor. The parameter $\beta \approx 2.5$ [34] is the electronic Grüneisen parameter. In the device's $x-y$ coordinates, x is along the tube's axis and y is along its circumference. The strain tensor $\bar{\boldsymbol{\varepsilon}}$ has elements $\varepsilon_{xx} = \varepsilon_{\text{total}}, \varepsilon_{yy} = -\nu\varepsilon_{\text{total}}$, and $\varepsilon_{xy} = \varepsilon_{yx} = 0$, where $\nu = 0.165$ is the Poisson ratio [34]. The pseudospin operator $\boldsymbol{\sigma} = (\sigma_x, \sigma_y)$ is represented by the Pauli

matrices and acts on the two-component spinor wavefunction associated with the A and B sublattices. The pseudospin orientation aligns either parallel (up) or anti-parallel (down) with the generalized wave vector $\tilde{\boldsymbol{k}}$. The term $\Delta\mu_G$ represents the gate-induced electrostatic potential.

Uniaxial strain induces four main qualitative effects on the channel's band structure. First, it causes a downward shift of the Fermi energy, which can be described by a scalar potential $e\phi_\varepsilon = g_\varepsilon(1-\nu)\varepsilon_{\text{total}}$, where $g_\varepsilon \approx 2.6$ eV [52,67]. Second, it leads to an anisotropic distortion of the Dirac cones, resulting in a direction-dependent Fermi velocity $\bar{\boldsymbol{v}}_{\boldsymbol{F}} = v_F(\bar{\boldsymbol{I}} + (1-\beta)\bar{\boldsymbol{\varepsilon}})$. For uniaxial strain, the matrix $(\bar{\boldsymbol{I}} + (1-\beta)\bar{\boldsymbol{\varepsilon}})$ only has diagonal elements $v_{xx} = 1 + (1-\beta)\varepsilon_{\text{total}}$ and $v_{yy} = 1 - (1-\beta)\nu\varepsilon_{\text{total}}$. Third, the positions of the Dirac points shift in momentum space. These shifts are described by gauge vector potentials $\boldsymbol{A_i}$, where the index i = 1, 2, 3 labels the K and K' valleys (Fig. 2a). Fourth, the subband positions also move in momentum space as the nanotubes' circumferences shrinks under strain (Fig. 2a). There is no strain in the source/drain SWCNT contacts, thus the Hamiltonian (Eq. 2.12) has no strain-induced terms. In the contacts, the term $\Delta\mu_{\text{G}}$ is replaced with μ_{contact}, which is the fixed contact doping due to the charge transfer from the gold film to the tube.

In a strained SWCNT channel, the Dirac equation and the plane wave solution are [52]:

$$\hbar v_F\left(\sigma_x, \sigma_y\right).(\bar{\boldsymbol{I}} + (1-\beta)\bar{\boldsymbol{\varepsilon}}).\begin{pmatrix}\tilde{k_x}\\ \\ \tilde{k_y}\end{pmatrix}\boldsymbol{\Psi} = \tilde{E_n}\boldsymbol{\Psi} \tag{2.13}$$

$$\boldsymbol{\Psi}_{\tilde{k_y},y,\tilde{k_x},x} = a_N\begin{pmatrix}1\\ \operatorname{sgn}(\tilde{k_F})\frac{\tilde{k_x}v_{xx}+i\tilde{k_y}v_{yy}}{\sqrt{(\tilde{k_x}v_{xx})^2+(\tilde{k_y}v_{yy})^2}}\end{pmatrix}e^{i\tilde{k_y}y}e^{i\tilde{k_x}x} \tag{2.14}$$

where $\tilde{k_x}$, $\tilde{k_y}$ are the x and y component of the wavevector $\tilde{k_F} = \tilde{E_n}/(\hbar v_F)$ in the strained channel, $\operatorname{sgn}(\tilde{k_F}) = \pm 1$ refers to the conduction and valence bands respectively, a_N is a normalization coefficient.

Wavevectors in the contacts and channel are denoted as $\boldsymbol{k} = k_x\hat{x} + k_y\hat{y}$ and $\widetilde{\boldsymbol{k}} = \widetilde{k}_x\hat{x} + \widetilde{k}_y\hat{y}$, respectively, where $k_y = 2\pi N/C_h$, C_h is tube circumference and N is an integer. The wavefunction for the N-th mode (subband) in the different regions as shown in Fig. 4.4 can then be obtained:

$$\mathbf{\Psi} = \begin{cases} \mathbf{\Phi}_S, & \text{if } x < 0 \\ \tilde{\mathbf{\Phi}}, & \text{if } 0 < x < L \\ \mathbf{\Phi}_D, & \text{if } x > L \end{cases} \tag{2.15}$$

$$\mathbf{\Phi}_S = \mathbf{\Psi}_{k_y,y,k_x,x} + r_N \mathbf{\Psi}_{k_y,y,-k_x,x} \tag{2.16}$$

$$\tilde{\mathbf{\Phi}} = \alpha_N \mathbf{\Psi}_{\tilde{k_y},y,\tilde{k_x},x} + \beta_N \mathbf{\Psi}_{\tilde{k_y},y,-\tilde{k_x},x} \tag{2.17}$$

$$\mathbf{\Phi}_D = t_N \mathbf{\Psi}_{k_y,y,k_x,x-L} \tag{2.18}$$

Here, r_N and t_N represent the reflection and transmission amplitudes, while α_N and β_N are coefficients. Due to the continuity of Ψ at the boundaries $x = 0$ (source-channel edge) and $x = L$ (channel-drain edge), we obtain the following boundary conditions.

$$\mathbf{\Psi}_{k_y,y,k_x,0} + r_N \mathbf{\Psi}_{k_y,y,-k_x,0} = \alpha_N \mathbf{\Psi}_{\tilde{k_y},y,\tilde{k_x},0} + \beta_N \mathbf{\Psi}_{\tilde{k_y},y,-\tilde{k_x},0} \tag{2.19}$$

$$\alpha_N \mathbf{\Psi}_{\tilde{k_y},y,\tilde{k_x},L} + \beta_N \mathbf{\Psi}_{\tilde{k_y},y,-\tilde{k_x},L} = t_N \mathbf{\Psi}_{k_y,y,k_x,L-L} \tag{2.20}$$

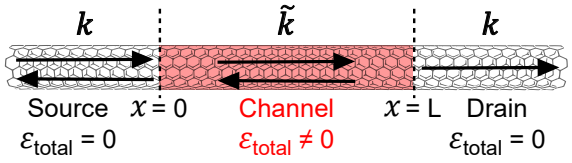

Figure 2.7: Diagram showing a 1D representation of the reflection and transmission of charge carriers across a strained SWCNT channel and unstrained SWCNT source/drain contacts. The source-channel and channel-drain boundaries are located at $x = 0$ and $x = L$, respectively.

Note that the coefficient a_N has dropped out. We can then obtain the transmission amplitude of N-th mode by solving Eq. 2.19 and Eq. 2.20:

$$t_N = \frac{k_x \tilde{k_x} v_{xx}}{k_x \tilde{k_x} v_{xx} \cos\left(\tilde{k_x} L\right) - i\left(-k_y \tilde{k_y} v_{yy} + \mathrm{sgn}(k_F \tilde{k_F}) \sqrt{(k_x^2 + k_y^2)((\tilde{k_x} v_{xx})^2 + (\tilde{k_y} v_{yy})^2)}\right) \sin\left(\tilde{k_x} L\right)} \tag{2.21}$$

where $k_F = \mu_{\text{contact}}/(\hbar v_F)$ is the magnitude of the Fermi wave vector in the contacts, and L is the channel's length. The transmission probability of the N-th mode is given by $|t_N|^2$:

$$T_N = \frac{(k_x \tilde{k_x} v_{xx})^2}{(k_x \tilde{k_x} v_{xx})^2 \cos^2(\tilde{k_x} L) + (k_F \tilde{k_F} - k_y \tilde{k_y} v_{yy})^2 \sin^2(\tilde{k_x} L)} \tag{2.22}$$

The only remaining unknown term is the quantized y-momentum $\widetilde{k_y}$, which will be discussed later. By summing over all conduction modes, one can find the ballistic conductance in strained SWCNTs:

$$G = \frac{4e^2}{h} \sum_{N=0}^{N_{\max}} T_N \tag{2.23}$$

where the number of modes in the summation, $N_{\max}$, is determined by the contact potential $\hbar v_{\mathrm{F}} k_y \leq \mu_{\text{contact}}$, and the factor of 4 arises from the spin and valley degeneracies. For quasi-metallic nanotube contacts, the energy difference between two adjacent modes (i.e. subbands) is determined by the diameter due to its periodic boundary condition along the circumference: $\Delta k_y = 2/d$. Because the diameter of any single-wall carbon nanotube is very likely smaller than 2.0 nm [81], the minimum subband energy spacing is ≈ 0.6 eV. Because μ_{contact} is lower than this value experimentally, there is a single conduction mode ($N_{\max} = 0$) in our quasi-metallic SWCNT transistors.

When uniaxial strain is applied to SWCNTs, both the nearest-neighbour carbon atom distances and the hopping amplitudes between atoms are modified. These two types of changes can be described by the gauge potentials $\boldsymbol{A}_{i,\text{lat}}$ and $\boldsymbol{A}_{\text{hop}}$, respectively [46]. The total vector potential $\boldsymbol{A}_{\mathrm{i}} = \boldsymbol{A}_{\mathrm{i,lat}} + \boldsymbol{A}_{\text{hop}}$ indicates the shift of the Dirac points under strain in K_{i} valley, where $i = 1, 2, 3$. By symmetry, $\boldsymbol{A}'_{\mathrm{i}}$ in the K'_{i} valleys are equal to $-\boldsymbol{A}_{\mathrm{i}}$. The $\boldsymbol{A}_{\mathrm{i}}$ are given by Eq. 2.24:

$$\boldsymbol{A}_{\text{hop}} = \frac{\beta\varepsilon(1+\nu)}{2a} \begin{pmatrix} \sin 3\theta_h \\ \\ \cos 3\theta_h \end{pmatrix} \tag{2.24a}$$

$$\boldsymbol{A}_{1,\mathrm{lat}} = \frac{2\pi\varepsilon}{3a}\begin{pmatrix} -\cos\theta_h - \frac{1}{\sqrt{3}}\sin\theta_h \\ \frac{1}{\sqrt{3}}\nu\cos\theta_h - \nu\sin\theta_h \end{pmatrix} \tag{2.24b}$$

$$\boldsymbol{A}_{2,\mathrm{lat}} = \frac{2\pi\varepsilon}{3a}\begin{pmatrix} \cos\theta_h - \frac{1}{\sqrt{3}}\sin\theta_h \\ \frac{1}{\sqrt{3}}\nu\cos\theta_h + \nu\sin\theta_h \end{pmatrix} \tag{2.24c}$$

$$\boldsymbol{A}_{3,\mathrm{lat}} = \frac{4\pi\varepsilon}{3\sqrt{3}a}\begin{pmatrix} \sin\theta_h \\ -\nu\cos\theta_h \end{pmatrix} \tag{2.24d}$$

Here, $a = 1.42$Å is the nearest neighbor carbon-carbon distance under zero strain. θ_h is the chiral angle defined by the chiral vector $\boldsymbol{C}_\mathrm{h} = n\boldsymbol{a}_1 + m\boldsymbol{a}_2$ with respect to the zigzag direction, where $\boldsymbol{a}_1$ and $\boldsymbol{a}_2$ are the unit vectors of the hexagonal carbon lattice (Fig. 2.8a) [47]. Note that the crystal orientation notation θ_h we use here differs from a similar quantity used in graphene devices [52], where a crystal angle θ was defined between the device's x-axis and zigzag direction. Fig. 2.8b shows how $\varepsilon_\mathrm{total}$ modifies linearly the y-components of the vector potentials, $A_{\mathrm{i},y}$, in a $(n = 12, m = 9)$ SWCNT where θ_h =25°.

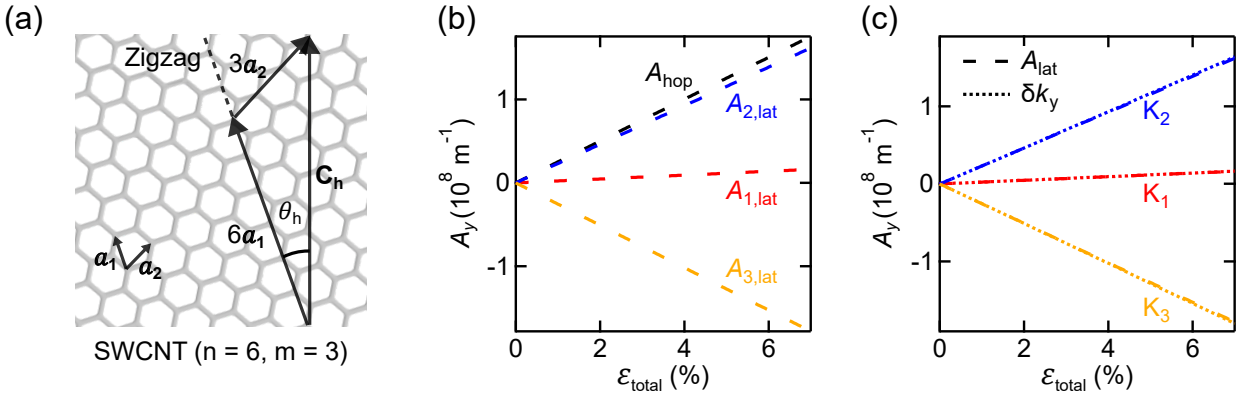

Figure 2.8: Chirality and strain-induced vector potentials in SWCNTs. (a) A $(n = 6, m = 3)$ SWCNT unrolled into a graphene ribbon. The chiral angle $\theta_h = 19°$, chiral vector $\boldsymbol{C}_\mathrm{h}$, and lattice vectors are shown. (b) $A_{\mathrm{i,lat},y}$ and $A_{\mathrm{hop},y}$ versus $\varepsilon_\mathrm{total}$ for a $(n = 12, m = 9)$ tube, with $\theta_h = 25°$. (c) The subband shifts $\delta\tilde{k}_{\mathrm{i},y}$ (dotted lines) versus $\varepsilon_\mathrm{total}$ always exactly cancel the $A_{\mathrm{i,lat},y}$ shifts(dashed lines). The quantities shown are for a (12,9) tube.

While applying a uniaxial strain along the tube axis, the circumference of the tube decreases by $\varepsilon_{yy} = -\nu\varepsilon_{\text{total}}$. Thus, the periodic boundary condition along the circumference becomes:

$$\tilde{k_y}(1+\varepsilon_{yy})C_h = 2\pi N \tag{2.25}$$

where N is an integer. As shown in the main text Fig. 2a, when there is no strain, the subbands (black dashed lines) pass through the Dirac points in quasi-metallic nanotubes. Meaning that there is a zero y-momentum $\tilde{k_y} = 0$ component in the allowed subband. When strain is applied, the subbands (red dashed lines) move as shown in Fig. 2a and $\tilde{k_y}$ in K_i valley is determined both by the Dirac points shift $A_{i,y}$ and the subbands shift $\delta\tilde{k}_{i,y}$. For example, in a quasi-metallic SWCNT ($n = 12, m = 9$) under 4% strain, $A_{1,y} = 1.1 \times 10^8$ m^{-1}, $A_{2,y} = 2.0 \times 10^8$ m^{-1}, $A_{3,y}$ = -0.02 $\times 10^8$ m^{-1}, while $\delta\tilde{k}_{1,y} = 0.1 \times 10^8$ m^{-1}, $\delta\tilde{k}_{2,y} = 1.0 \times 10^8$ m^{-1}, $\delta\tilde{k}_{3,y}$ = -1.02 $\times 10^8$ m^{-1}. The strain-induced change in $\tilde{k_y}$ is given by $\delta\tilde{k}_{i,y} - A_{i,y}$ which gives -1.0 $\times 10^8$ m^{-1} for all K_i valleys. Fig. 2.8c shows that $\delta\tilde{k}_{i,y}$ is always equals to the lattice-induced term $A_{\text{i,lat},y}$ under different strain. Thus, in general,

$$\tilde{k}_y = k_y - A_{i,y} + \delta\tilde{k}_{i,y} = k_y - (A_{\text{i,lat},y} + A_{\text{hop},y}) + A_{\text{i,lat},y} = k_y - A_{\text{hop},y} \tag{2.26}$$

We can use Eq. 2.26 to simplify Eq. 2.22, and obtain:

$$T_\xi = \frac{(k_x\tilde{k_x}v_{xx})^2}{(k_x\tilde{k_x}v_{xx})^2\cos^2(\tilde{k_x}L) + (k_F\tilde{k_F} - k_y(k_y - \xi A_{\text{hop},y})v_{yy})^2\sin^2(\tilde{k_x}L)} \tag{2.27}$$

where ξ = 1 (-1) in the K_i (K_i') valley, $\tilde{k_F} = |\tilde{\boldsymbol{k}}|$, $k_F = |\boldsymbol{k}|$, $k_x = \sqrt{{k_F}^2 - {k_y}^2}$, $\tilde{k_x} = {v_{xx}}^{-1}\sqrt{{\tilde{k_F}}^2 - {v_{yy}}^2{\tilde{k_y}}^2} = {v_{xx}}^{-1}\sqrt{{\tilde{k_F}}^2 - {v_{yy}}^2(k_y - \xi A_{\text{hop},y})^2}$. By summing over all valleys, the conductance of the nanotube transistor is finally obtained as

$$G = \frac{4e^2}{h}\frac{1}{2}\sum_\xi T_\xi \tag{2.28}$$

From Eq. 2.27 and Eq. 2.28, we can calculate the conductance of a strained SWCNT device at any gate-induced energy shift $\Delta\mu_{\text{G}}$. However, in experiments, it is rather a gate voltage V_{G} that is applied to the device. In the following, we discuss how to convert $\Delta\mu_{\text{G}}$ to V_{G}.

In our proposed SWCNT devices, the channel and the gate (silicon substrate) form a capacitor. Its capacitance is determined by both the usual geometric capacitance C_{G} and a quantum capacitance C_{DOS} stemming from the density of states in the SWCNT [76]:

$$C_{\mathrm{total}}^{-1} = C_{\mathrm{DOS}}^{-1} + C_{\mathrm{G}}^{-1} \tag{2.29}$$

where C_{G} is given by Eq. 2.10 above, and C_{DOS} is:

$$C_{\mathrm{DOS}} = e^2 g(\mu_{\mathrm{channel}}) \tag{2.30}$$

where $g(\mu_{\mathrm{channel}})$ is the density of states at the chemical potential $\mu_{\mathrm{channel}} = \Delta\mu_{\mathrm{G}} + e\phi_{\varepsilon}$. As noted above, a band gap in strain-induced in quasi-metallic SWCNT, and its value is simply: $E_{\mathrm{gap}} = 2\hbar v_F |A_{\mathrm{hop},y}|$. Then, $g(\mu_{\mathrm{channel}})$ can be written as:

$$\begin{aligned} g(\mu_{\mathrm{channel}}) &= \frac{4}{\pi\hbar v_{\mathrm{F}}}\left[1 - (E_{\mathrm{gap}}/2\mu_{\mathrm{channel}})^2\right]^{-1/2} \\ &= \frac{4}{\pi\hbar v_{\mathrm{F}}}\left[1 - (\hbar v_F |A_{\mathrm{hop},y}|/\mu_{\mathrm{channel}})^2\right]^{-1/2} \end{aligned} \tag{2.31}$$

The above capacitances determine the conversion ratio between the gate voltage and chemical potential [76]:

$$\frac{\mathrm{d}V_{\mathrm{G}}}{\mathrm{d}\mu_{\mathrm{channel}}} = \frac{C_{\mathrm{DOS}}}{eC_{\mathrm{tot}}} \tag{2.32}$$

One can then find the gate voltage V_{G} from the gate energy $\Delta\mu_{\mathrm{G}}$:

$$V_{\mathrm{G}} = \frac{1}{e}\int_0^{\Delta\mu_{\mathrm{G}}} \frac{C_{\mathrm{DOS}}}{C_{\mathrm{tot}}} \mathrm{d}\Delta\mu_{\mathrm{G}} \tag{2.33}$$

Note that because C_{DOS} is strain-dependent, the V_{G} giving a specific $\Delta\mu_{\mathrm{G}}$ is not the same at different strains.

2.3 Mechanical Aharonov-Bohm effect in quasi-metallic SWCNTs

2.3.1 Main results

Quantum transport circuits [5, 6, 12] are usually manipulated via multiple electric and magnetic fields, but their mechanical degrees of freedom mostly remains unused and poorly

controlled. A precise mechanical control of quantum transport phases would add both new functionalities and reduce quantum dephasing, due to mechanical disorder, in devices such as quantum bits, transmission lines, transistors, and NEMS.

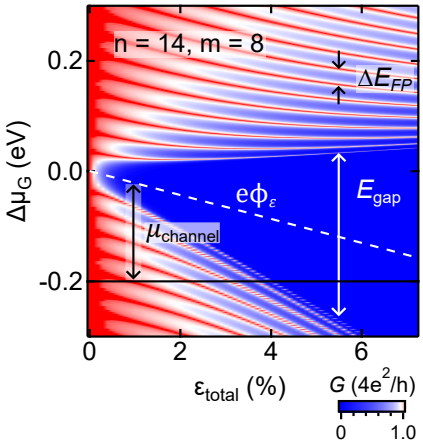

Figure 2.9: G-$\Delta\mu_{\rm G}$-$\varepsilon_{\rm total}$ data calculated for a (14,8) quasi-metallic tube. Strain opens a band gap, as shown by the blue region. A linear shift is created by the scalar potential energy $e\phi_\varepsilon$ (white dashed line). Clear FP resonances, with spacing $\Delta E_{\rm FP}$, are visible.

Figure 2.9 shows $G-\Delta\mu_{\rm G}-\varepsilon_{total}$ data calculated using Eq. 2.6 for a (14,8) quasi-metallic tube (similar data for a (12,9) tube are shown in Fig. 2.13(a). We readily notice four qualitative features. First, a band gap opens up as strain increases (blue region). Secondly, the center of this $G=0$ region (off state) is shifting linearly downward with strain due to $e\phi_\varepsilon$. Thirdly, even outside the bandgap region, G is decreasing as ε_{total} increases (see also Fig. 2.6). Finally, we observe sharp G interferences whose energy spacing is $\Delta E_{\rm FP}\approx hv_{\rm F}/2L\approx$ 36 meV, where $L=50$ nm is the length of the channel. The positions of these interferences shift with strain. We first seek to describe quantitatively the strain-dependence of these Fabry-Pérot (FP) interferences in terms of electron trajectories as a function of ε_{total}.

Figure 2.10(a) shows the charge carriers' trajectories in quasi-metallic SWCNTs, in the first and only occupied subband, when $\varepsilon_{\rm total}=0$ (top diagram) and $\neq 0$ (bottom diagram). As discussed above, the effect of strain is two fold. First, $e\phi_\varepsilon$ modifies the magnitude of the Fermi wavevector in the channel. For example, when $V_{\rm G}>0$ then $e\phi_\varepsilon$ increases $\mu_{\rm channel}$ and $|\tilde{\boldsymbol{k}}|$. Secondly, $A_{i,y}=\pm A_{hop,y}$ modifies the orientation of $\tilde{\boldsymbol{k}}$. The current flows at a propagation angle $\pm\Theta=sin^{-1}(A_{hop,y}/|\tilde{\boldsymbol{k}}|)$ with respect to the tube's axis.

It is well known [1], and consistent with Eq. 2.27, that G strongly depends on Θ in SWCNTs and graphene. What is unique about the present devices is that a purely mechanical degree of freedom, uniaxial-strain, permits a precise control of Θ over its entire range from

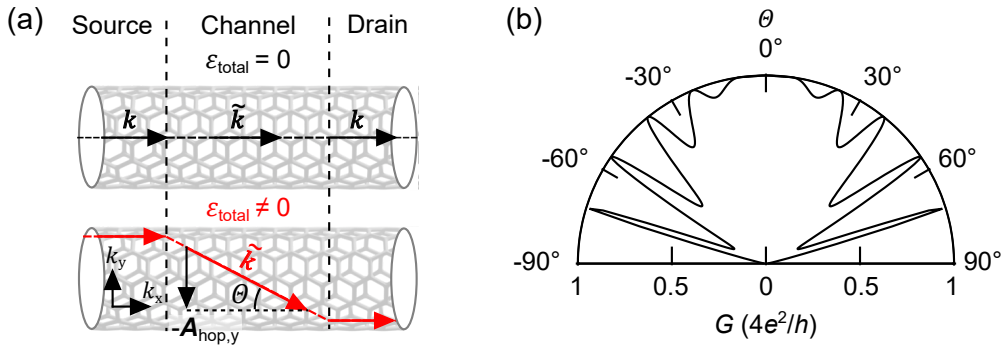

Figure 2.10: Mechanical control of the propagation angle and transmission probability of charge carriers. (a) Trajectory of charge carriers in the first subband of quasi-metallic nanotubes under zero (black line) and finite (red line) strain. The charge carrier propagation angle Θ is strain tunable. (b) Polar plot of G versus Θ for a (14,8) tube when $\mu_G = -0.2$ eV, i.e. along the black cut in Fig. 2.9.

0^o to 90^o. Figure 2.10(b) shows the transmission probability, T, and $G = 4e^2/hT$ vs Θ in a quasi-metallic (14,8) transistor. Clear oscillations (interferences) of G vs. Θ are visible. The relationship between Θ and ε_{total} is shown in Fig. 2.11.

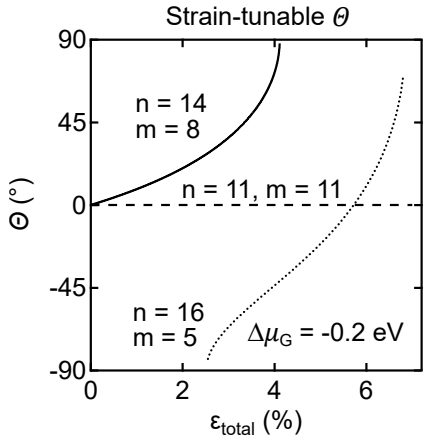

Figure 2.11: Strain controls Θ in all quasi-metallic (e.g. $n = 14$, $m = 8$ data shown as a solid line) and semi-conducting (e.g. $n = 16$, $m = 5$ data shown as a dotted line) SWCNTs. However, Θ is independent from ε_{total} in armchair tubes (e.g. $n = 11$, $m = 11$ data shown as a dashed line).

The black data in Fig. 2.11 is extracted along the horizontal black cut in Fig. 2.9 at $\mu_{\text{channel}} = $ -0.2 eV. The transmission angle Θ evolves smoothly from 0^o to 90^o as ε_{total} changes from 0 to $\approx$ 4 %. The Θ =90^o point corresponds to crossing into the band gap region in Fig. 2.9. For completeness, We show in Fig. 2.11 that a similar control of Θ is possible in other types of SWCNTs. The dotted data are for a semiconducting (16,5) tube. The only

instance when Θ is not strain-tunable is in armchair tubes, as shown by the dashed (11,11) data. Our prediction of a precise mechanical control of Θ and G in quasi-metallic SWCNT transistors is robust over a broad range of tube diameters beyond $d = 1.5$ nm. For instance, we show in Sec. 2.3.2 that the picture is unchanged for 1.0 nm $< d <$ 2.0 nm. We mention that to observe most clearly the transport features in Fig. 2.9, the temperature needs to be of the order of several Kelvin or lower to satisfy the relationship: $k_{\mathrm{B}}T, eV_{\mathrm{B}} \backsim 1$ meV $\ll \Delta E_{\mathrm{FP}} < e\phi_{\varepsilon} < E_{\mathrm{gap}}, \mu_{\mathrm{contact}}$. The strain-dependence of the FP interferences in Fig. 2.9 also implies a mechanical control of the quantum phase of charge carriers. We now discuss this phase control and how it could be used in devices.

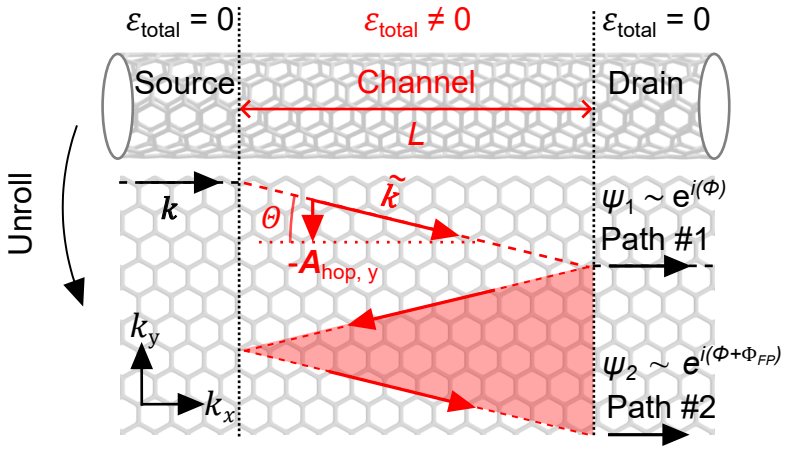

Figure 2.12: Diagram of the charge carriers trajectories across a quasi-metallic SWCNT channel under strain. Paths #1 and #2 interfere with a phase difference Φ_{FP} which depends on Θ and is mechanically tunable.

Figure 2.12 is a diagram representing the two most likely paths followed by ballistic charge carriers across a quasi-metallic SWCNT channel under strain. Path #1 is a single passage across the channel at a transmission angle $\Theta = sin^{-1}(A_{hop,y}/|\tilde{\boldsymbol{k}}|)$. Path #2 is for charge carriers which are reflected upon first encountering the channel-drain interface, but transmitted into the drain contact upon their second attempt. Higher order terms (paths) which involves more reflections, and make smaller contributions to G, are not shown for clarity.

The measured transmission probability T, and conductance G, is obtained by squaring the sum of the amplitudes of these superposed paths. Therefore, G will oscillate as a function of the additionnal Fabry-Pérot phase Φ_{FP} acquired along path #2. That Φ_{FP} and interference amplitude ΔG can be tuned electrostatically is a well established result [82, 83]. What is

new, and technologically useful, is that $\Phi_{\rm FP}$ and ΔG can also be tuned entirely mechanically.

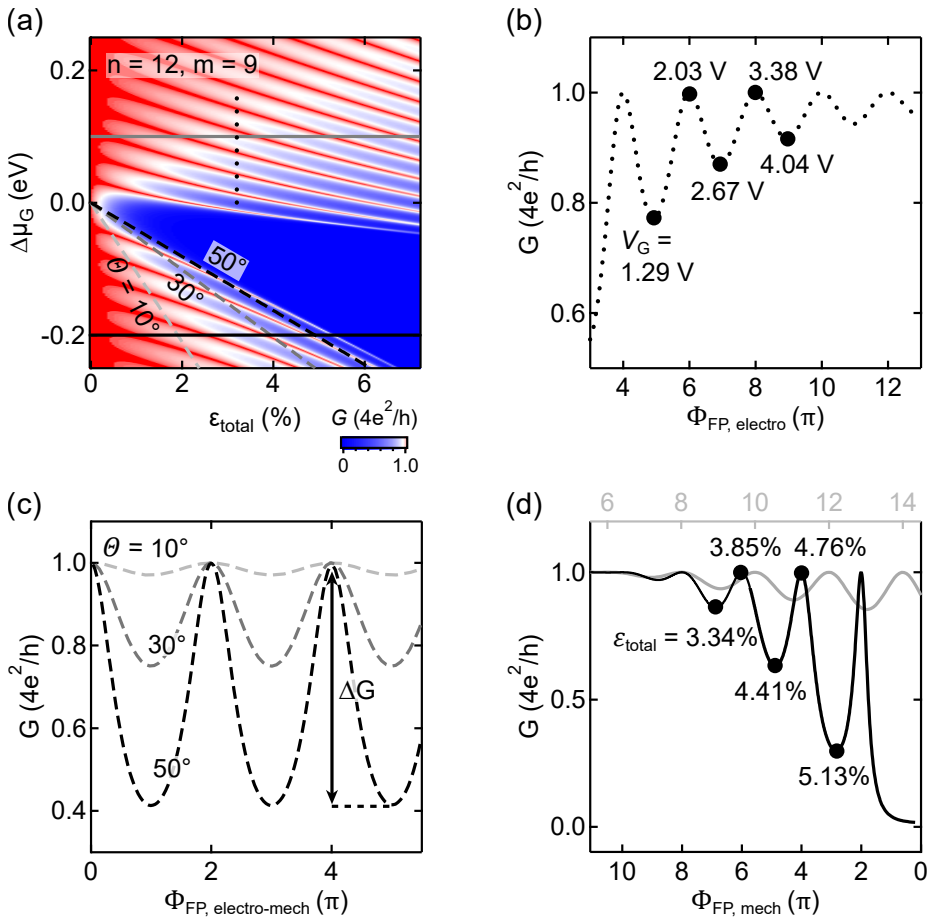

Figure 2.13: Mechanical control of the quantum transport phase in nanotube transistors. (a) Calculated $G - \Delta\mu_{\rm G} - \varepsilon_{\rm total}$ data for a (12,9)-SWCNT transistor. (b) Data extracted along the vertical dotted line in panel (a). These G interferences are tunable electrostatically using $V_{\rm G}$. (c) Data extracted along the tilted dashed lines in panel (a) where $\Theta = 10^o$, 30^o, and 50^o. The G oscillations are tunable using a combination of electrostatic, $V_{\rm G}$, and mechanical potentials ϕ_ε, $A_{hop,y}$. (d) Data extracted along the horizontal solid lines in panel (a). The G interferences are fully tunable using only the mechanical potentials.

Figure 2.13(a) shows the $G - \Delta\mu_{\rm G} - \varepsilon_{total}$ for a (12,9) quasi-metallic tube (similar data for a (14,8) tube are shown in Fig. 2.9). The oblique dashed lines in the bottom left of the panel show data cuts at $\Theta = 10$, 30, and 50^o. Along these constant angle cuts it is easier to calculate $\Phi_{FP} = \oint \tilde{\boldsymbol{k}} \cdot \boldsymbol{dl}$ where $\boldsymbol{dl}$ is the displacement around the shaded-red triangular loop in Fig. 2.12. Note that $\boldsymbol{A}$ is constant everywhere in the channel, and only the $\tilde{k_x}$ component is inverted when the wavefunction is reflected. We thus find $\Phi_{\rm FP} = 2\tilde{k_x}L$. This is fully consistent with Eq. 2.27 whose phase dependence origins from the functions $sin^2(\tilde{k_x}L)$ and $cos^2(\tilde{k_x}L)$.

Using the model in Section 2.2, we can re-write $\tilde{k_x}$ to better visualize the strain dependence of $\Phi_{\rm FP}$ as

$$\Phi_{\rm FP} = 2\sqrt{[(\Delta\mu_{\rm G} + e\phi_\varepsilon)/(\hbar v_{\rm F})]^2 - (A_{{\rm hop},y} v_{yy})^2}(\frac{L}{v_{xx}}) \tag{2.34}$$

Equation 2.34 highlights that Φ_{FP} can be controlled via ϕ_ε and $A_{{\rm hop},y}$, which are both proportional to $\varepsilon_{\rm total}$. This mechanical control of quantum interferences is closely analogous to the usual *electrostatic* Aharonov-Bohm (AB) phase, where an electrostatic potential can be used to tune G interferences [70, 71]. We can verify this analogy by comparing the mechanical tuning of the phase, $\Phi_{\rm FP,mech}$, and the electrostatically-induced phase $\Phi_{\rm FP,electro}$ controlled via $V_{\rm G}$.

Figure 2.13(b) shows G - $\Phi_{\rm FP,electro}$ data extracted along the vertical dotted line in Fig. 2.13(a). The only parameter tuning the FP phase along this cut is the electrostatic potential $V_{\rm G}$. For instance, $\Phi_{\rm FP,electro}$ can be changed by π, and G from a local minimum to a maximum, betIen $V_{\rm G}$ = 1.29 V and 2.03 V. Many full oscillations of $\Phi_{\rm FP,electro}$ are possible over the experimentally available $V_{\rm G}$ range of ± 15 V.

In Fig. 2.13(c), we show data extracted along the tilted dashed lines, in Fig. 2.13(a), for which $\Theta = 10^o$, 30^o, and 50^o. Many complete G oscillations are visible along these cuts. To move along these constant Θ cuts, and tune $\Phi_{\rm FP,electro\text{-}mech}$ and ΔG, one must adjust both the electrostatic, $V_{\rm G}$, and mechanical potentials, ϕ_ε, $A_{{\rm hop},y}$.

Lastly, in Fig. 2.13(d), we show G interferences which are controlled solely via the mechanically-generated potentials. These data cuts are extracted parallel to the ε_{total} axis in Fig. 2.13(a) and show many complete oscillations of G. For instance, in the black trace a full 2π change in $\Phi_{\rm FP,mech}$ is created by changing $\varepsilon_{\rm total}$ from 4.4 % to 5.1%. The amplitude of the interferences ΔG can be engineered with strain and can become $\sim 4e^2/h$. The data in Fig. 2.13(d) constitute a mechanical analog to the electrostatic Aharonov-Bohm effect.

Collectively, the data in Fig. 2.13 make a clear prediction for realistic experiments: quasi-metallic SWCNT ballistic transistors can serve as coherent current sources whose phase is mechanically tunable. This additional degree of freedom to control the phase of current in quantum circuits, independently from electrostatics, opens new possibilities for previous work on SWCNT qubits and coherent transport devices [5, 6, 11].

2.3.2 Supporting material

Figure 2.13 shows the mechanical control of the quantum phase of current in a (12,9) SWCNT channel whose diameter $d \approx 1.5$ nm. To prove that this prediction is valid for a broad range

of quasi-metallic SWCNTs, we present below additional data for quasi-metallic tubes with different diameters and chiralities.

First, we look at a SWCNT with a similar diameter $d \approx 1.5$ nm, but a different chirality (14,8). Figure 2.14a is a G - $\Delta\mu_{\mathrm{G}}$ - $\varepsilon_{\mathrm{total}}$ color map for a (14,8) quasi-metallic tube. Comparing these data to the (12,9) data in Fig. 4(a), we notice that the blue region (bandgap) is wider, which indicates a larger $A_{\mathrm{hop,y}}$ in the (14,8) tube at the same strain. A clear pattern of interferences is observed in all cases. Fig. 2.14b shows the G data extracted along the grey and black cuts in Fig.2.14a, where $\Delta\mu_{\mathrm{G}} = 0.1$ eV and -0.2 eV, respectively. We note that changing $\varepsilon_{\mathrm{total}}$ from 3.5 % to 3.7 % suffices to change by π the phase of the G interference. Moreover, the amplitude of the interference is large and reaches up to $\Delta G/G_{\mathrm{max}} \approx 0.8$.

Next, we look at two SWCNTs with different diameters: $n = 9, m = 6$, $d \approx 1.0$ nm and $n = 16, m = 13$, $d \approx 2.0$ nm. There are clear interference patterns both in Fig. 2.14c and Fig. 2.14e. The latter has a smaller bandgap region. Figures 2.14d,f confirm that using the available $\varepsilon_{\mathrm{total}}$ range one can fully tune the G interferences in these tubes.

In our model, we incorporated three experimental parameters whose values were taken from literature: the contact region Fermi energy μ_{contact}, the scalar energy pre-factor g_{ε}, and the electronic Grüneisen parameter β. Their exact value has some uncertainty in literature and may also vary slightly in different SWCNT devices. In addition, we made two approximations when writing the Hamiltonian in Eq. 2.11, namely we included the tensile strain effects only to first-order and we did not include any shear (torsional) strain. In this section, we discuss the magnitude of the uncertainty introduced by theses parameters and approximations, and find that they do not introduce uncertainties on G beyond about 20%. The model is therefore sound for describing realistic experiments which typically have other experimental sources of uncertainty of a similar magnitude (e.g. the uncertainty on L can be around $\pm$ 10 nm [52, 63], which amounts to 20 % of $L = 50$ nm).

As stated earlier, when μ_{contact} is smaller than the minimum energy of the second subband, there is a single conduction mode in the channel. Here, we calculate the conductance with $\mu_{\mathrm{contact}} = 0.12$ eV and 0.25 eV in a SWCNT $n = 12, m = 9$. Both values are smaller than the required energy to reach the second subband, which is $\approx$0.60 eV. Fig. 2.15a shows the conductance under different strain at $\Delta\mu_{\mathrm{G}} = -0.2$ eV. We see clearly that μ_{contact} has no impact on the calculated G data, and thus does not introduce any significant uncertainty.

g_{ε} changes the scalar energy $e\phi_{\varepsilon} = g_{\varepsilon}(1-\mu)\varepsilon_{\mathrm{total}}$, which leads to lateral shifts of the gate voltage position of the charge neutrality point. Fig. 2.15b shows $G - V_{\mathrm{G}}$ curves calculated using different g_{ε} values. By increasing g_{ε} from 2.6 eV to 3.0 eV, which is approximately the

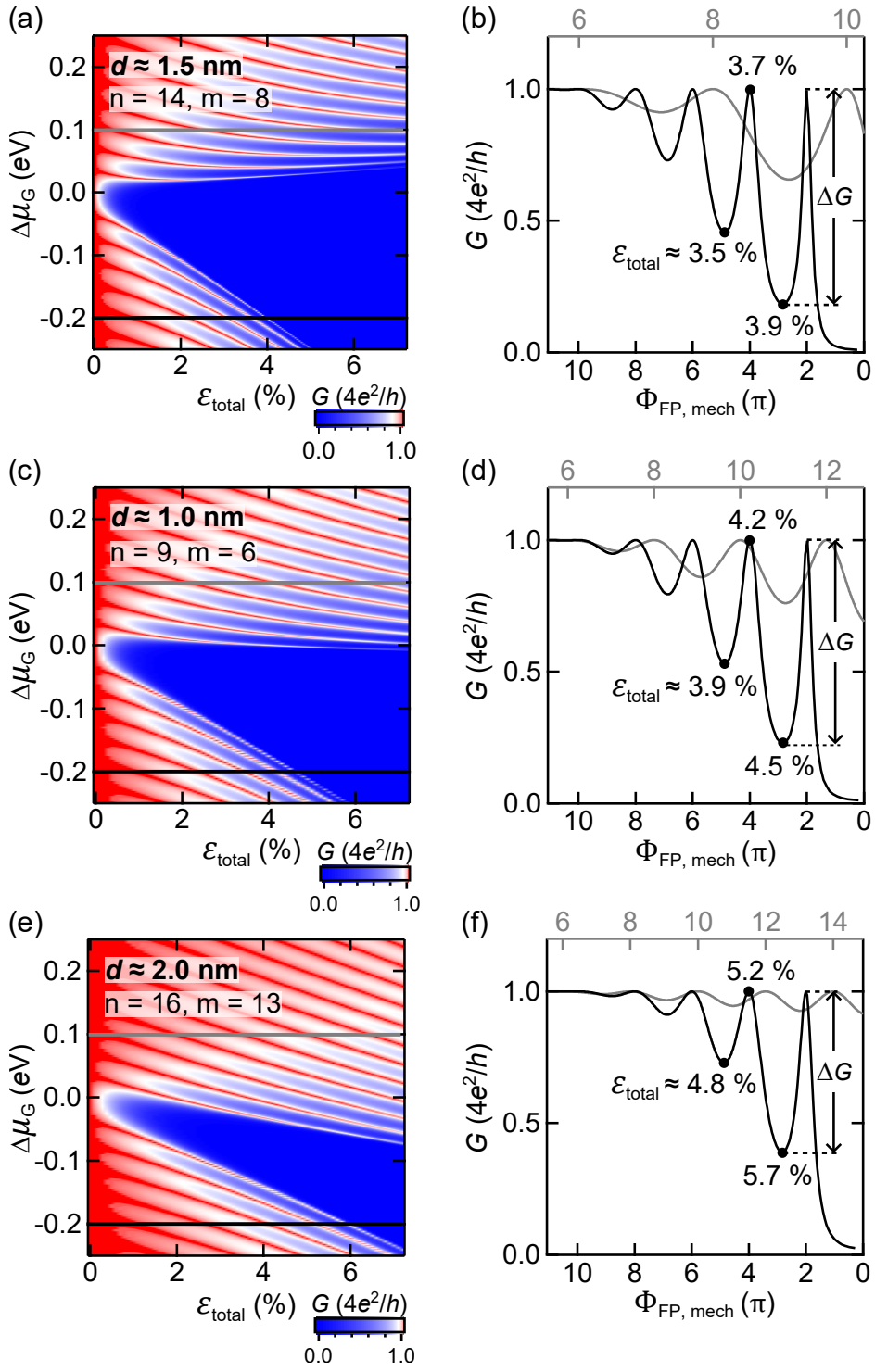

Figure 2.14: Transport data for strain transistors based on quasi-metallic SWCNTs of different diameters and chiralities. For a tube (14,8) with $d \approx$1.5 nm, (a) G - $\Delta\mu_G$ - ε_{total} data and (b) G - $\Phi_{FP,\,mech}$ data extracted from (a) along the grey and black cuts. For a tube (9,6) with $d \approx$1.0 nm, (c) G - $\Delta\mu_G$ - ε_{total} data and (d) G - $\Phi_{FP,\,mech}$ data extracted from (c) along the grey and black cuts. For a tube (16,13) with $d \approx$ 2.0 nm, (e) G - $\Delta\mu_G$ - ε_{total} data and (f) G - $\varphi_{FP,\,mech}$ data extracted from (c) along the grey and black cuts.

uncertainty range, the charge neutrality point shifts from $V_G \approx -1.8$ V to ≈ -3.1 V. Most importantly, the impact of uncertainty in g_ε is a rigid shift of the entire calculate G data spectra and does not change its features. Moreover, the amplitude of the rigid V_G shift is much smaller than the available experimental V_G range. This ensures that the uncertainty on g_ε does not introduce a meaningful error in connecting the calculated G to experimental measurements.

A reasonable range of uncertainty on β is shown in Fig. 2.15c, where the black and red data are calculated with $\beta = 2.5$ and 3.0, respectively. The difference between the two data sets shows that the uncertainty on β has only minor effects on the key features of G. For instance, the magnitude of its oscillations, the spacing between its maxima, and the ability to fully tune the phase of G mechanically are only slightly modified. Therefore, the calculated data present in the main text will lead to robust experimental features independently of the exact value of β .

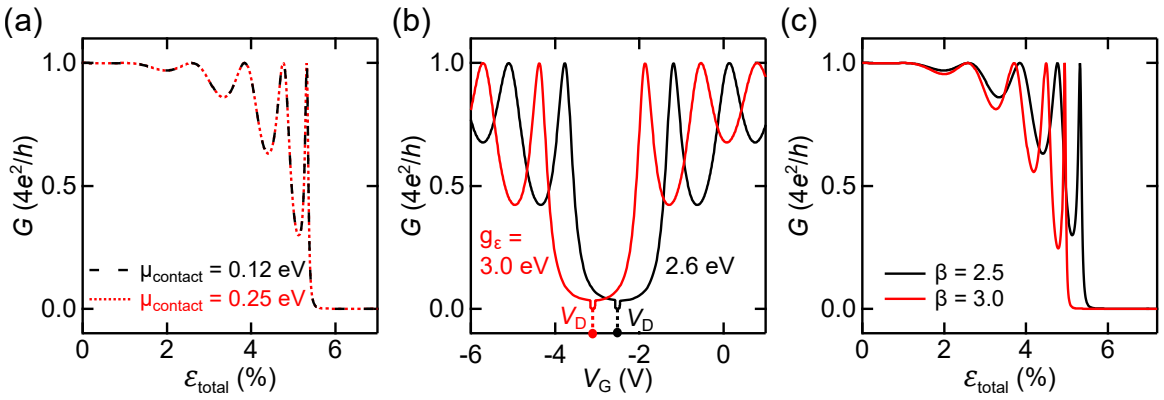

Figure 2.15: Impact of input parameters on simulations of our theoretical model. (a) G vs $\varepsilon_{\text{total}}$ at $\Delta\mu_G = -0.2$ eV in a quasi-metallic nanotube $n = 12, m = 9$. The dashed-black data and dotted-red data are calculated with $\mu_{\text{contact}} = 0.12$ eV and 0.25 eV, respectively. (b) G vs V_G at $\varepsilon_{\text{total}} = 4$ % in a quasi-metallic nanotube $n = 12, m = 9$. Black and red solid lines show the calculated data with $g_\varepsilon = 2.6$ eV and 3.0 eV, respectively. (c) G vs $\varepsilon_{\text{total}}$ at $\Delta\mu_G = -0.2$ eV in a (12, 9) tube. The black and red data are calculated with $\beta = 2.5$ and 3.0, respectively.

The expressions for the A_i in Eq. 2.24 and the strain tensor $\bar{\varepsilon}$ in Eq. 2.11 only consider first-order strain corrections and uniaxial strain. Here we discuss the impact of second-order strain corrections and/or unintentional torsional strain on G.

The wave vector $\tilde{\boldsymbol{k}}$ is modified by the strain-induced vector potentials. The second-order correction to $A_{\text{hop},y}$ will affect the propagation angle Θ and thus the transmission probability across the channel. Using the calculations of *Oliva-Leyva et al.* [84], the effect of including

second order strain corrections in a (14,8) tube changes $A_{\text{hop},y}$ from 3.3×10^8 m^{-1} to 3.6×10^8 m^{-1} for $\varepsilon_{\text{total}} = 7\%$. We see that even at the largest strains considered in our work, the inclusion of the second order corrections only represented a 10 % correction to the calculated A_{i}, and leads to a similar change in the calculated G. Given that experimental uncertainties in device dimensions [52] (i.e. nanofabrication) are typically $\geq$ 10 %, the first-order strain approximation still provides an accurate model to guide experiments.

Another source of uncertainty in connecting quantitatively experiments and theory could be if a torsional (shear) strain is present in the fabricated devices. From previous experimental work [63, 85], we know that a realistic upper bound for such spurious torsional strain is $\approx 1^\circ$. The dominant effect of such a shear strain in SWCNTs is the tuning of the bandgap. This torsion-induced bandgap is smallest for zigzag tubes and largest for armchair tubes [39]. For the SWCNTs mentioned in our work (quasi-metallic, $d \approx 1.5$ nm), a 1° torsion creates a bandgap of $\approx$ 140 meV. This energy scale is equivalent to the band gap generated by a tensile strain of 2.6%. The effect of this *maximal* spurious torsion is therefore smaller than the thermally-induced uniaxial strain $\varepsilon_{\text{thermal}} \approx 3.2\%$. Moreover, any built-in torsion during nanofabrication would remain constant while measuring a well-functioning QTS transistor (Fig. 1(a) of the main text). Thus, the only mechanically-tunable strain would remain the uniaxial $\varepsilon_{\text{mech}}$ (Fig. 1(b)). The impact of any torsional strain would therefore be equivalent to a rigid, and modest in magnitude, offset of the tunable strain range in the device. It would not lead to any qualitative change in our predictions for experiments: strain tunable bandgaps, strain tunable amplitude of the Fabry-Pérot interferences, and strain-controlled quantum phase of the transistor's current.

2.4 Conclusions

In conclusion, single-wall nanotubes are very narrow ribbons of 2D materials with atomically precise edges, making them ideal systems for QTS (quantum transport straintronics, i.e. using mechanical strain to control quantum transport). Their narrow widths means that it is realistic to build transistors whose transport involves a single subband, and where a single quantum phase describes the conductance or current. Here, we developed an applied theory, describing an existing experimental platform [52], to explore QTS and a mechanical Aharonov-Bohm effect in quasi-metallic SWCNTs.

A uniaxial mechanical strain $\varepsilon_{\text{total}}$ in a SWCNT creates a scalar, ϕ_ε, and vector, $\boldsymbol{A} = \boldsymbol{A}_{\text{lat},i} + \boldsymbol{A}_{\text{hop}}$, gauge potentials. The former is analogous to a mechanical gating effect or tuning of the work function. Its experimental signature differs quantitatively from the one

in graphene due to the differences in densities of states and quantum capacitances. The $\boldsymbol{A}$ potentials acting on the charge carriers are also distinct from the ones in graphene because of the periodic boundary condition in SWCNTs. The strain-dependent diameter of a tube generates a momentum-shift of its subbands, which cancels the $\boldsymbol{A}_{\text{lat}}$ component present in graphene [36]. This has an important consequence, charge carriers in all valleys of the SWCNT Hamiltonian have the same $|\boldsymbol{A}|$ and the same propagation angle $|\Theta|$. Thus, all charge carriers propagating across the transistor are coherent.

We showed that a realistic experimental range of $\varepsilon_{\text{total}} \approx 0$ - 7 % is more than sufficient to tune Θ from 0^o to 90^o, in a broad range of quasi-metallic SWCNTs. When $\Theta = 90^o$, G is reduced to zero as the channel's Fermi energy enters the band gap. The numerical value of the strain-tunable bandgap is in agreement with previous semi-classical calculations [68]. The calculated transport data $G - \Delta\mu_{\text{G}} - \varepsilon_{\text{total}}$ shows a rich set of quantum interferences which Ire not previously reported and discussed.

We explained this interference spectrum in terms of a phase Φ_{FP} added by the mechanically-induced potentials as well as by the electrostatic (gate) potential. In quasi-metallic SWCNTs, it is possible to tune Φ_{FP} with $\varepsilon_{\text{total}}$ over several 2π oscillations, as Ill as control the amplitude ΔG of the interferences. This effect can be interpreted as a mechanical analog of the electrostatic Aharonov-Bohm effect [70, 71].

This work opens many opportunities to explore and harness quantitative strain effects in quantum technologies [5, 6, 9, 11, 12, 86] and condensed matter physics [24, 83, 87, 88]. A detailed understanding of strain effects on quantum transport will also be useful to optimize existing transport devices based on 2DMs and their nanotubes, which are invariably subjected to strains inside heterostructures [53, 89]. We believe that experiment-ready applied theoretical models, such as the one presented here, can help accelerate the development of QTS in 1D and 2D materials.

Chapter 3

Experimental Methods for Quantum Transport Straintronics in SWCNTs

In this chapter, we describe the fabrication of suspended SWCNT junctions, their packaging for our custom-built QTS platform, and the preparation of nanoscale SWCNT channels. In Chapter 2, we proposed suspended SWCNT transistors on thin chips that allow in-situ tuning of mechanical strain during low-temperature transport measurements. Fabricating such devices presents challenges, including precise alignment of the tubes, long suspension length of the mechanical clamps. Aligning gold clamps on SWCNTs requires accurate nanotube coordinates, high electron beam imaging resolution and proper alignment of the electron beam lithography (EBL) pattern. Suspending devices without collapse requires knowledge of the needed etching depth and precise timing control when removing the SiO_2. To address these challenges, we improved the existing e-beam lithography procedure for more precise alignment and optimized the substrate etching parameters for accurate suspension control.

To make low-temperature transport measurements, we wire-bonded μm-sized contact pads connected to the nm-sized SWCNT junctions and then loaded them into a custom-built cryostat probe. The subsequent tasks include maintaining the cryostat and setting up the electrical circuits. We optimized the procedures for wire-bonding thin chips and loading them into the cryostat. In the earlier method, the loading process was very difficult for one person and typically required assistance from another, whereas the optimized procedure can now be performed reliably by a single person. These improvements have since been adopted by other members of the lab.

After cooling down, nanoscale SWCNT channels are created by electromigration of the gold bow-tie junctions covering them, and cleaned via Joule annealing. We fabricated eight devices, among which three SWCNT QDs and one graphene QD were studied in detail. The combination of their short 30 nm length and mechanical tunability had not been achieved

before and improved on the previous devices in our lab [63, 79]. Importantly, these are the first SWCNT devices enabling both in-situ strain tunability and quantum-transport measurements.

3.1 Fabrication of suspended SWCNT-under-Au junctions

In this section, we describe all fabrication steps to build nanoscale suspended SWCNT-under-Au junctions, starting from the localization and identification of SWCNTs, followed by the alignment and deposition of electrical contacts, and ending with the suspension of the junctions. In total, we have successfully fabricated six suspended SWCNT-under-Au junctions, each with a suspension length L_{sus} (indicated in Fig. 2.1) of ≈ 700 nm.

3.1.1 Localization and identification of SWCNTs

We grew carbon nanotubes on SiO_2-on-Si heavily doped substrate with a thickness of ≈ 200 μm, via chemical vapor deposition. Details of the growth process are provided in Refs. [49,90,91]. We then deposited L-shaped Au marks (labeled in Fig. 3.1) on the substrate surface to index the SWCNT positions. These marks were fabricated by photolithography and thermal evaporation [91] and were later used to align Au clamps on top of the SWCNTs using EBL. Next, we determined the nanotube positions using scanning electro microscopy (SEM) imaging and identified single-wall tube by their diameters [81] as measured with atomic force microscopy (AFM). To assign precise position coordinates to individual nanotubes relative to our alignment Au marks, the SEM magnification and resolution must be optimized to obtain a clear image with minimal carbon contamination. The maximum magnification used should include one $100\,\mu\text{m} \times 100\,\mu\text{m}$ grid (Fig. 3.1) to have both Au marks and nanotubes in the image. Carbon nanotubes were grown on chips patterned with an 40×40 array of these grids and imaging the entire chip grid by grid is not practical, as it is overly time-consuming and inefficient. To overcome this challenge, we optimize the SEM parameters such that nm-sized carbon nanotubes give μm-sized contrast at a low magnification. We find that with an accelerating voltage of 1.00 keV, a beam current of 0.15 nA, and a working distance of 6.0 mm, carbon nanotubes appear bright and distinguishable. This optimization enables us to rapidly locate tubes at a magnification as low as $\times 620$, as shown in Fig. 3.1. From our experience, carbon nanotubes with slight wrinkles are very likely to be single-walled, whereas multi-walled nanotubes typically appear straighter.

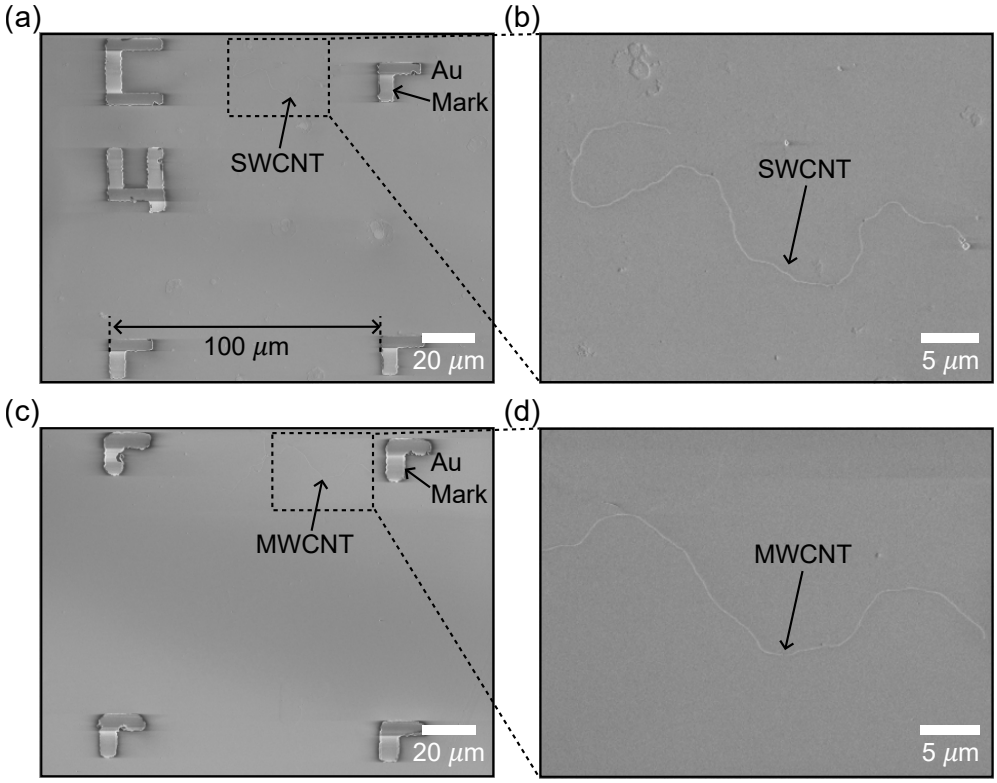

Figure 3.1: SEM images of our CNTs. (a) A SWCNT lies within the dashed rectangular area near the Au marker. (b) The zoom-in image clearly reveals the SWCNT with multiple small wrinkles. (c)-(d) A MWCNT appears to be more straight and rigid.

AFM measurements were performed to determine the nanotube diameters and indicate whether they are single-walled. The measurements are carried out in tapping mode using tips with radii smaller than 10 nm, a resonant frequency of ≈ 300 kHz, and a force constant of ≈ 40 N/m. To obtain high-quality AFM images, we use a scan rate of 0.5 Hz (corresponding to a tip velocity of 1.0 μm/s) with 512 sample points per line. The amplitude setpoint and feedback parameters are optimized to achieve accurate measurements while avoiding nanotube damage. Figure 3.2 shows AFM images of a SWCNT and a MWCNT, where the z axis indicates the nanotube height.

To minimize uncertainty in the diameter, we extract height profiles from multiple linecuts taken at different positions along the nanotube, as shown in Figure 3.3. The substrate background (black solid line) is obtained by fitting data from regions away from the nanotube and is then subtracted to improve accuracy. Figures 3.3(c)–(d) determined the carbon-nanotube diameters to be 1.6 ± 0.5 nm and 3.7 ± 0.5 nm, corresponding to the SWCNT and MWCNT shown in Figures 3.2(a)–(b). Note that van der Waals forces between the AFM tip and the nanotube can slightly affect the measured diameter [92, 93], and we accounted for

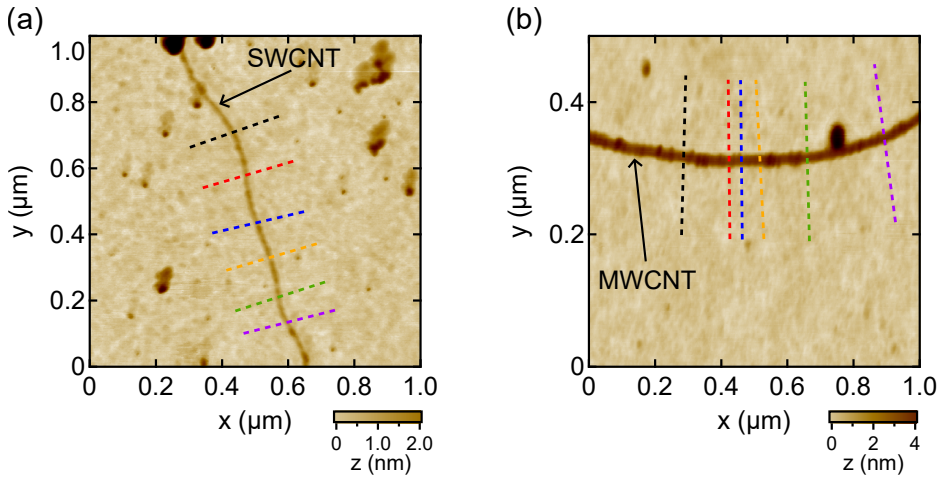

Figure 3.2: AFM images of our CNTs. (a)-(b) AFM images of the SWCNT and MWCNT shown in Fig. 3.1 (b) and (d), respectively.

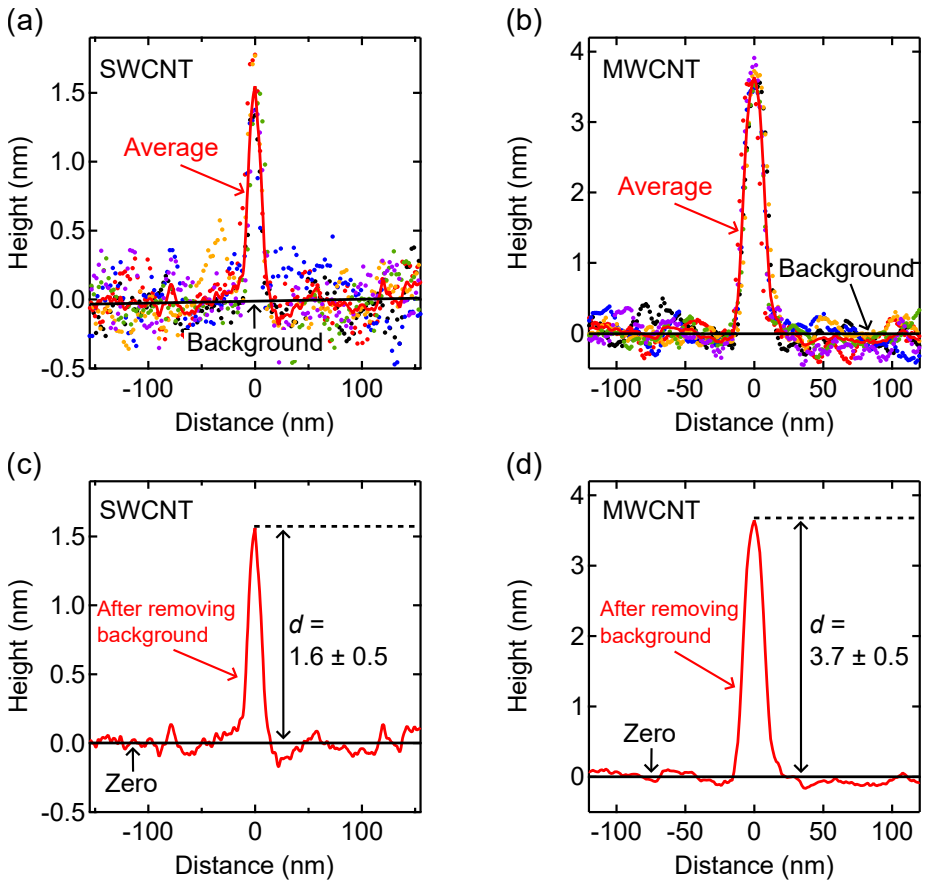

Figure 3.3: CNT diameter determination. (a)-(b) Dots are measured heights across the six linecuts shown in Fig. 3.2, with different color indicating the corresponding linecut. The background (black solid line) is determined by fitting the data from regions away from the nanotube sections, while the red solid line represents the average of all linecuts. (c)-(d) The SWCNT has a diameter of 1.6 ± 0.5 nm, while the MWCNT has a diameter of 3.7 ± 0.5 nm.

this effect by including an additional 0.2 nm uncertainty in the reported ±0.5 nm. Following Ref. [81], nanotubes with diameters smaller than 2 nm are most likely SWCNTs. SWCNTs with long horizontal sections are then selected for subsequent fabrication.

3.1.2 Alignment and deposition of Au clamps and contact pads

For standard DC transport measurements, electrical contacts are required to apply bias and gate voltages and to measure the current through the devices. We used Au films for electrical connections, as well as for mechanical clamping. The Au clamps must be very narrow, on the order of ≈ 200 nm, so that they can be broken in a controlled manner via electromigration (a technique used to create a nanogap in Au, discussed in Section 3.3). Because SEM imaging is performed at low magnification to minimize carbon contamination, and nanotubes appear to be on the micrometer scale while they are actually nanometer-sized, aligning and depositing narrow Au contacts with precision is highly challenging. We managed to optimize the alignment procedure and achieve a yield of 86 %, with 18 out of 21 alignments being successful. Large Au contact pads are then deposited to be used as wirebonding terminals. Aluminium wires are used for wirebonds. In this subsection, we present the optimized procedures for aligning and depositing Au clamps and contact pads using electron-beam lithography (EBL) and photo-lithography. Details including the coating and developing of resists, lithography parameters, Au film deposition are provided in previous work [91] and are not repeated here.

We first load the substrate in the EBL system and establish a coordinate system with the origin at the center of four 'L-shaped' Au marks, as shown in 3.4(a). The coordinates of the target SWCNT sections can then be determined. We select the horizontal sections because they are aligned with the bending direction of our chips. Figure 3.4(b) shows a CAD design of an EBL pattern where the bow-tie junction width is 200 nm, narrow enough to facilitate electromigration but not so narrow as to risk missing the nanotube. To achieve precise alignment, 'L' corners have to very sharp to provide clear reference positions. In cases where the "L" corners are unfortunately not well defined, distinctive features are used as reference. To further improve accuracy, we can also overlay the SEM image of the grids taken before EBL, with the one obtained during EBL. This is particularly useful when a thick bilayer resist is coated on the chip, because the beam focuses on the resist surface and the Au marks beneath the resist are often blurry. Overlaying these two images helps achieve better alignment. The e-beam spot resolution is also crucial, and the best results we obtain are beam width in the range of 10–20 nm. A gold junction without any SWCNT is

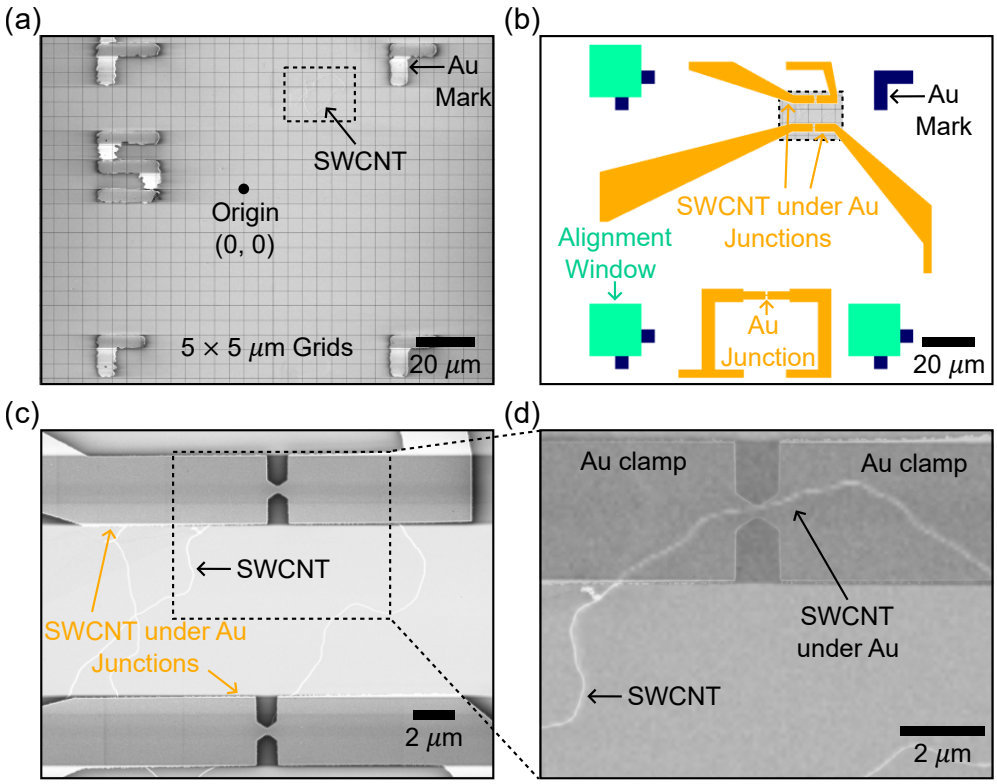

Figure 3.4: Deposition of Au clamps. (a) 5×5 μm mesh is drawn on a SEM image to create a coordinate system for CAD design. Origin is located at the center of four 'L' corners. (b) Arms (colored in gold) are designed to connect the nm-sized SWCNT and μm-sized large contact pads. Green squares are alignment windows for aligning the device with the CAD design. (c) A SEM image of junctions on the SWCNT after EBL. (d) Semi-transparent SWCNT SEM image is superposed on the top junction in panel (c) to check the alignment. It clearly shows that the nanotube is under the junction.

also fabricated, as shown at the bottom of the EBL design, for practicing electromigration and calibrating mechanical motion. Figure 3.4(c) presents the final result after EBL and Au deposition. Au clamps are positioned on top of the horizontal SWCNT segments. Alignment can be verified by overlaying the SWCNT SEM image taken before and after EBL, as shown in Fig. 3.4(d).

The deposited Au arms have a maximum width of $\sim$20 μm, which is insufficient for bonding 38 μm aluminum wires. To ensure reliable wire-bonding, we add $200 \times 200, \mu$m contact pads connected to the EBL pattern, as shown in Fig. 3.5. A 3 nm chromium adhesion layer was placed under Au to improve stickiness, but it was omitted in the EBL pattern to avoid introducing unnecessary disorder. This later step was done with photo-lithography, detailed in previous work [91]. The SWCNT-under-Au junctions are now sitting on the SiO_2/Si substrate, and are ready for suspension.

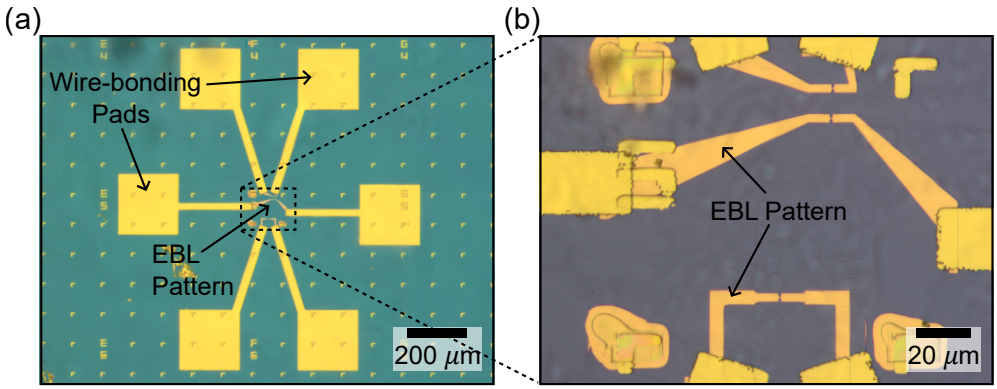

Figure 3.5: Deposition of large contact pads. (a)-(b) Optical images showing six contact pads fabricated with photo-lithography. These pads are used to bond aluminum wires for electrical transport measurements.

3.1.3 Suspension of SWCNT-under-Au junctions

The final clean room fabrication step is etching the SiO_2 to suspend the gold junctions. Suspension helps avoid the disorder from the substrate and increases the channel elongation under the same bending deformation of the chip [73]. This step is performed by removing the substrate surface with a wet buffer oxide etch (BOE). While etching more can achieve a longer suspension length for larger mechanical strain, it is also important to keep the junctions from collapsing. We first clean the substrate surface to remove carbon and resist residues from earlier fabrication steps, ensuring uniform etching across the chip. We then remove 180 - 190 nm SiO2 by placing the chip in a BOE solution of 1:7 49% HF:NH4F for 2 minutes and 30 seconds and the etching rate is calibrated on the dry SiO2 as approximately 75 nm/min. The chips are transferred to IPA to stop the etching process, and critical point drying is then used to prevent junction collapse during IPA evaporation.

Figure 3.6 shows titled SEM images of junctions at 80°, demonstrating that the junction is fully suspended over a length of 670 nm without collapsing. This suspension length depends on both the junction width and the etching depth. Junctions with narrower widths tend to be suspended more. Up to this step, we fabricate six suspended SWCNT-under-Au junctions on four different chips, ready for packaging into our custom-built QTS platform.

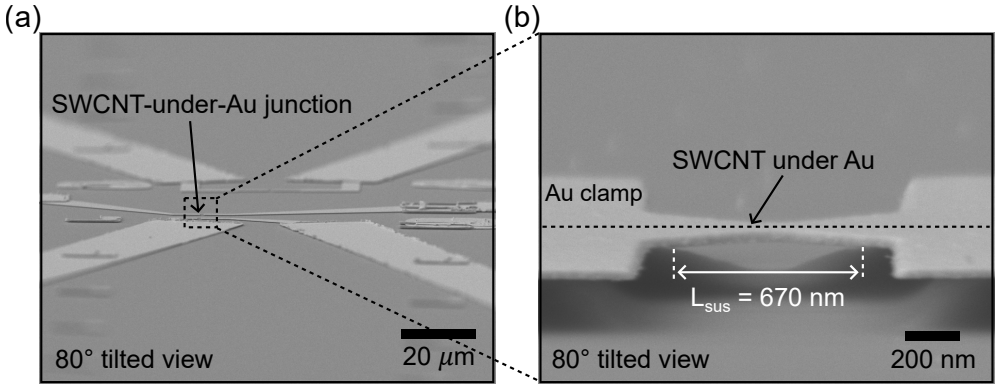

Figure 3.6: Suspended SWCNT-under-Au junctions. (a) A tilted-SEM image (80°) of the EBL pattern. (b) The zoom-in indicates that the junction is fully suspended over a length of 670 nm.

3.2 Packaging SWCNT devices for a custom-built QTS platform

In Chapter 2, we proposed an experimental platform for studying quantum transport in strained SWCNTs, as illustrated in Fig. 2.1(a). To implement this concept, we modified an existing low-temperature cryostat probe, focusing primarily on its wiring and mechanical assembly, which required non-trivial design and custom fabrication. Figure 3.7(a) shows our top-loading cryostat probe. At the top of the assembly is a stepper-motor unit (Fig. 3.7(b)), which connects to an internal driving rod shown in Fig. 3.7(c). This rod transmits motion down the cryostat to a driving fork (Fig. 3.7(d)), which in turn rotates the push screw (rigidly attached to the fork block shown in Fig. 3.7(e)) to apply mechanical strain to the sample. The BNC box in Fig. 3.7(b) is connected to the folded ribbon cables in Fig. 3.7(d), which link to the sample holder and ultimately to the SWCNT device, enabling electrical measurements. Further details of this electro-mechanical cryostat probe can be found in our previous work [49, 52].

In this section, we discuss how we package SWCNT devices for the cryostat probe designed for QTS measurements. This includes gating the substrate, wire-bonding contact pads, loading the chip, cooling down the cryostat, and building the electrical circuits. Be mindful that SWCNT devices are extremely fragile and could be easily destroyed by electrostatic discharge. Additionally, it is very challenging to bond a contact pad on the chip with a custom chip holder which is not planar (3D). Loading the chip and inserting the probe also requires patience and careful handling. To address these challenges, we improved the gating procedure and optimized the wire-bonder settings to achieve a higher yield, and refined the

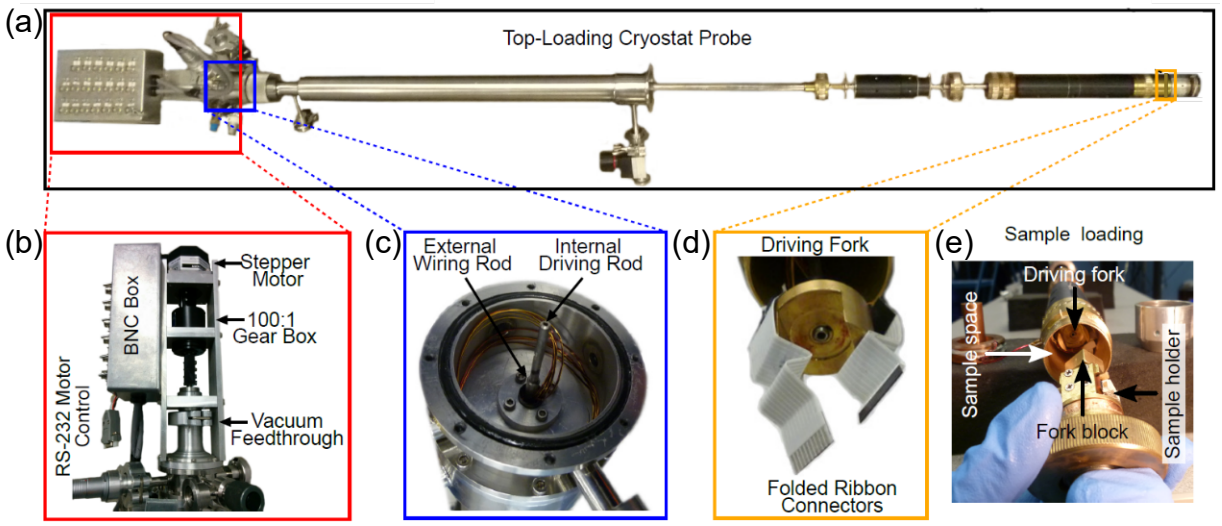

Figure 3.7: Custom-built cryostat probe for QTS. (a) Top-loading cryostat probe. (b) A stepper motor assembly. (c) The internal driving rod and external wiring rod are separated to prevent wire tangling during rod rotation. (d) Driving fork and folded ribbon connectors. (e) The sample is loaded into the probe. Figure adapted from [52].

loading process to make it both safer and more efficient. In the following, we present these procedures, emphasizing improvements made over previous work [49].

3.2.1 Gating and wire-bonding devices

To make transport measurements, a bias voltage is required to drive the current through the SWCNT device, and a gate voltage is needed to control the electrostatic potential in the channel. We gate the chip from the backside and wire-bond large contact pads on the front side.

Because all connector pins of the chip holder are on the top side and only the back of the chip is conductive (not covered by SiO_2), an aluminum wire is used to connect the gate voltage to the back from the front of the chip. Conductive epoxy is applied to secure the Al wire for both electrical contact and mechanical stability, as shown in Fig. 3.8(a). This gating process is done through a stereoscope. We first position the wire at the center of a six-pads pattern and then apply the epoxy, whereas previous work reversed this order. This modification reduces the amount of epoxy needed and minimizes its impact on the chip bending uniformity. The size of the epoxy on the front side is about 300 μm $\times$ 300 μm. We also made an improvement by placing the chip across a trench formed by two parallel glass slides during epoxy procedure. This provided greater stability and avoided the need for a

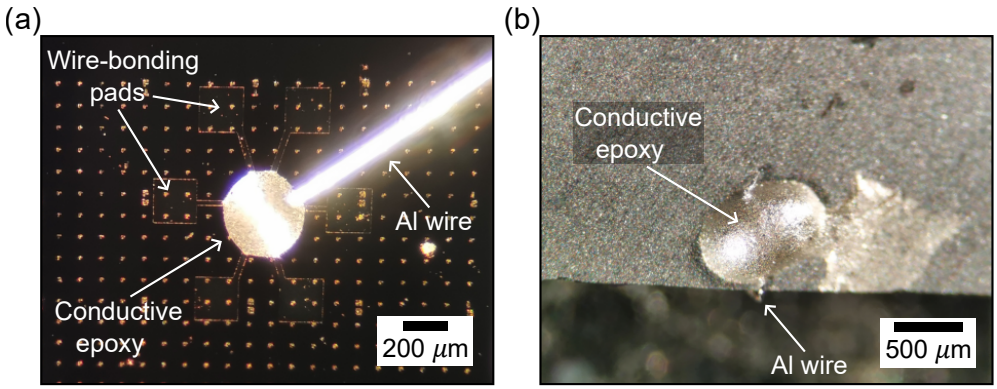

Figure 3.8: Back gating of a thin device substrate. (a) One end of the Al wire is epoxied at the center of the six contact pads using silver epoxy. (b) The other end of the Al wire is epoxied at the edge of the conductive backside of the chip, away from the center to avoid blocking the pushing screw.

large epoxy bumps on the front side for protection when flipping the chip, as in earlier work. This stability also allowed us to apply a smaller amount of epoxy on the backside, as shown in Fig. 3.8(b). After curing, both the electrical connection and mechanical strength of the wire were verified.

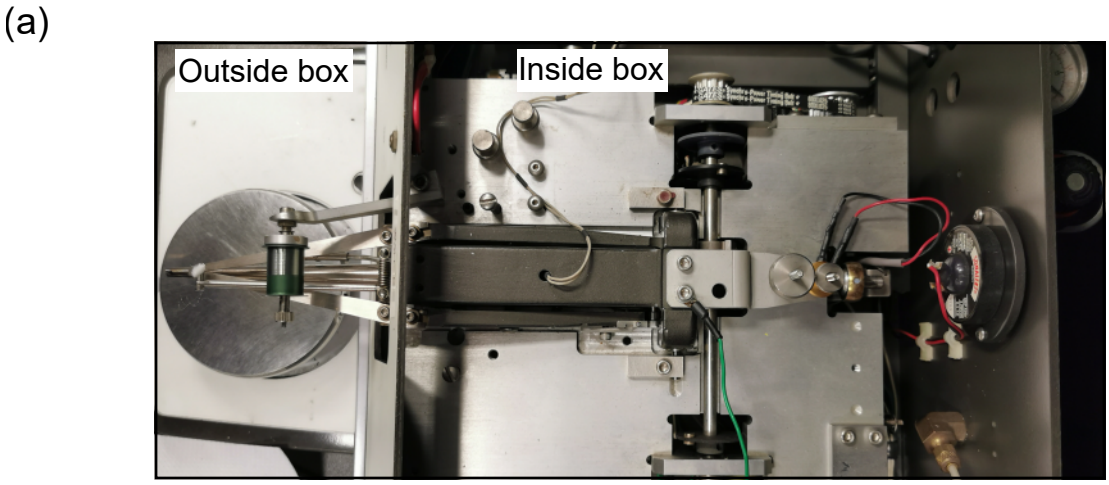

Figure 3.9: Top view of the wire-bonder. The left side shows the parts outside the instrument, and the right side shows the parts inside the instrument.

Following the gating of the chip, we used a wire-bonder to bond a wire between the connector pins on the chip holder and the large contact pads on the chip. The model used is a West·Bond MODEL 7400A SERIES, a manual wedge bonder. Although it takes time to become proficient with this machine, it allows us to perform wire-bonding that requires a

large bonding distance both along the chip surface and vertically. Besides practicing wire-bonding skills, such as planning the bonding paths to avoid wires touching each other (also improves the visual neatness), bonding at exact positions on the large contact pad without touching the SiO_2 surface, it is also essential to have the right settings so that the bonds are solid both on the large contact pads and the connector pins while not damaging the substrate, which could cause the gate leakage. We conduct a series of experiments to optimize bonding parameters, and here, for the first time, we present below detailed information on this wire bonder and describe how to adjust its settings to achieve the best bonding results for thin chips mounted on our QTS chip holder.

Figure 3.9 presents the top view of the wire bonder with its outer box opened. For clarity, we describe only the key components here. On the left side are the working stage, bonding tip, clamp blade, and wire spool, which are visible without opening the box. Inside are the feed screw, force screw, and tail screw. The working stage can be rotated to adjust its height, thereby raising or lowering the chip holder. We set the stage height to four and a half turns from the lowest position. Taping the stage helps keep it fixed during bonding. This height is determined by ensuring that the bonding tip contacts the pads at 90° for uniform bonding.

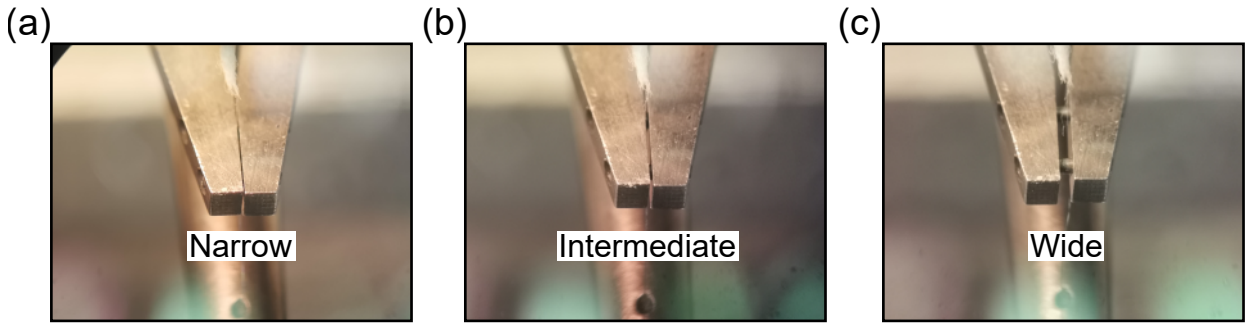

Figure 3.10: Clamp blade distance. (a)-(c) Narrow, intermediate and wide clamp blade distances.

The clamp blades, shown in Figure 3.10, must be set to an intermediate spacing. If too narrow, they block wire feeding, if too wide, they fail to hold the wire properly. The optimal clamping distance is about 0.0046 inch, adjusted by turning the feed screw (Figure 3.11(a)) by ten turns from its lowest position.

We use a UT45A-W-3535-3/4-CM bonding tip from Micro Point Pro (Fig. 3.11(d)), designed for 1.5 mil Al wire. We select this wire thickness because the bonding power required for a solid connection to the connector pins on the chip holder is sufficiently high that thinner wires would break easily, while thicker wires would make it difficult to position the bonds

on the contact pads without touching the SiO_2 surface. The tip and spool positions, shown in Fig. 3.11(e) and (f), are optimized to ensure smooth and continuous wire feeding during operation.

The force screw is used to adjust how firmly the tip is pushed against the substrate, if too strong, it breaks the Al wire, if too weak, it leads to a poor bonding. We set this to be 18 turns from its lowest position for the best result. Finally, the tail screw controls how long the wire is delivered through the bonding tip after each bond and the lowest position is sufficient.

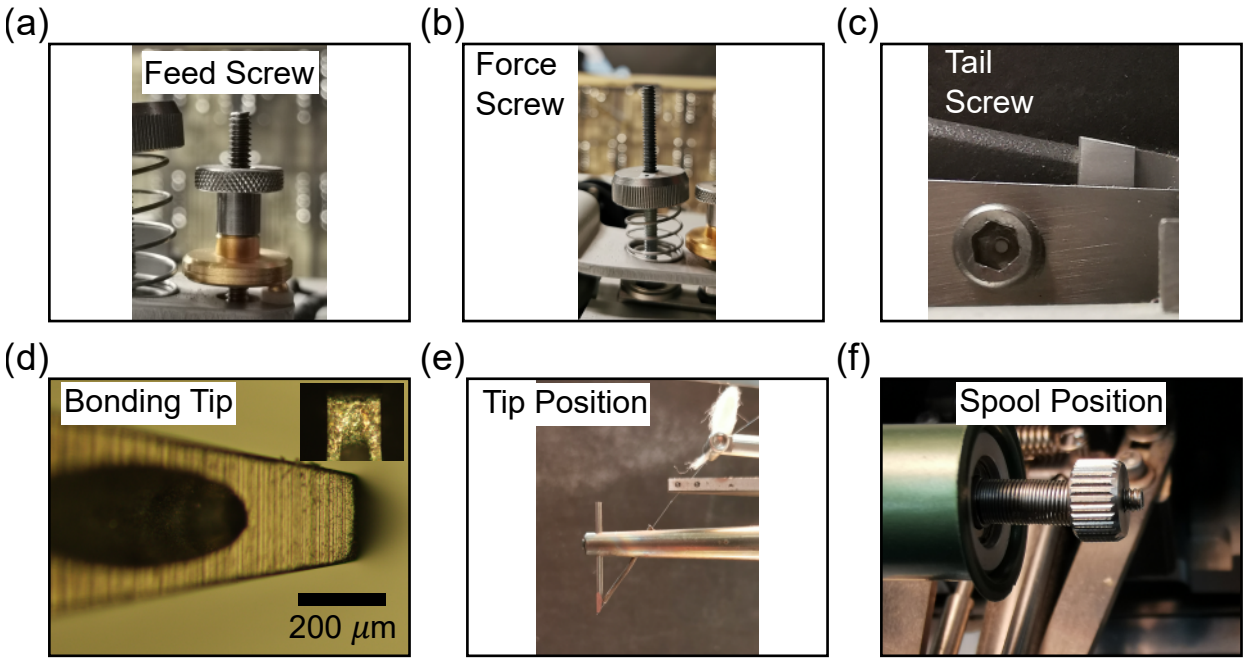

Figure 3.11: Selected wire-bonder settings. (a) The feed screw is used for adjusting the clamp blade distance. (b) The force screw is used for controlling the force pressed against the substrate. (c) The tail screw is used for adjusting the length of the wire delivered through the bonding tip after each bond. (d) The bonding tip UT45A-W-3535-3/4-CM from Micro Point Pro. (e)-(f) The tip and spool positions needed to be adjusted properly to ensure smooth wire-feeding.

Figure 3.12(a) shows the bonded wires connecting the large contact pads to the connector pins on the chip holder. We bond them symmetrically for a strong and uniform support for the chip. Panel (b) shows bonds under a microscope and we confirm their robustness by applying a pulling force. The bonds demonstrate excellent strength, providing confidence that they will remain secure throughout the rest of the experiment.

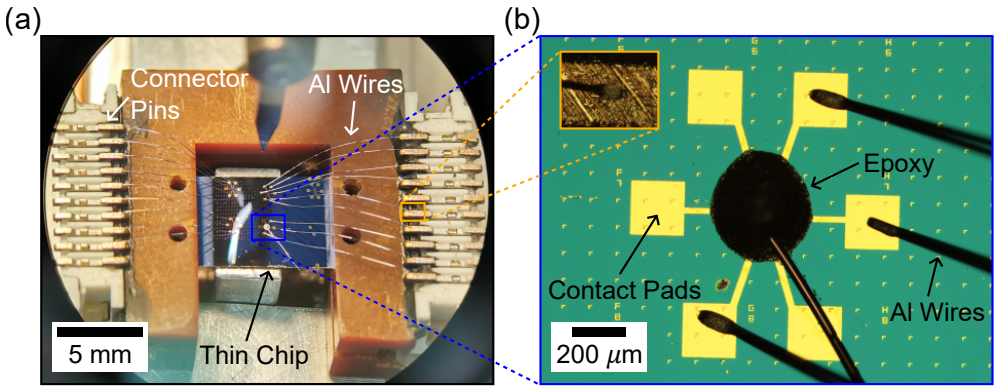

Figure 3.12: Wire-bonding images. (a) Al wires are bonded to the large contact pads on the chip and connector pins on the chip holder. (b) The zoom-in shows the bonds on the contact pads and connector pins.

3.2.2 Loading devices into the cryostat probe

After a chip was gated and wire-bonded, we loaded it into our custom-built cryostat probe, which is designed to provide both the necessary electrical connections and mechanical control of the push screw. A detailed description of the probe itself is available in earlier theses and publications [49, 52]. Here, we focus specifically on the modifications we introduced to improve the chip-loading procedure.

The chip holder is first flipped over and inserted into the manifold, as shown in Fig. 3.13(a), which holds the chip holder in position and allows the movement of the push screw. This assembly was then secured on a mechanical vise and grounded using grounding strips to protect the samples from electrostatic discharge. The folded flexible cables connected to the electrical circuits inside the cryostat probe were clamped in a position aligned with the chip holder connectors, as shown in Fig. 3.13(b). The driving fork, used for turning the push screw, was rotated to align with the block holding the push screw. We then moved the assembly toward the cryostat probe, inserted the flexible cables into the connectors, and locked them into place. This is illustrated in Fig. 3.13(c). Finally, we secured the assembly with a retaining nut and inserted the temperature sensor block for sample-space temperature control. In this process, we introduced the use of the vise and clamps, which were not part of the previous methodology. This addition significantly simplified the procedure and increased the device safety. In the earlier approach, connecting the folded cables and inserting the assembly into the probe often required the assistance of two people, or a single person working with significant effort and time. We repeatedly used this method with consistent success, making the loading process more manageable and no longer a high risk part of the

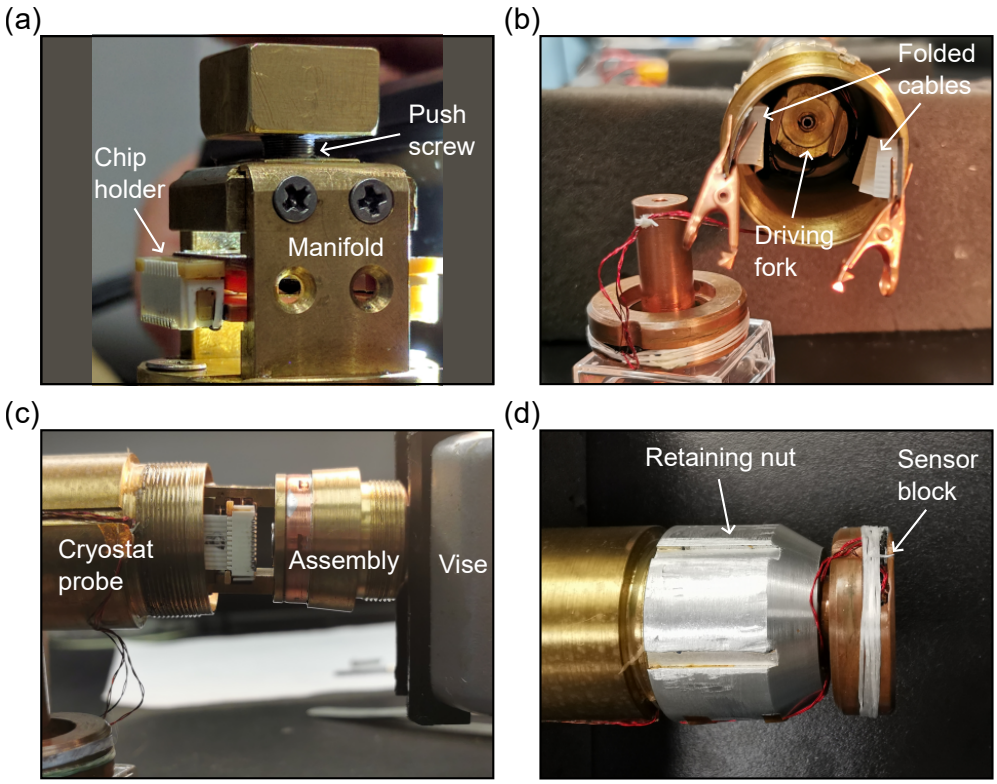

Figure 3.13: Loading a chip with devices. (a) The chip holder with a wire-bonded Si chip is flipped over and then inserted into the manifold. The push screw is used to bend the Si chip. (b) Folded flexible cables are held in position with a pair of clippers. (c) By adjusting the position and orientation of the manifold with a mechanical vise, the folded flexible cables can be inserted and locked into the connectors on the chip holder. (d) The probe is sealed to prevent vacuum leaks.

experiment.

At this stage, we have packaged and loaded our SWCNT devices into the QTS probe. They are now secured by grounding all connector pins, and the probe effectively acts as a Faraday cage to protect the sample space from electrostatic effects.

3.3 Creating ultra-short SWCNT quantum dot devices

At this stage, the SWCNTs remain covered by a Au film and we still needed to break the film to create naked nanotube channels. For a given substrate bending, shorter channel lengths provide a larger mechanical strain range. Our goal is to reach as much strain as possible to observe pronounced strain-induced transport features. However, if the channel is too narrow, the gate coupling becomes weak and the transport data becomes less informative. The channel length depends on the thickness and width of the Au junction, as well as on

the breaking voltage and power. We successfully fabricate three strain-tunable SWCNT quantum-dot (QD) devices, one with strong gate dependence and two with record-high tunable mechanical-strain ranges. In this section, we describe the electromigration and Joule-annealing processes used to expose and clean the SWCNT channel.

3.3.1 Fabricating nanoscale SWCNT channels via electromigration

Figure 3.14(a) illustrates the working principle of electromigration. When a large current flows through the suspended junction, gold atoms loosen as the temperature increases due to Joule heating. The flowing electrons momentum transfer can then knock away Au atoms, creating a gap that exposes the SWCNT beneath the Au. This method opens a nanoscale gap in the Au, resulting in a very short SWCNT channel.

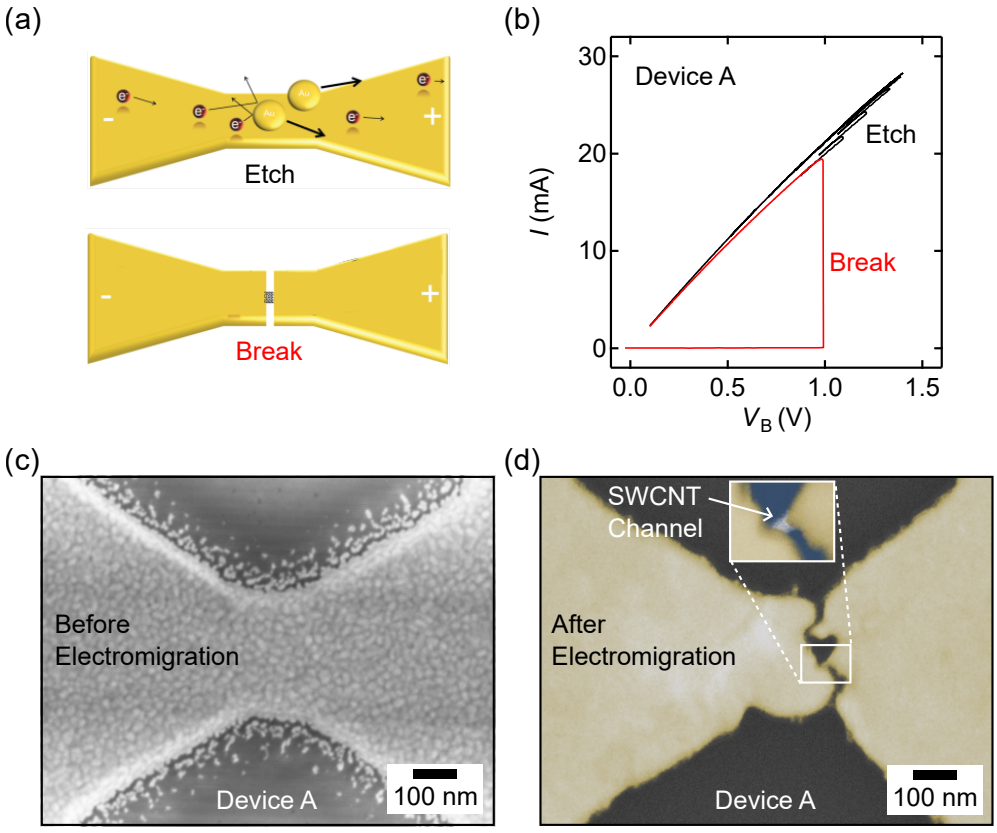

Figure 3.14: Fabricating a nanoscale SWCNT channel via electromigration. (a) Cartoon showing how electromigration works to break the Au film. Figure adapted from Ref. [49]. (b) The black and red curve shows the etching and breaking stages during electromigration of Device A. (c)–(d) SEM images of Device A before and after electromigration. A $\approx$ 30 nm SWCNT channel is exposed.

Both the voltage and power used to break the Au film influence the resulting channel length. However, their dependence is not straightforward, and these two parameters are not independent. Furthermore, the maximum achievable voltage and power during electromigration vary from device to device, depending on geometry and micro-defects. We employ a feedback system [49] to have coarse control over the breaking voltage and power. The optimum breaking power for our devices is approximately 35 mW, with a bias voltage greater than 1 V, for Au junctions 270 nm wide and 50 nm thick.

Figure 3.14(b) shows the etching and breaking stages of electromigration. The black curve indicates the gradual removal of Au atoms, which narrows the junction and corresponds to the etching process. The junction typically breaks at slightly higher voltage and power than the final values reached during etching. The red curve represents the breaking process, during which the resistance increases sharply at $V \approx 1$ V. Panels (c) and (d) show the Au junction before and after electromigration, respectively. A 30 nm SWCNT channel was created for subsequent transport measurements.

3.3.2 Joule annealing of SWCNT QDs

During photolithography and e-beam lithography, some resist residue inevitably remains and may contaminate the SWCNT. Joule annealing is a common method used to clean the suspended SWCNT channel by passing a large current through it to thermally anneal the residue. We need to be careful not to over-anneal the device, as excessive heating can introduce unwanted structural defects in the SWCNT channel. Another effect of annealing is tuning the doping of the SWCNT contact sections (source and drain), as annealing removes oxygen from gold, which modifies the Au work function [66, 94] and how much charge it transfer to the underneath nanotube. This process can potentially convert a closed-QD device into an open-QD device [63]. At this stage, we completed fabrication of SWCNT-QD and graphene transistors for transport measurements under tunable mechanical strain.

3.4 Conclusions

In this chapter, we have shown how we located and identified SWCNTs using SEM and AFM, and how we build suspended SWCNT-under-Au junctions using EBL and BOE. Suspended junctions on thin Si chips allow large and tunable mechanical strain upon substrate bending, permit electromigration and annealing, as well as eliminate disorder originating from the substrate. We have also discussed how we wire-bonded SWCNT devices and packaged them

for our QTS platform, which enables quantum-transport measurements and mechanical-strain control of SWCNT devices. Lastly, we have presented methods to expose and clean nanometer-scale SWCNT channels using electromigration and Joule annealing. The suspended Au clamps will act as cantilever arms that amplify the applied mechanical strain to the short SWCNT channels to help maximize the strain range and observe effects from strain-induced potential in charge transport.

Our experimental methods provide a path to study the mechanical control of quantum transport in low-dimensional materials. It is also straightforward to modify the device geometry to explore a wide range of physical effects in different materials in the future. For example, by depositing three Au clamps at 120° spaced orientations on a graphene sheet, we could study large, tunable pseudo-magnetic fields arising from triaxial strain. By stretching magic-angle twisted bilayer graphene instead of monolayer graphene, we could mechanically tune the superconducting phase.

In the next chapter, we will discuss our latest transport measurements in strain-tunable SWCNT quantum dots fabricated using the experimental methods introduced in this chapter.

Chapter 4

Experimental Straintronics in SWCNT Quantum Dots

Single-wall carbon nanotubes (SWCNTs) are narrow ribbons of graphene with atomically precise edges and a single quantum transport channel, at realistic dopings. This makes them ideal systems to harness *quantum transport straintronics* (QTS), i.e. using mechanical strain to control accurately quantum transport. We present QTS data from three single-wall carbon nanotube quantum dot (SWCNT-QD) transistors over a broad range of *in-situ* tunable and reversible uniaxial strain ($\Delta\varepsilon_{\rm mech} \approx 0$ to 4 %). We first present the nanofabrication of the suspended SWCNT transistors whose channel lengths are ≈ 30 nm. The channels are strained by moving gold clamps holding the nanotubes. We present detailed charge transport data, $dI/dV_{\rm B} - V_{\rm B} - V_{\rm G}$ and $dI/dV_{\rm B} - V_{\rm B} - \Delta\varepsilon_{\rm mech}$, showing a large mechanical-gating effect of the SWCNT-QDs. The precise reversibility of the data, and their agreement with QTS theory, confirms that the tubes are strained elastically. By analyzing the data with QTS theory, we demonstrate that the mechanical control of the QD doping is not due to capacitive-gating effects, but to *predictable* bandstructure changes described by scalar and vector potentials. This added mechanical degree to control SWCNT-QD doping could find applications in qubits and other quantum devices.

4.1 Introduction

Experimental control of quantum transport, and its quantitative agreement with theory, in one- and two-dimensional materials (1DMs/2DMs) requires very low and uniform disorder across entire devices [1,2]. This level of mastery has been achieved for charge dopant disorder [3], but not for mechanical (strain) disorder in most 2DMs and their nanotubes/nanoribbons [4]. Quantum straintronics transport (QTS) aims to both remove the disruptive effects

of disordered (uncontrolled) strain fields on quantum transport, as well as using precisely engineered strain fields in 2DMs and 1DMs to tune their properties (band gap, charge doping, gauge potentials) towards quantum electronics applications [20, 33, 35, 36, 51–53, 95]. Ideal quantum straintronics transistors would permit a complete control of both the magnitude and phase of their quantum current both mechanically and electrostatically. This would lead to many possibilities to optimize quantum effects in graphene, transition metal dichalcogenides (TMDs), twisted 2DMs, and 1D nanotubes/nanoribbons [42, 54–57]. Technological applications of QTS would include qubits and quantum circuits [5–10], spintronics [11–16], valleytronics [17–20], strain-tunable superconductivity [21–23] and topological switches [21, 24–29].

There have been a few recent demonstrations of well-controlled QTS in graphene transistors [43, 52]. However, the experimental validation of many exciting QTS theoretical predictions [21, 35] has been a major challenge. Two major experimental limitations to explore *quantitative* QTS are that 2DM devices usually have atomically disordered edges which scramble the phase of their charge carriers, and the mesoscopic widths of most 2DM devices mean that many subbands (transverse momentum modes) contribute to their charge transport. Because the quantum phase of each mode is impacted differently by mechanical strain [36, 51], many subbands make a precise control of QTS complex. Single-wall carbon nanotubes (SWCNTs) and other nanotubes [54, 60] naturally resolve both of these issues as they have perfect transverse (periodic) boundary conditions, and their very narrow width (circumference) leads to a single transport subband being available at experimentally relevant charge dopings. Until now, only the most basic room-temperature strain-dependent properties of SWCNTs, such as bandgaps, have been studied experimentally [42, 61]. Thus, SWCNTs represent a major unexplored opportunity for QTS experiments. For instance, recent theoretical work [38] foresees that transistors made with a SWCNT will permit a full *mechanical* control of the quantum phase of their coherent charge current. Previous work on SWCNTs also suggests a broad strain tunability of their electron-phonon coupling [62] and spin-orbit coupling [16].

In addition to being a rolled-up 2DM, SWCNTs are also single-molecules which can naturally host quantum dots acting as zero-dimensional (0D) systems. The long length of nanotubes allows a precise alignment of the tubes, and permits to use the same tube for the contacts (source/ drain) and channel of the device. This enables highly reproducible fabrication of QDs which nearly match the size and energy scales of traditional single-molecule transistors [96]. It is expected that straining a firmly clamped SWCNT-QD can be used to

mechanically control the charge state [38] of the QD. This approach would permit to tune the doping single-molecule transistors even when they are electrostatically shielded by metallic contacts [37].

In the following sections, we report QTS data from three SWCNT-QD transistors over a broad range of *in-situ* tunable and reversible uniaxial strain ($\Delta\varepsilon_{\rm mech} \approx 0$ to 4 %). We first present the nanofabrication of the devices, whose channels are strained by moving gold clamps holding the nanotubes. We discuss detailed transport data showing that the charge states of the QDs are tunable via strain. The data are fully reversible and reproducible. We then analyze and model the data with QTS theory [38], and find that the mechanical-gating effect stems from well-controlled bandstructure changes described by scalar and vector potentials.

4.2 Instrumentation and SWCNT transistors for QTS

4.2.1 Main results

Figure 4.1 and 4.2 presents the instrumentation and suspended SWCNT transistors we designed and fabricated to study QTS in SWCNTs. The geometry of our platform is shown in Fig. 4.1. The details of our instrumentation were reported previously [52]. In summary, it operates inside a low-temperature cryostat to precisely bend a Si substrate (thickness $t = 200$ μm) and applies a uniaxial mechanical strain $\Delta\varepsilon_{\rm mech}$ to our suspended SWCNT channels of length $L \approx 30$ nm, and diameter $d \approx 2$ nm. The nanotubes are held mechanically by gold clamps (50 nm-thick films). We have shown previously, in similar suspended SWCNT transistors (without tunable strain) [63], that the source and drain electrodes for the charge carriers are sections of the same nanotube located under the gold clamps. This creates a complete source-channel-drain transistor from a single SWCNT. The source and drain contacts have a charge doping set via charge transfer from the gold film [63, 66, 94]. The overlap length between the gold clamps and each nanotube contact is a few μm-long and provides slippage-free clamping, as we will demonstrate below. Details about the micro and nanofabrication of the SWCNT devices can be found in Sec. 4.2.2.

We study DC transport in these transistors at temperature $T = 4$ Kelvin. We apply a bias voltage, $V_{\rm B}$, to the source electrodes and measure the current, I, at the drain. The channel's Fermi energy (doping) is controlled via a gate voltage, $V_{\rm G}$, applied to the Si backplane. A unique feature of our device design is that the gold clamps are also suspended. These clamps act as cantilever arms which amplify the mechanical strain imparted to the SWCNT channel

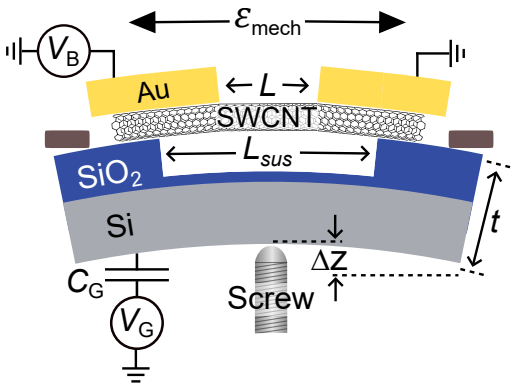

Figure 4.1: Instrumentation for quantum transport straintronics (QTS). Side-view schematic of the instrumentation loaded in a low-temperature cryostat. A push screw bends slightly the ultra-thin Si substrate, applying an *in-situ* mechanical strain $\varepsilon_{\rm mech}$ to the suspended SWCNT channel. A DC circuit is used for transport measurements.

upon bending the substrate. The total suspension length of our transistors is $L_{\rm sus} \approx 700$ nm (Fig. 4.1). The strain applied to the channel is given by $\varepsilon_{\rm mech} = \Delta x/L = (3L_{\rm sus}t/D^2)\Delta z/L$, where Δx is the uniaxial stretching of the tube, $D \approx 8.2$ mm is the distance between the substrate anchoring points, and Δz is the motion of the pushing screw bending the substrate. Over a large number of previous experiments, we found that a maximum $\Delta z_{\rm break} \approx 260$ μm can be applied before substrate failure [52]. In the present experiment, we applied up to $\Delta z_{\rm break} = 130$ μm and reached a maximum $\varepsilon_{\rm mech}$ of 4% in Device B which had a 26-nm-long channel and $L_{\rm sus} \approx 890$ nm. It is worth mentioning that any gate-voltage induced strain is truly negligible due to the very short length of our channels [36].

Figure 4.2(a) shows a tilted (80°) scanning electron microscopy (SEM) image of Device A1 before we used electromigration to create the naked SWCNT channel. The SWCNT, under the gold film, is outlined with a dashed line. The measured $L_{\rm sus}$ is 650 ± 45 nm. SEM images of the other two samples, Devices A2 and B, are shown in Sec. 4.2.2 and give $L_{\rm sus} =$ 580 ± 55 nm and 890 ± 25 nm, respectively. The final step of sample fabrication is a low-temperature feedback-controlled electromigration [63,85], which we used to create a nanogap in the suspended gold film. Figure 4.2(b) shows Device A1 after the electromigration step. The top-left inset is a summary of the I - $V_{\rm B}$ electromigration data, where a relatively large current is used to create a Joule-induced electromigration of the gold. The electromigration power for Device A1 was $P = 34$ mW. In the main panel, and the top right inset, of Fig.4.2(b), we see the gap formed in the gold film and the SWCNT channel ($\approx$ 28 nm) bridging the

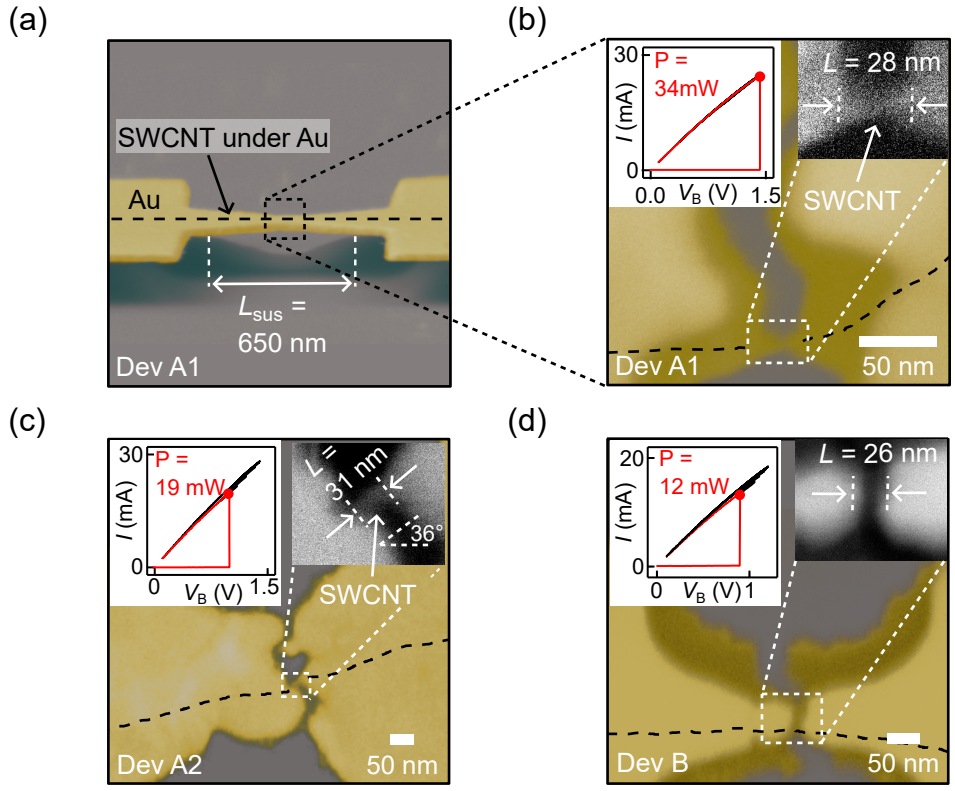

Figure 4.2: SWCNT transistors for quantum transport straintronics (QTS). (a) Tilted-SEM image (80°) of the suspended SWCNT-under-gold breakjunction in Device A1 (before electromigration). The suspension length is $L_{sus} = 650$ nm. (b) Zoom-in view of the breakjunction in (a) after electromigration. The top left inset shows the electromigration process for Device A1, and the top right inset the small scale SEM image of the naked-SWCNT channel created during this process. (c)-(d) show the same information as (b) for Devices A2 and B, respectively.

gap. The position of the nanotube beneath the gold film (dashed lines), was determined precisely by aligning SEM images of the SWCNT before the gold deposition and after the electromigration (Sec. 4.2.2).

Figures 4.2(c)-(d) show the electromigration step and SEM images for Devices A2 and B, respectively. Devices A1 and A2 were fabricated on the same SWCNT at different locations. This is important since it guarantees that these two devices have the same nanotube chirality (rolling angle) and diameter. As shown in Sec. 4.2.2, the measured tube diameters for the devices are 2.1 ± 0.5 nm (Devices A1-A2) and 1.6 ± 0.4 nm (Device B).

Following electromigration, and before making the transport measurements, we used Joule-annealing (Sec. 4.2.2) to remove leftover nanofabrication residues, acting as scattering centers, on the SWCNT channels. Figure 4.3(a) shows transport data $I - V_B$ in all three

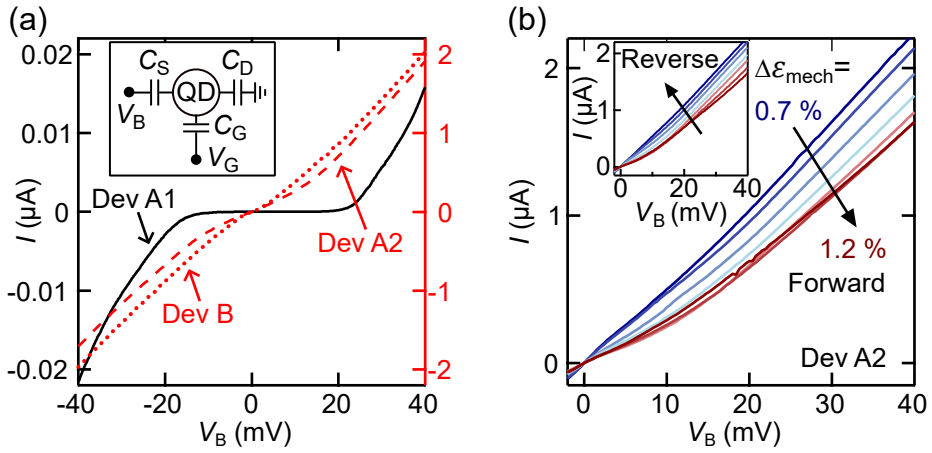

Figure 4.3: I-V_B transport data and hysteresis-free reversibility for SWCNT-QDs. (a) I-V_B data at 4 Kelvin, after electromigration, in Devices A1 (black, solid), A2 (red, dashed), and B (red, dotted). The inset is a schematic of our QDs' electronics circuit. (b) I-V_B data in Device A2 versus increasing $\Delta\varepsilon_{mech}$. The inset shows the reverse mechanical sweep data, demonstrating hysteresis-free reversibility.

devices at V_G and $\Delta\varepsilon_{mech} = 0$. The resistance of Devices A2 and B are ≈ 20 kΩ, consistent with open QD behavior [63, 82, 83] (i.e. semi-transparent contact-channel tunnel barriers). On the other hand, Device A1 is a closed QD and shows a clear Coulomb blockade regions [48] (opaque tunnel barriers). The inset of Figure 4.3(a) shows a lump-element electronics diagram for our QD devices. The electrostatic potential on the dot [97] is set via the source, drain and gate capacitance, respectively labelled C_S, C_D, C_G.

Figure 4.3(b) shows the $I - V_B$ transport data for Device A2 at various applied strain $\Delta\varepsilon_{mech}$. We notice a very smooth decrease in the conductance of the device as a function of increasing strain. The inset shows that the data from a reverse mechanical sweep (decreasing strain) precisely reproduces the forward data. This is true for all three devices, and the relevant data for Device A1 and B are shown in Sec. 4.2.2. This reproducibility is achieved over numerous forward and reverse mechanical sweeps. This is very strong evidence that the SWCNT channels are stretched elastically without any slippage of the tubes under the gold clamps. In the remainder of this work, we measure and calculate how mechanical strain predictably modulates quantum transport in these three SWCNT-QDs.

4.2.2 Supporting material

In this section, we summarize key parameters of the SWCNT devices shown in Fig. 4.2, and describe critical fabrication steps including nanotube diameter measurements, Au clamp

alignment, and junction suspension. We then describe the annealing process used to clean the SWCNTs, with all measurements in this section being carried out after the final anneal. Lastly, we present the mechanical calibration and additional data confirming reproducible and reliable mechanical motion using the instrumentation shown in Fig. 4.1.

Device	d (nm)	L_{channel} (nm)	L_{sus} (nm)	C_G/C_S	$C_G/(C_D+C_G)$
A1	2.1 ± 0.5	28 ± 5	650 ± 45	9.50E-02	8.50E-02
A2	2.1 ± 0.5	31 ± 5	580 ± 55	7.45E-05	4.85E-05
B	1.6 ± 0.4	26 ± 5	890 ± 25	2.07E-04	1.82E-04

Table 4.1: Key parameters of SWCNT devices. Devices A1 and A2 share the same SWCNT (Fig. 4.5). Channel lengths are ≈ 30 nm and suspension lengths are 600 to 900 nm. Lower capacitance ratios in A2 and B reflect weaker gate dependence than in A1.

We list the key parameters for all SWCNT devices in Table 4.1. Devices A1 and A2 originate from the same SWCNT, as shown in Fig. 4.5. The diameter uncertainty is estimated by averaging multiple AFM height profiles measured at different positions along the nanotube. The channel length, obtained from SEM images, is about 30 nm for all devices. The suspension length L_{sus} varies between 600 and 900 nm (Fig. 4.2 and Fig. 4.6), mainly due to variations in the bow-tie junction width. Capacitance ratios C_G/C_S and $C_G/(C_D+C_G)$ are extracted from the slopes of Coulomb diamonds in the dI/dV–V_G–V_B maps (Sec. 4.3.2). Devices A2 and B show significantly smaller capacitance ratios than Device A1, consistent with their weaker electrostatic gate coupling.

We measured SWCNT diameters using AFM (atomic force microscopy). Figure 4.4(a) shows the height measurement over a 1 μm × 1 μm area, where black, red, blue, gold, green, and purple dotted lines indicate the scan positions corresponding to the data in (b). To minimize the effect of substrate tilt, we averaged all data points (red curve) and fitted the regions away from the nanotube center to extract the background. After removing the background tilt, the nanotube diameter was obtained by measuring the height difference between the nanotube and the substrate. The nanotube for Devices A1 and A2 has a diameter of 2.1 ± 0.5 nm, while the one for Device B has a diameter of 1.6 ± 0.4 nm. The uncertainty includes contributions from statistical variations and systematic effects associated with the AFM measurement [92, 93]. The SWCNT diameter was used to confirm that the nanotube is single-walled [81] and to calculate the maximum gate capacitance using a wire-to-plane model, assuming minor screening effect from the Au film (Sec. 4.3.2).

Here, we provide additional details on the alignment and suspension of the Au clamps to build suspended SWCNT quantum dots. Figure 4.5(a) shows the Au clamps deposited

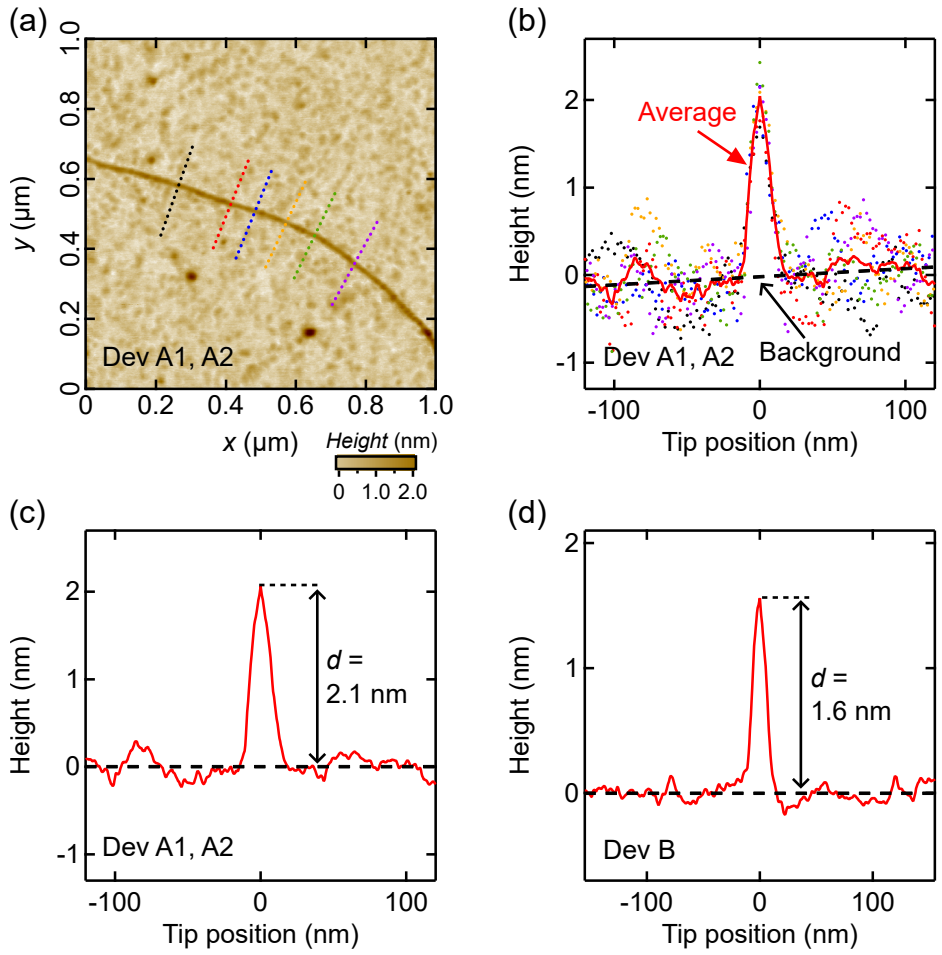

Figure 4.4: Measurement of SWCNT diameters. (a) 1 μm $\times$ 1 μm AFM image of the SWCNTs for Devices A1 and A2. (b) Dots with different colors indicate data from different scans across the nanotube in (a). The red curve is the average of all data points, and the black dashed line is the linear fit of the substrate background. (c),(d) After removing the background tilt, the nanotube diameters were determined to be 2.1 $\pm$ 0.5 and 1.6 $\pm$ 0.4 nm for Devices A1/A2 and B, respectively.

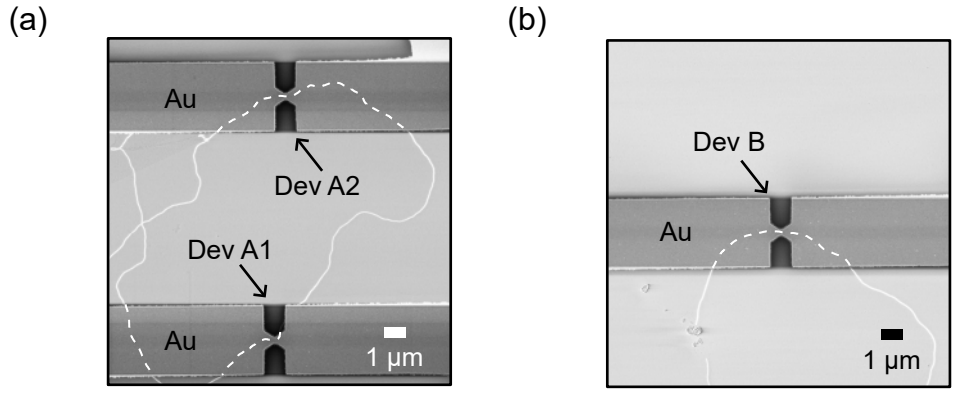

Figure 4.5: Clamping SWCNT channels with Au films. (a) Au clamps are aligned and deposited on the selected horizontal SWCNT sections of Devices A1 and A2. Dashed lines are drawn based on the superposition of SEM images of the SWCNT before and after Au clamp deposition. (b) Au clamps on top of the SWCNT section for Device B.

on the selected SWCNT sections for Devices A1 and A2. The nanotube direction is aligned with the chip bending direction (horizontal). The white dashed lines indicate the nanotube positions beneath the Au film, obtained by superimposing SEM images taken before and after Au deposition. The Au clamps for Device B are shown in Fig. 4.5(b). After etching of the substrate's oxide, the junctions were left suspended as shown in Fig. 4.6(c) and (d) for Devices A2 and B, respectively. Device A2 has a suspension length of 580 nm, whereas Device B has a suspension length of 890 nm, which explains the larger mechanical strain range of Device B.

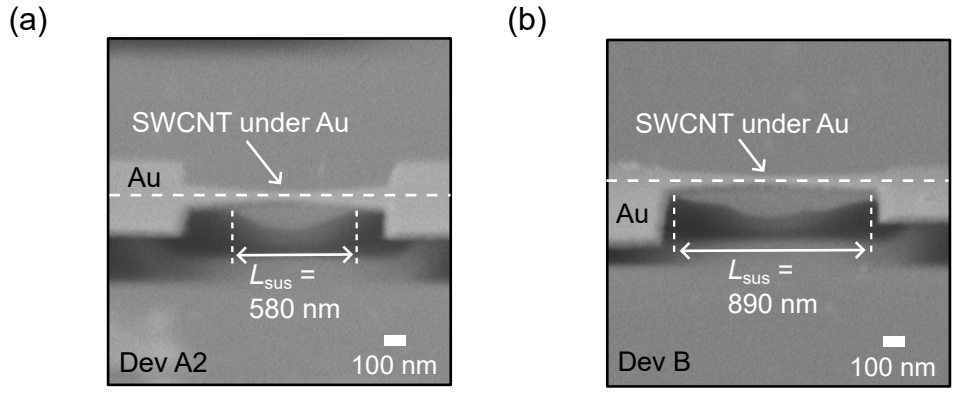

Figure 4.6: Suspending SWCNT-under-Au junctions. (a),(b) Suspended SWCNT-under-Au junctions for Devices A2 and B imaged at an 80° tilted angle, respectively.

After fabricating the suspended SWCNT-under-Au junctions, we loaded the devices into

the cryostat and cooled them down to 4 K. The SWCNT channels were then created via electromigration, as shown in Fig. 4.2. However, resist residues from earlier fabrication steps can remain on the SWCNTs, degrading transport measurements. To solve this problem, we passed a large current through the SWCNTs, generating sufficient heat to anneal contaminants and prepare the devices for transport measurements. This process is referred to as Joule annealing. Figures 4.7(a)–(c) show the initial and final annealing processes for Devices A1, A2, and B, respectively. Although the initial annealing power is comparable across all devices, the final annealing power for Devices A2 and B is at least an order of magnitude higher than that for Device A1.

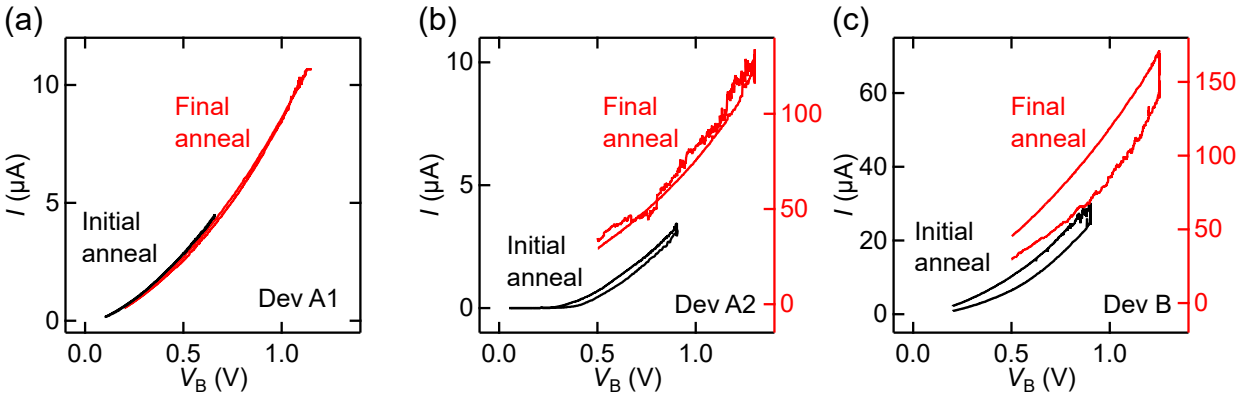

Figure 4.7: Joule annealing on SWCNT devices. (a)–(c) Annealing curves for Devices A1, A2, and B. Devices A2 and B show a strong current increase from the initial anneal to final anneal, from which the data presented in this chapter are extracted.

This large difference in annealing power resulted in distinct I–V_B behaviors after the initial (black) and final (red) anneals, as shown in Figs. 4.8. While Device A1 remained a closed quantum dot (high resistance and a clear blockade region), Devices A2 and B evolved from closed to open quantum dots (high conductance and weak blockade). Annealing is known to reduce the oxygen content of Au films and modify their work function [66, 94]. It thereby alters the doping level of the SWCNTs beneath the Au. In Sec. 4.2.1, we showed that the SWCNT channels in our devices are n-doped (electron-dominated). For low-power annealing (Device A1), the SWCNT contacts remain p-doped, forming thick tunnel barriers between the channel and contacts, resulting in a closed quantum dot. For high-power annealing (Devices A2 and B), the contact regions convert from p-type to n-type, producing weak tunnel barriers and open quantum dots. This behavior is consistent with previous observations of p-doped graphene contacts converting to n-type after annealing [52] and with the known electron–hole asymmetry we reported earlier in SWCNT devices [63].

After annealing, the zero-position of mechanical strain was calibrated by locating the

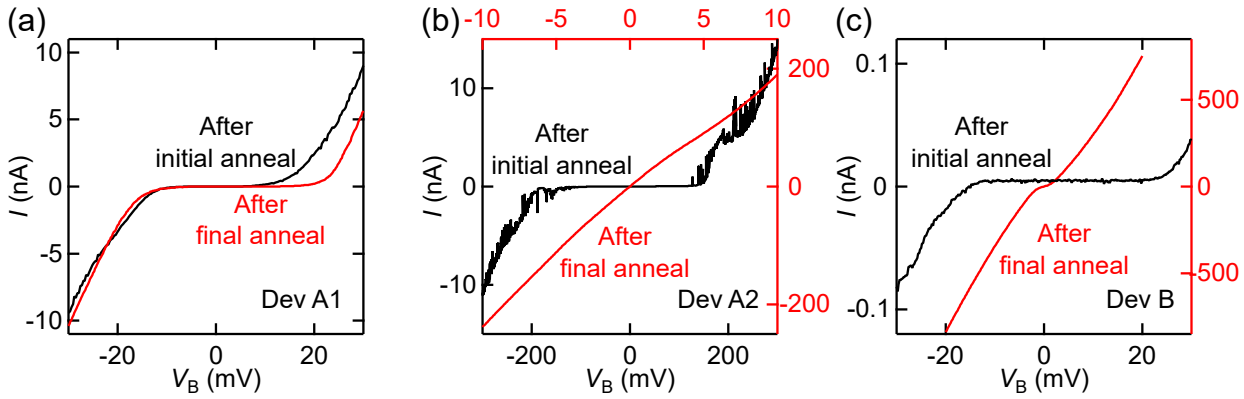

Figure 4.8: Annealing results for SWCNT devices. (a)–(c) Black and red curves are bias sweeps after the initial and final anneal, respectively, for Devices A1, A2, and B. Devices A2 and B become highly conductive with no visible blockade, indicating open quantum dots, while Device A1 remains a closed quantum dot, consistent with their anneal curves.

point where the SWCNT begins to stretch. The vertical displacement at the chip center is denoted by Δz, as shown in Fig. 4.1. When the chip is slightly bent, the nanotube may remain slack if it was not fabricated under tension, and can nevertheless cause minor resistance changes as the tube moves. The displacement at which this first resistance change appears is the same to all devices and defines the chip's zero position ($\Delta z = 0$). However, each device has its own zero-strain point ($\Delta\varepsilon_{\text{mech}} = 0\%$), determined by fitting the resistance versus Δz in the regions of high and low resistance changes on Fig. 4.9(a). The intersection of these fits defines the onset of $\Delta\varepsilon_{\text{mech}} = 0$. Figure 4.9(a) shows how we determine the zero point for Device A1.

Once we have the zero-strain point for Device A1, we can then calculate the applied mechanical strain using its geometry [73], $\Delta\varepsilon_{\text{mech}} = \Delta x/L_{\text{channel}} = 3L_{\text{sus}}t/D^2\Delta z/L_{\text{channel}}$, where L_{sus} is the suspension length, t is the chip thickness and D is the distance between two clamps for the chip (brown rectangles in Fig. 4.1). Figure 4.9(b) shows the I–V_{B} curves for Device A1 at $\Delta\varepsilon_{\text{mech}} = 0\%$–$2.1\%$, and the inset presents the data during the reverse mechanical sweep. The forward and reverse sweeps exhibit identical behavior. Similarly reproducible results for Devices A2 and B are shown in Fig. 4.3(a) and Fig. 4.9(c), confirming the reliability of the mechanical clamping.

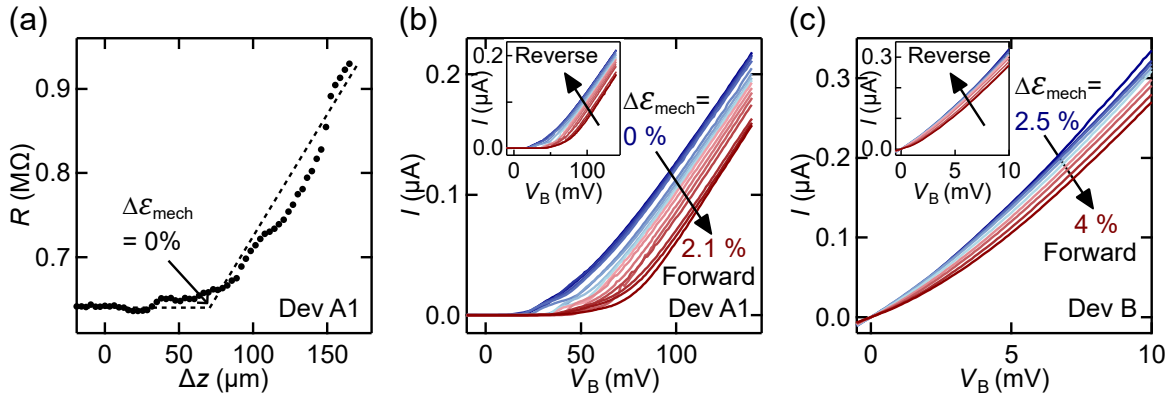

Figure 4.9: Mechanical calibration and reproducibility. (a) Resistance of Device A1 at $V_{\mathrm{B}} = 135$ mV and $V_{\mathrm{G}} = 5$ V as a function of Δz. The intersection of high- and low-sensitivity fits defines the zero position. (b) I–V_{B} characteristics for Device A1 as $\Delta\varepsilon_{\mathrm{mech}}$ varies from 0% to 2.1%. Forward (main) and reverse (inset) sweeps show nearly identical behavior, confirming reproducibility. (c) Forward and reverse sweeps in Device B are also highly reproducible.

4.3 Mechanical doping and workfunction tuning of SWCNT-QDs

4.3.1 Main results

Figure 4.10 summarizes the electro-mechanical transport data measured in Device A1, and additional data for this device are in Sec. 4.3.2. Figure 4.10(a) shows $dI/dV_{\mathrm{B}} - V_{\mathrm{B}-V_{\mathrm{G}}}$ data at $\Delta\varepsilon_{\mathrm{mech}} = 0$. The methodology to determine the location of $\Delta\varepsilon_{\mathrm{mech}} = 0$ is presented in Sec. 4.3.2. The data show a clear series of Coulomb diamonds (dashed contours labelled $N = 1$, 2, 3, 4). They correspond to QD charge ground states where one electron is added to the QD as we move from one diamond to its neighbor on the right. We remark that the width and slopes of the diamonds give direct measurements of the capacitances C_S, C_D, and C_G [63]. The width of the diamonds 1-3 are ≈ 0.56 V, giving $C_{\mathrm{G}} = 0.29$ aF. Using a wire-over-plane electrostatic model for C_{G}, the extracted channel length is $L_{\mathrm{G}} = 31$ nm. This is in good agreement with $L = 28nm$ obtained from Fig. 4.2(c).

Figure 4.10(b) shows a similar data set acquired at $\Delta\varepsilon_{\mathrm{mech}} = 0.4$ %. The vertical and horizontal black dotted lines in diamond 1 illustrate how the center of a diamond is determined. We labeled the centers of diamonds 1, 2, 3, 4 with squares, circles, upward and downward triangles, respectively. The blue markers are for the $\Delta\varepsilon_{\mathrm{mech}} = 0$ diamonds and the light red markers for the $\Delta\varepsilon_{\mathrm{mech}} = 0.4$ % data. We observe that the center of each diamond shifts to the left with strain. This trend is confirmed by data sets at several other strain values,

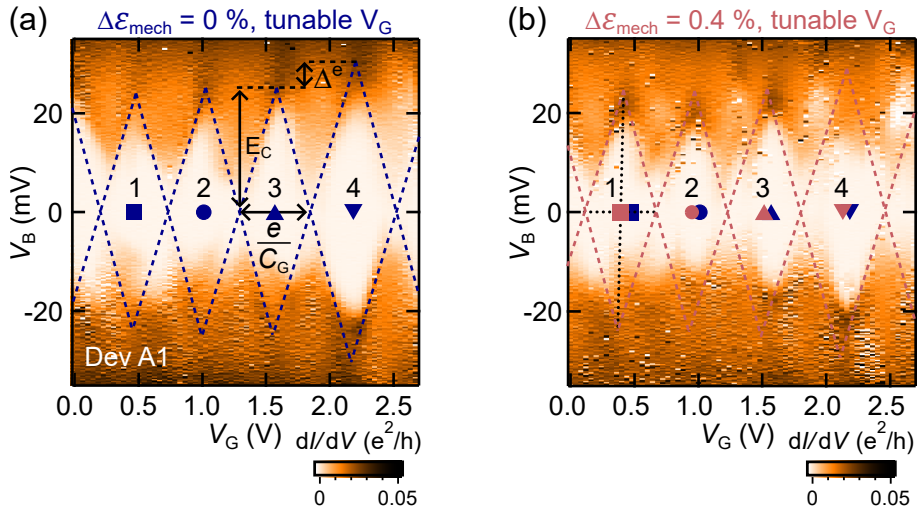

Figure 4.10: Coulomb diamonds for Device A1 under $\Delta\varepsilon_{\text{mech}}$. (a)-(b) $dI/dV_{\text{B}} - V_{\text{B}} - V_{\text{G}}$ data from Device A1 at $\Delta\varepsilon_{\text{mech}} = 0$ and 0.4 %, respectively.

as shown in Sec. 4.3.2. Figure 4.11(a) shows an enlarged version of the measured diamond shifts ΔV_{G} for diamond 2 as $\Delta\varepsilon_{\text{mech}}$ increases from 0 to 0.5 %.

Figure 4.11(b) summarizes all shifts of diamonds 1 (squares), 2 (circles), 3 (triangles), 4 (downward triangles) versus strain. We observe a linearly increasing shift ΔV_{G} with $\Delta\varepsilon_{\text{mech}}$. The right hand-side axis gives the Fermi energy shift on the QD $\Delta\mu_{\text{G}} = \alpha e \Delta V_{\text{G}}$, where α is the ratio between half the diamond height and its width. The dashed line is a linear fit to the data, and its slope gives $\Delta\mu_{\text{G}} = 7.5 \pm 0.3$ meV/%. As will be discussed below, this is consistent with predicted [38, 51] strain-induced potentials ϕ_ε and $\mathbf{A}_{\text{hop}}$ being added to the SWCNT-QD. Practically, this means that it is possible to gate (dope) the QD using purely mechanical means. One advantage of this "mechanical-gating" is that unlike electrostatic-gating it cannot be screened by the QD environment such as nearby metallic contacts, and could be useful in single-molecule electronics [37].

As shown in Fig.4.12 and 4.13, *in-situ* strain control of the QD doping is observed even more dramatically in Devices A2 and B. It is important to notice that although the $dI/dV_{\text{B}} - V_{\text{B}} - \Delta\varepsilon_{\text{mech}}$ data in Fig.4.12 and 4.13 may resemble the data in the color plots of Fig.4.10, the horizontal axis is no longer V_{G} but rather $\Delta\varepsilon_{\text{mech}}$. These data were acquired at constant $V_{\text{G}} = 0$. Fig. 4.12(a) shows $dI/dV_{\text{B}} - V_{\text{B}} - \Delta\varepsilon_{\text{mech}}$ for Device A2 for a forward (increasing) strain sweep from 0 to 1.2 %, and Fig.4.12(b) shows the reverse (decreasing) strain sweep. The data are highly reproducible and fully reversible, confirming again that there is no slippage of the tube under the gold clamps. Additional data and analysis details for Devices

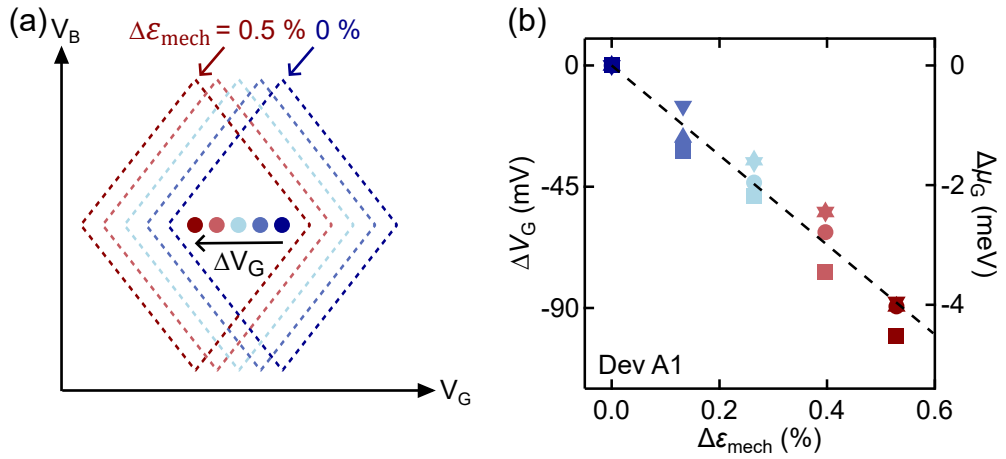

Figure 4.11: Mechanically-tunable Coulomb diamond V_G shifts. (a) Outline of the Coulomb diamond 2 extracted from Fig. 4.10(a)-(b) and similar data at $\Delta\varepsilon_{mech}$ between 0 (blue) and 0.5 (red)%. The center of the diamonds are labelled with circle markers. (b) The ΔV_G shift of diamonds 1 (squares), 2 (circles), 3 (triangles), 4 (downward triangles) versus $\Delta\varepsilon_{mech}$. The right-hand side axis shows the corresponding channel energy shift, $\Delta\mu_G = \alpha e \Delta V_G$. The dashed line is a linear fit whose slope is 7.5 ± 0.3 meV/%.

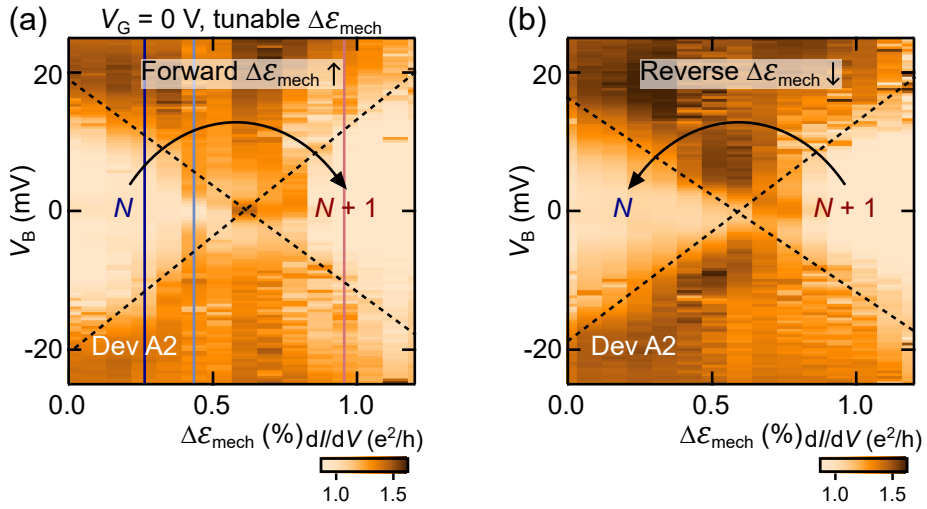

Figure 4.12: Mechanical gating in a SWCNT-QD. (a) $dI/dV - V_B - \Delta\varepsilon_{mech}$ data from Device A2 for a forward (increasing) $\Delta\varepsilon_{mech}$ sweep. (b) Same as (a), but for a reverse (decreasing) $\Delta\varepsilon_{mech}$ mechanical sweep. The labels N and $N+1$ refer to the average number electrons on the QD.

A2 and B are provided in Sec. 4.3.2.

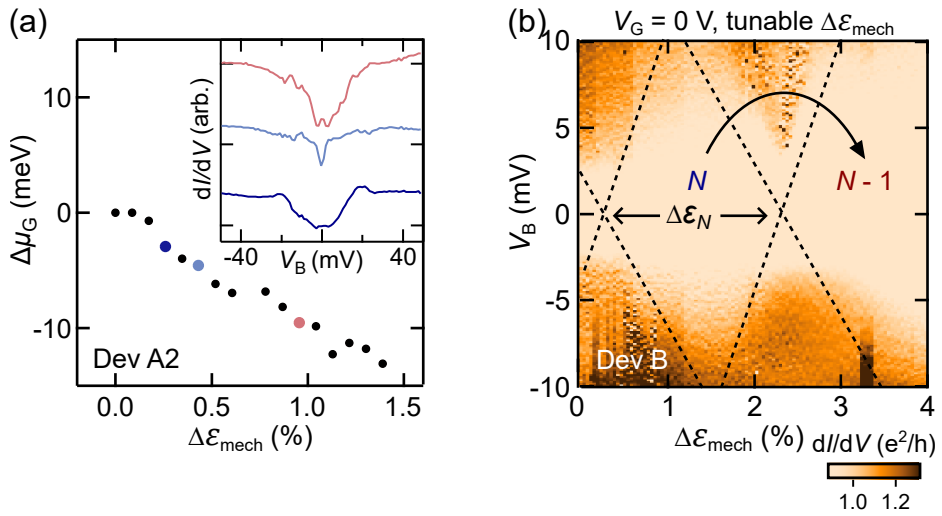

Figure 4.13: Mechanical doping and workfunction tuning of SWCNT-QDs. (a) The main panel shows $\Delta\mu_G - \Delta\varepsilon_{\rm mech}$ data for Device A2. The inset shows $dI/dV - V_{\rm B}$ data extracted from Fig. 4.12(a) at the location of the vertical cuts highlighted in dark blue, light blue, and red, respectively. (b) Same as Fig. 4.12(a), but for Device B. Increasing $\Delta\varepsilon_{\rm mech}$ removes more than one electron.

We remark that the finite differential conductance dI/dV near $V_{\rm B} = 0$ indicates that Device A2 is an open quantum dot. Most importantly, well-defined diamond-like features are observed in the data, showing that we can use *in-situ* tunable strain to add one full electron (on average) to the QD as we move the system from the regions labelled N to $N+1$ in Fig.4.12.

The inset of Fig.4.13(a) shows the $dI/dV_B - V_B$ data traces extracted from the dark blue, light blue, and red vertical data cuts in Fig.4.12(a). As $\Delta\varepsilon_{\rm mech}$ increases, the width of the low-conductance region shrinks and then grows again. A complete $dI/dV_B - V_B - V_G$ data set was recorded at each mechanical position (Sec. 4.3.2). Using these data, we extracted the V_G-position of the charge degeneracy point (diamond crossing) at each $\Delta\varepsilon_{\rm mech}$. As discussed above for Fig.4.11(b), we then calculate the channel's $\Delta\mu_{\rm G} = \alpha e \Delta V_{\rm G}$. Figure 4.13(a) shows $\Delta\mu_{\rm G}$ vs $\Delta\varepsilon_{\rm mech}$ in Device A2. We observe that the Fermi energy of the QD can be tuned mechanically by over 13 meV using a 1.3% strain. We emphasize that the ability to tune the charge state of the QD by a full electron is important in the context of quantum technologies [5]. For instance, adding a full electron to a closed QD (Fig. 4.10) can flip its spin state.

Figure 4.13(b) shows $dI/dV{\rm B} - V_{\rm B} - \Delta\varepsilon_{\rm mech}$ data for Device B. Once again, we see a clear

strain control of the charge number on the QD. One striking difference is that increasing strain removes an electron (from N to $N-1$), meaning that strain increases $\Delta\mu_{\mathrm{G}}$. The sign of $\Delta\mu_{\mathrm{G}}$ observed directly in the $dI/dV_B - V_B - V_G$ data (Sec. 4.3.2) from the shift direction of the Coulomb diamonds in the $dI/dV - V_{\mathrm{B}} - V_{\mathrm{G}}$ maps.

4.3.2 Supporting material

In Fig. 4.10, we show the Coulomb diamonds for Device A1 at $\Delta\varepsilon_{\mathrm{mech}} = 0\%$ and 0.4%, respectively, to demonstrate their lateral shift. In this section, we present a more detailed analysis of the diamonds and additional data at different strain values to illustrate the continuous shift.

Figure 4.14 shows the dI/dV–V_{B}–V_{G} data for Device A1 at $\Delta\varepsilon_{\mathrm{mech}} = 0\%$, 0.13%, 0.25%, 0.4%, and 0.53%. Diamonds 1–3 have similar widths of approximately 0.56 V, from which the gate capacitance is extracted as $C_{\mathrm{G}} = e/0.56\mathrm{V}$=0.29 aF, where e is the elementary charge. The channel length can then be estimated using the wire-over-plane capacitor model [63,79]:

$$\frac{C_{\mathrm{G}}}{L_{\mathrm{G}}} = \frac{2\pi\varepsilon_{\mathrm{ox}}}{\frac{\varepsilon_{\mathrm{ox}}}{\varepsilon_{\mathrm{vac}}}\cosh^{-1}\left(\frac{t_{\mathrm{vac}}}{r}\right) + \cosh^{-1}\left(\frac{t_{\mathrm{vac}}+t_{\mathrm{ox}}}{r+t_{\mathrm{vac}}}\right)} \tag{S7}$$

where $\varepsilon_{\mathrm{ox}}$ and $\varepsilon_{\mathrm{vac}}$ are the permittivities, t_{ox} and t_{vac} are the thicknesses of the oxide and vacuum spacers, respectively, and r is the nanotube radius ($d/2$). The calculated channel length is $L_{\mathrm{G}} = 31$ nm, which agrees well with the observed length of 28 nm from the SEM image in Fig. 4.2.

Diamonds 1–3 also have similar heights of approximately 25 mV, corresponding to the charging energy E_{C}. Diamond 4 exhibits a larger height due to the energy level spacing, denoted as $\Delta^e \approx 6$ meV. Such a small level spacing has been observed in a SWCNT quantum dot with a similar channel length in our previous work [63]. A small bandgap was also reported in that nanotube, suggesting that Device A1 experiences an initial strain.

The centers of the Coulomb diamonds are identified by drawing their diagonal lines, marked by rectangular, circular, upward-triangular, and downward-triangular symbols. A continuous leftward shift is observed, and the gate voltage shifts of all four diamonds at different mechanical strain are plotted in Fig. 4.11, showing a clear linear relationship. Since the diamond width also reflects the charging energy, a conversion factor $\alpha = E_{\mathrm{C}}/\mathrm{width}$ can then be determined to be 0.045. This factor is used to calculate the gate potential change corresponding to the gate voltage shift under strain, $\Delta\mu_{\mathrm{G}} = \alpha e \Delta V_{\mathrm{G}}$, also shown in Fig. 4.11.

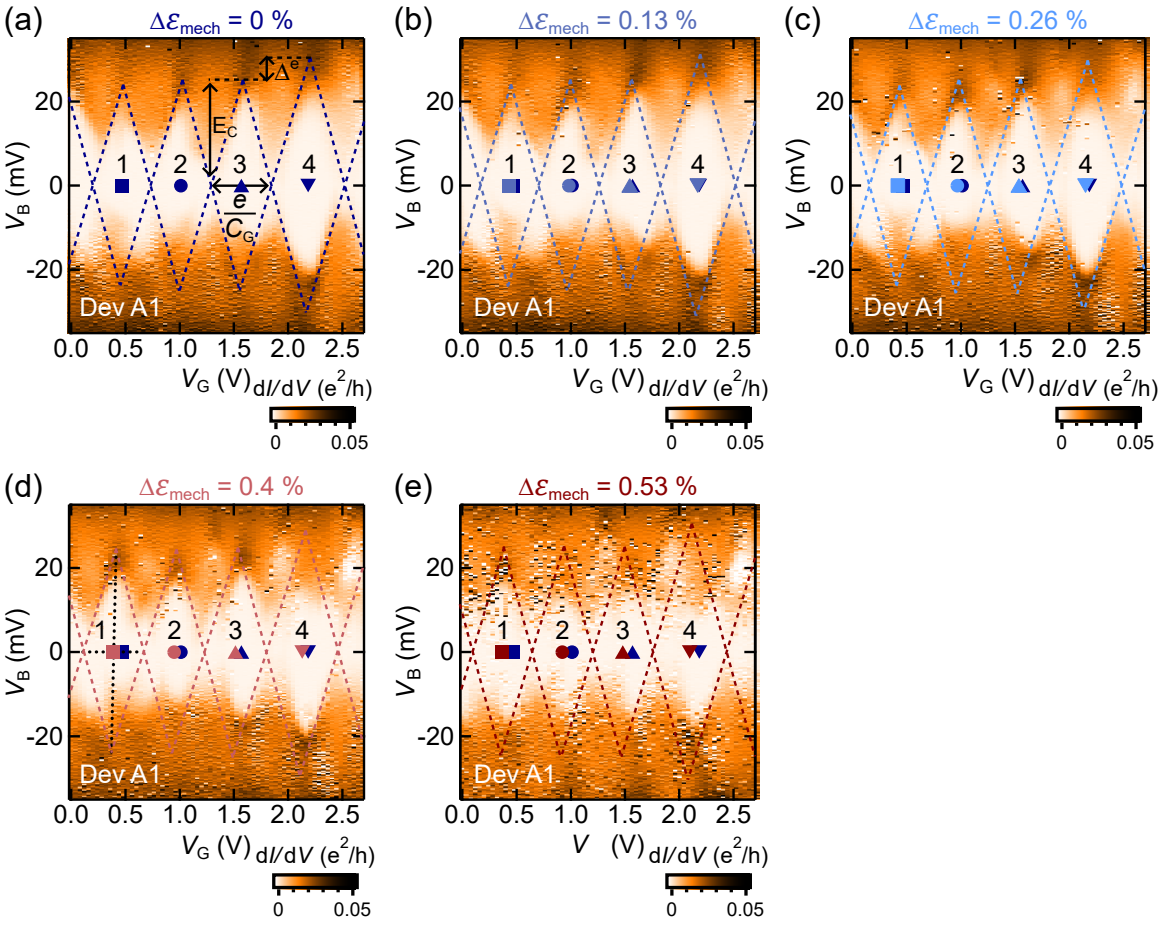

Figure 4.14: Shift of Coulomb diamonds in a SWCNT-QD (Device A1) under mechanical strain. (a) At $\Delta\varepsilon_{\mathrm{mech}} = 0\%$, Device A1 shows well-defined Coulomb diamonds of a closed QD. The charging energy $E_{\mathrm{C}} = 25$ meV is obtained from the maximum bias voltage of the diamond, and its width reflects the gate capacitance e/C_{G}. The maximum bias voltage difference between the diamond 3 and 4 $\Delta^e \approx 6$ meV originates from discrete energy levels in the QD. Diamond centers are marked with symbols of different shapes. (b)–(e) dI/dV-V_{B}-V_{G} in Device A1 at $\Delta\varepsilon_{\mathrm{mech}} = 0.13\%$, 0.26%, 0.4%, and 0.53%. All diamonds shift leftward with increasing strain.

When electrostatic gate control is weak or absent, mechanical strain provides an alternative means to tune energy levels in the channel, as illustrated in Fig. 4.12 and 4.13 for Devices A2 and B. This section presents additional data and analyses illustrating mechanical gating in weakly coupled SWCNT quantum dots.

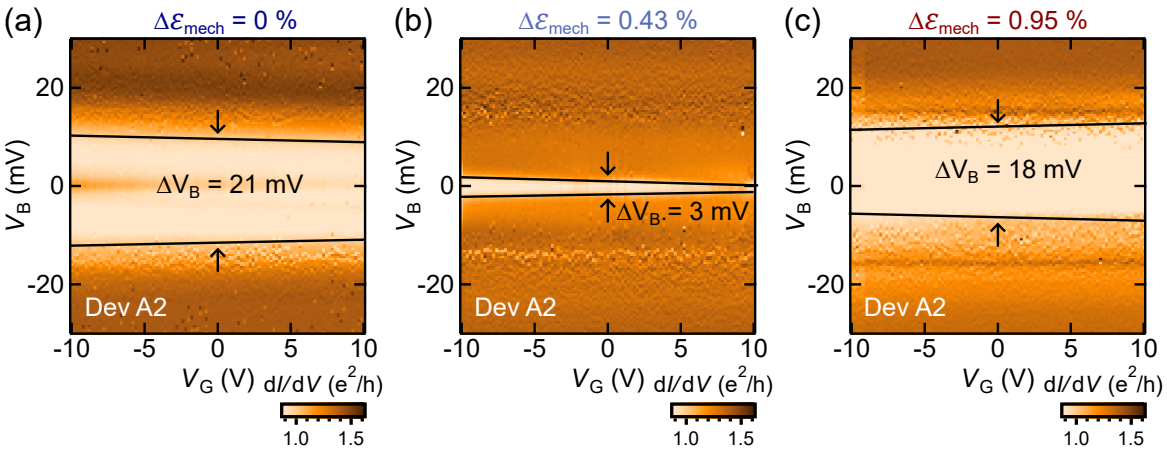

Figure 4.15: Leftward shift of Coulomb diamonds with increasing mechanical strain in Device A2. (a) At $\Delta\varepsilon_{\mathrm{mech}} = 0\%$, the diamond narrows with increasing gate voltage, and its height at $V_{\mathrm{G}} = 0$ V is 21 mV. (b) At $\Delta\varepsilon_{\mathrm{mech}} = 0.43\%$, the diamond continues to narrow with V_{G}, and the height at $V_{\mathrm{G}} = 0$ V is 3 mV. (c) At $\Delta\varepsilon_{\mathrm{mech}} = 0.95\%$, the diamond widens with increasing V_{G}, and the height at $V_{\mathrm{G}} = 0$ V is 18 mV.

Figure 4.15 presents the dI/dV–V_{B}–V_{G} data of Device A2 at $\Delta\varepsilon_{\mathrm{mech}} = 0\%$, 0.43%, and 0.95%. A clear leftward shift of the Coulomb diamond with increasing strain is observed, similar to that in Device A1. The bias voltage difference at the diamond edges at $V_{\mathrm{G}} = 0$ V decreases from 21 mV to 3 mV and then increases to 18 mV under equal $\Delta\varepsilon_{\mathrm{mech}}$ increments, consistent with the linear strain dependence of the gate potential shift. Unlike Device A1, no complete diamond appears within the gate sweep range, preventing the use of diamond centers to quantify the shift. Instead, we extract ΔV_{G} from the diamond-edge slopes and the corresponding bias voltage variations. Using $\Delta\mu_{\mathrm{G}} = \alpha e \Delta V_{\mathrm{G}}$, where $\alpha = C_{\mathrm{G}}/(C_{\mathrm{S}} + C_{\mathrm{G}} + C_{\mathrm{D}}) = 2.9 \times 10^{-5}$, the strain dependence of the gate potential is plotted in Fig. 4.13(a).

In contrast to Device A1 and A2, Device B shows a rightward shift of the Coulomb diamonds with increasing strain, as illustrated in Fig. 4.16. The color scale has been adjusted to emphasize this shift, particularly the feature indicated by black arrows. The opposite shift direction reveals that the mechanical gating effect cannot be explained solely by the strain-induced scalar potential, which would shift all SWCNT diamonds in the same (leftward) direction. This behavior instead suggests a contribution from chirality-dependent vector potentials that modify the band structure and open the band gap in the SWCNT. The

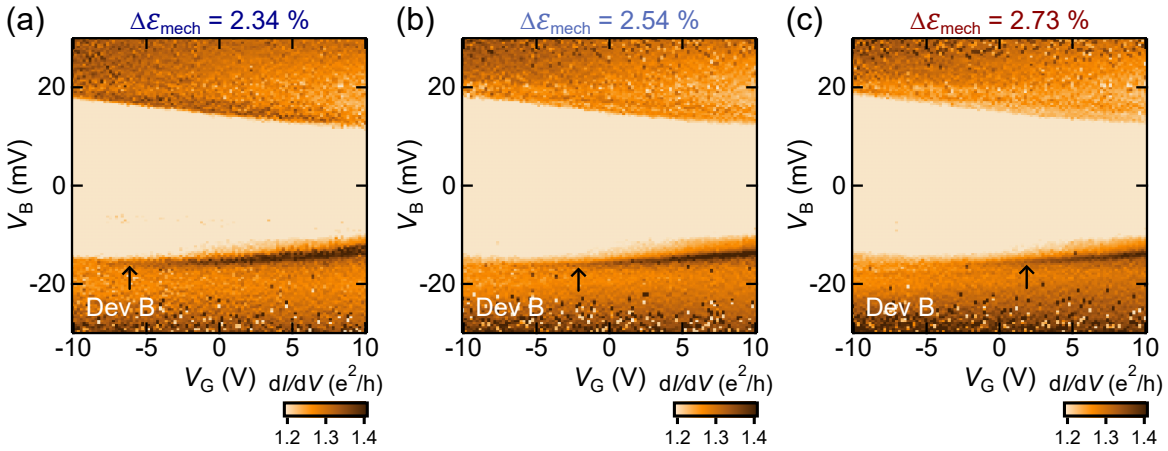

Figure 4.16: Rightward shift of Coulomb diamonds with increasing mechanical strain in Device B. (a)–(c) dI/dV–V_B–V_G maps at $\Delta\varepsilon_{mech}$ = 2.34%, 2.54%, and 2.73%. The high-conductance feature, whose left edge is marked by black arrows, shifts rightward with increasing strain, showing an equal gate-voltage shift for each strain increment.

underlying mechanism of this mechanical gating will be discussed in the following section.

4.4 Physical origin of mechanical gating in our SWCNT transistors

4.4.1 Main results

The observed mechanically-induced QD charge control is fundamentally different than previous reports [73,98,99], because it originates from band-structure modifications of the material and offers a predictable control. Figure 4.17 and 4.18 show evidence of the stark difference between the mechanically-induced doping in previous movable QDs, arising from capacitance changes (Figs.4.17), and our strain-tunable band structure QDs (Figs.4.18).

We briefly review the effect of mechanically-tunable QD capacitances on transport to understand why it cannot explain the data presented above. As shown in Fig.4.17(a), in previous mechanically-controlled QD (mechanical break-junctions) the QD was affixed to a metal contact (e.g. source) and free to move a distance Δx away from another metal contact (e.g. drain). This configuration leads to a mechanically-dependent QD-drain capacitance, C_D, and roughly constant QD-source, C_S, and QD-gate, C_G, capacitances. Based on this geometry (Sec. 4.4.2), the left-hand side of Fig. 4.17(b) shows the expected change in the Coulomb diamonds in Device A1 between the measured data at $\Delta x = 0$ $\mathring{A}$ (blue) and the expected (calculated) data for Δx =4 $\mathring{A}$ (red). We note that the height and slopes of the

expected red Coulomb diamond are significantly modified by Δx. The right-hand side of Fig. 4.17(b) shows that actual measured diamonds at $\Delta x = 0$ (blue) and 4 (red) $\mathring{A}$ did not change shape, in clear disagreement with the capacitive model.

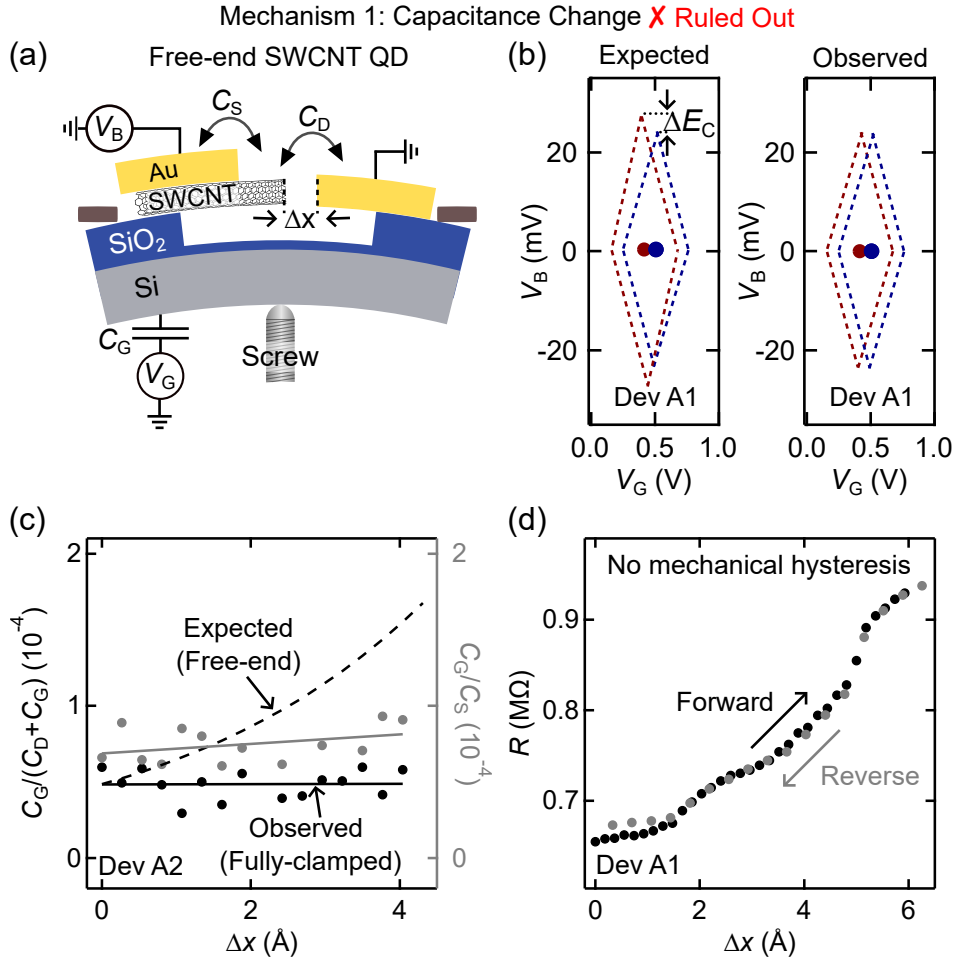

Figure 4.17: Ruled-out mechanism for mechanical gating in our SWCNT transistors. (a) Diagram showing the geometry of previously reported mechanically-controlled QDs (mechanical break-junctions). The QD was affixed to a metal contact (e.g. source) while free to move a distance Δx away from another metal contact (e.g. drain). (b) The expected change, based on the geometry in (a), in the Coulomb diamond shape for Device A1 between $\Delta x = 0$ $\mathring{A}$ (measured, blue) and Δx =4 $\mathring{A}$ (calculated, red). The right-hand side diamonds show that the actual measured diamonds at $\Delta x = 0$ (blue) and 4 (red) $\mathring{A}$ did not change shape. (c) The measured slopes (solid markers) of the diamonds in Device A2 at various Δx. The solid lines are linear fits to the data. The dashed line shows a conservative estimate (Sec. 4.4.2) of the expected change in the diamond slopes based on the device geometry in (a). (d) R–Δx for Device A1 during forward and reverse motion shows no mechanical hysteresis. Similar data for Devices A2 and B are provided in Sec. 4.4.2.

In Fig.4.17(c), we plot the measured slopes of the diamonds in Device A2 at various Δx.

The upward slopes (black markers) and downward slopes (grey markers) correspond to the quantities $C_G/(C_D + C_G)$ and C_G/C_S, respectively. The solid lines are linear fits to the data and show that the capacitances are nearly constant. The dashed line shows a conservative estimate (Sec. 4.4.2) of the expected change in the diamond slopes if our QDs had the geometry shown in Fig.4.17(a). This further supports that the capacitances in our QDs do not change as we move the gold clamps.

This implies that both ends of our SWCNT-QDs are firmly anchored by the gold. Further evidence of this is visible in Fig.4.17(d) where we show the resistance, R, of Device A1 as we ramp up (forward) and down (reverse) the mechanical displacement Δx. The extremely good reversibility of the mechanical sweep is only compatible with a nanotube which is firmly clamped at both ends, and elastically stretched as a function of Δx. Collectively, the above data rule out capacitance changes as the primary mechanism for the mechanical dependence of our QDs' charge transport.

Figure 4.18 show how the strain-induced band structure modifications of the SWCNT-QDs lead to a quantitatively accurate description of our observed mechanical-gating effect. Figure 4.18(a) shows how a uniform uniaxial strain $\Delta\varepsilon = \Delta x/L$ is applied to the suspended nanotube channel [36]. Figure 4.18(b) summarizes the expected strain-induced band structure modifications, as previously reported [38] and discussed in Sec. 4.4.2. The solid blue (red) line in the left (right) Dirac cone of Fig.4.18(b) shows the lowest electronic subband in a quasi-metallic SWCNT with $\varepsilon_{\text{mech}} = 0$ ($\varepsilon_{\text{mech}} \neq 0$). The Fermi level in the channel, μ_C, is shown by the horizontal black dotted line. We note that the work function of Au clamps remains unchanged during mechanical motion, supported by the exponential increase in Au tunnel junction resistance upon chip bending and its agreement with a tunnel junction model with constant Au work function [52].

When a uniaxial strain is applied to the SWCNT channel, the modifications to the transport subband (solid red line in Fig.4.18(b)) can be described by two new potentials. First, a scalar potential ϕ_ε shifts the entire dispersion (Dirac cones) down in energy relative to the unstrained source/drain SWCNT contacts. The magnitude of this scalar potential is [38, 52, 67] $e\phi_\varepsilon = (g_\varepsilon)(1 - \nu)\varepsilon_{\text{total}}$, where ν is the Poisson ratio 0.165 and $g_\varepsilon \approx 3.0$ eV, leading to a leftward shift of the Coulomb diamonds at a rate of ≈25 meV per 1 % mechanical strain. This effect is independent of the SWCNT chirality. We note that our nanofabrication process has been shown to naturally selects very small bandgap nanotubes [63], such as quasi-metallic ones. This is because metallic tubes have much higher contrast in scanning electron imaging (see Sec. 4.3.2).

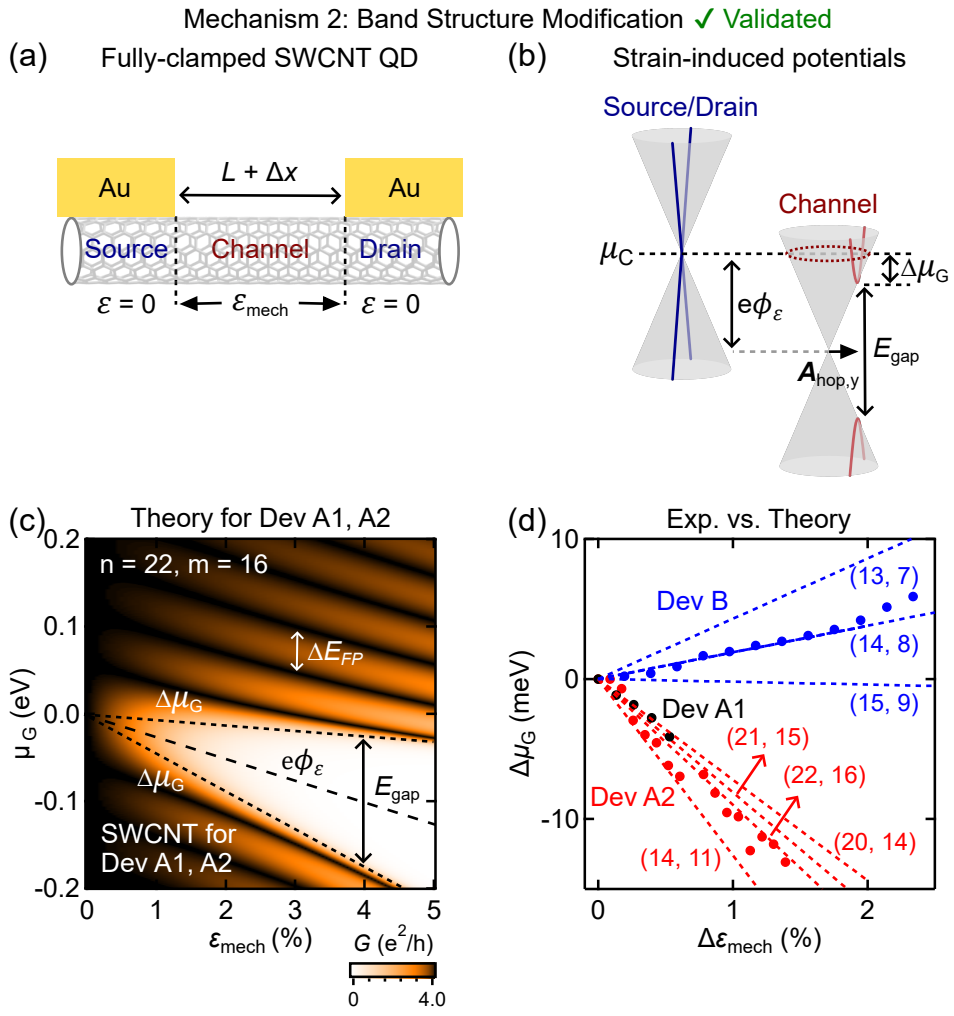

Figure 4.18: Physical origin of mechanical gating in our SWCNT transistors. (a) Diagram showing the geometry of the presently reported mechanically-controlled QDs. The QD is firmly clamped at both ends and uniaxially stretched as the clamps are moved, leading to predictable bandstructure modifications. (b) Energy level and band structure of SWCNT channel without (left cone) and with strain (right cone). Strain-induced scalar potential shifts the Dirac cone downwards by $e\Phi_\varepsilon$. Strain-induced vector potential $A_{\mathrm{hop,y}}$ opens a band gap the Dirac cone in *k-space*, leading to a bandgap E_{gap}. The total $\Delta\mu_{\mathrm{G}}$ is given by $e\Phi_\varepsilon$ - $E_{\mathrm{gap}}/2$. (c) Caculated $G - \varepsilon_{\mathrm{total}} - \mu_{\mathrm{G}}$ for a SWCNT with a chirality (22,16) likely corresponding to Devices A1 and A2. (d) The measured $\Delta\mu_{\mathrm{G}}$ vs $\Delta\varepsilon_{\mathrm{mech}}$ in Devices A1, A2, and B. The dashed lines are theoretical calculations.

Secondly, a vector potential $\boldsymbol{A}_{\rm hop}$ shifts the k-position of the Dirac cones. If we define the x-axis along the length of the tube, then the y-component is $A_{{\rm hop},y} = \frac{\beta\varepsilon(1+\nu)}{2a}\cos 3\theta_h$, where a =1.42 Å is the nearest-neighbor carbon-carbon distance without strain. $\theta_h = \tan^{-1}\left(\frac{\sqrt{3}\,m}{2n+m}\right)$ is the angle between the tube's chiral vector $\boldsymbol{C}_h$ and the zigzag lattice direction [38,47]. This k-shift of the subband leads to a strain tunable band gap $E_{\rm gap} = 2\hbar v_{\rm F} A_{{\rm hop},y}$, as shown in Fig.4.18(b). This latter potential is chirality-dependent. The combination of these two effects leads to the total electrostatic potential shift $\Delta\mu_{\rm G} = -e\phi_\varepsilon \pm E_{\rm gap}/2$, with the sign depending on the type of charge carriers [38].

To compare quantitatively the theoretical expectations with our measurements, Fig.4.18(c) shows a detailed calculation [38] of charge conductance $G = I/V_{\rm B}$ (color scale) as a function of $\varepsilon_{\rm mech}$ and $\mu_{\rm G}$, for a quasi-metallic SWCNT with chirality (22,16). This chirality is the likely candidate for Devices A1 and A2. The calculated spectrum is only weakly dependent (Sec. 4.4.2) on the minor chirality changes allowed to match both the measured tube diameter (2.1 nm) and the $\Delta\mu_{\rm G} - \Delta\varepsilon_{\rm mech}$ slope shown in Fig. 4.13(a).

The dark stripes in Fig. 4.18(c) indicate the energy-strain positions where the SWCNT energy levels have resonant transmission. The central dashed line indicates the scalar potential energy shift, $e\phi_\varepsilon$. The white region corresponds to the strain-induced band gap resulting from $A_{\rm hop,y}$. The sharp boundaries (dotted black lines) of the band gap region, indicate the electrostatic potential energy shift $\Delta\mu_{\rm G} - \Delta\varepsilon_{\rm mech}$. The upper black dotted line corresponds to the conduction band edge (electrons), while the lower one corresponds to the valence band edge (holes).

Since the electrostatic potential energy shift is chirality dependent, it can determine the chiral angle of a SWCNT. When combined with our tube diameter measurements, it constrains the possible chiralities to just a few. Figure 4.18(d) plots the experimental data for $\Delta\mu_{\rm G}$ vs $\Delta\varepsilon_{\rm mech}$ from Devices A1 (black), A2 (red) and B (blue). The experimental data were extracted as discussed previously over Figs.4.11(b) and 4.13(a). Devices A1 and A2 show nearly identical negative linear trends, consistent with their fabrication on the same SWCNT. Device B, in contrast, shows a positive slope of different magnitude.

By fitting the data (dashed lines), the chiral angles for the two SWCNTs are extracted. For Devices A1 and A2, we find $\theta = 25 \pm 0.5$ °, and for Device B, $\theta = 20.8 \pm 0.3$ °. Combined with the measured diameters of 2.1 ± 0.5 nm (Devices A1/A2) and 1.6 ± 0.4 nm (Device B), the most likely chiralities are (n = 22, m = 16) or (21, 15) for Devices A1/A2 and (14,8) for Device B. Figure 4.18(d) shows the quantitative agreement between the model (dashed lines) and the experimental data (markers) from all three devices. The agreement remains very

good for all plausible chiralities. Other chiralities corresponding to quasi-metallic SWCNTs with diameters within the measured range yield poor fitting results and even the best cases among them deviate noticeably from the measured data, as shown in the figure. This fitting approach therefore provides an additional means to determine the nanotube chirality.

4.4.2 Supporting material

Figure 4.17 and 4.18 demonstrate that the mechanical gating observed in our experiments originates from the strain-dependent SWCNT band structure rather than from capacitance variations. In this section, we present additional data and analysis confirming that the devices are fully clamped and exhibit no significant capacitance change over a broad strain range. We then describe the theory model used to calculate the transport behavior of the SWCNT devices and use it to simulate the transport characteristics of Device B.

For free-end quantum dots (Fig. 4.17(a)), the distance between the quantum dot and the Au electrode changes with mechanical motion, altering the source and drain capacitances and potentially shifting the Coulomb diamonds. To rule out this effect, we first verify that the QD capacitance remains constant over a broad range of mechanical motion. We then present highly reproducible transport data obtained during forward and reverse mechanical motion, providing further evidence that the nanotube is fully clamped.

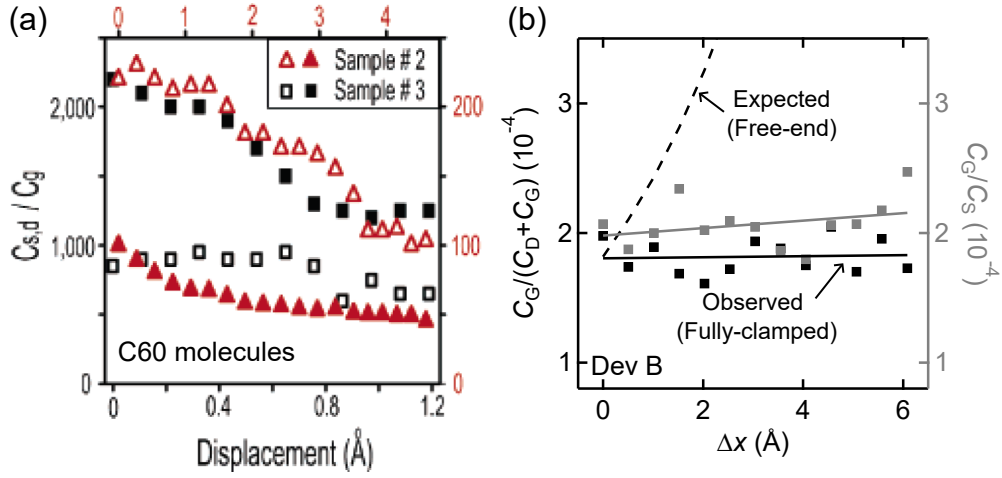

Figure 4.19: Evidence of full clamping in SWCNT devices. (a) Capacitance variation in a C_{60} molecular transistor as the electrodes separate. Figure adapted from Ref. [73]. (b) The capacitance ratio predicted by the free-end quantum dot model shows much larger variation than observed experimentally in our devices.

Figure 4.19(a) shows the capacitance change measured in two C_{60} molecular transistors

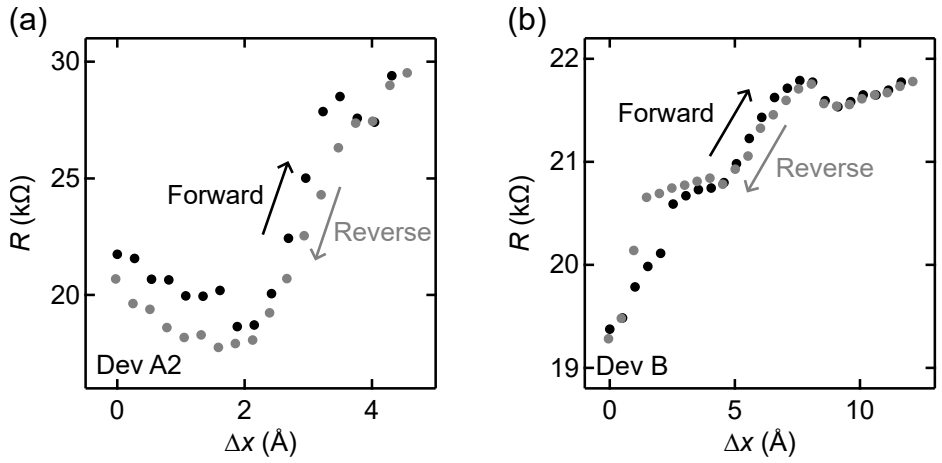

Figure 4.20: No mechanical hysteresis in SWCNT devices. (a)–(b) R–Δx data for Devices A2 and B during forward and reverse mechanical motion.

(squares and triangles) from literature [73]. The black and red traces represent $C_{\mathrm{D}}/C_{\mathrm{G}}$ and $C_{\mathrm{S}}/C_{\mathrm{G}}$, respectively. Because one side of the C_{60} molecule couples more strongly to an electrode, either the source or drain capacitance varies significantly [73]. Based on their results, we estimate that C_{S} or C_{D} changes by approximately 12% and 42% per 1 Å. For the following analysis, we used an intermediate value of 25% and described it as $C_{\mathrm{D}} = C_{\mathrm{D0}}(1 - 25\%)^{\Delta x/1\ \text{Å}}$, where C_{D0} denotes the initial capacitance. Figure 4.19(b) plots the capacitance ratio versus displacement Δx, comparing the calculated variation (dashed line) with the experimental ratios (black and gray points) for $C_{\mathrm{G}}/(C_{\mathrm{D}} + C_{\mathrm{G}})$ and $C_{\mathrm{G}}/C_{\mathrm{S}}$. The measured ratios remain nearly constant (solid black and gray lines) across displacements of 6 Å for Device B and 4 Å for Device A2 (Fig. 4.17(c)), while the free-end model predicts much larger changes. This result rules out capacitance variation as the origin of mechanical gating. Furthermore, the transport data are highly reproducible across a broad mechanical range (Fig. 4.17(d) and Figs. 4.20), confirming the absence of hysteresis and indicating that the SWCNTs are fully clamped.

We computed the G–$\Delta\mu_{\mathrm{G}}$–$\varepsilon_{\mathrm{mech}}$ characteristics shown in Fig. 4.18(c) and Fig. 4.21(b) for quasi-metallic (21,15) and (14,8) nanotubes under strain $\varepsilon = 0$–5%. A clear bandgap opens with increasing strain due to the vector potential, while the spectral features shift as a result of the scalar potential. These two effects define the upper and lower edges (short dashed lines) in Fig. 4.21(b). The direction and magnitude of the $\Delta\mu_{\mathrm{G}}$ shift at these top and bottom edges depend on the nanotube chirality and carrier type. This explains the opposite shifting behavior in Devices A1/A2 and B. Considering this chirality-dependent $\Delta\mu_{\mathrm{G}}$ shift and the

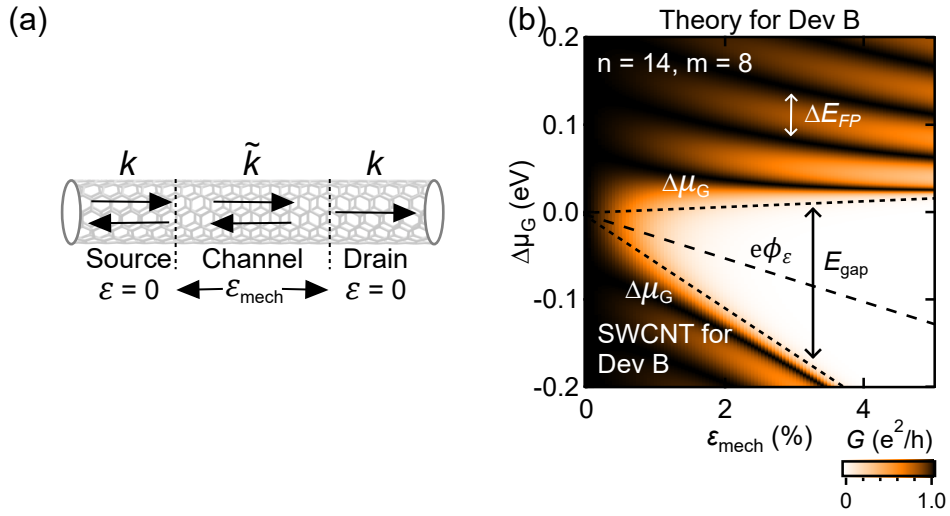

Figure 4.21: An applied theory for quantum transport in strained SWCNTs. (a) Diagram showing a 1D representation of the reflection and transmission of charge carriers across a strained SWCNT channel and unstrained SWCNT source/drain contacts. (b) Simulated conductance G as a function of $\Delta\mu_{\rm G}$ and $\varepsilon_{\rm mech}$ for Device B using the applied theory.

diameter relation $d = a\sqrt{n^2 + m^2 + nm}/\pi$ [48], we identified the most probable chiralities as $(n, m) = (21, 15)$ for Devices A1/A2 and $(n, m) = (14, 8)$ for Device B.

4.5 Conclusions

In conclusion, single-wall carbon nanotube transistors have atomically precise transverse boundary conditions and a single transport subband, making them ideal systems to study and harness quantum transport straintronics. We presented transport data from three SWCNT-QD transistors, whose channel is $\approx$ 30-nm-long, over a broad range ($\approx$ 0 to 4 %) of *in-situ* tunable and reversible uniaxial strain.

The precise reversibility of the data presented confirms that the tubes are firmly clamped mechanically and strained elastically. Using $dI/dV_{\rm B} - V_{\rm G} - V_{\rm B}$ data, we showed that the charge states of the QDs are widely tunable via strain. The agreement of the data with QTS theory calculations [38] confirmed that the mechanical tuning of the QDs stems from *quantitatively* predictable strain-induced scalar and vector potentials. This added mechanical-gating control of QD electronics could find applications in nanotube-based qubits [6] and quantum devices [7], as well provide a reliable way to gate single-molecule electronics devices [37].

Chapter 5

Other Contributions: Graphene QTS, SWCNT Electromechanical Resonators

In addition to the mechanical control of quantum transport in SWCNTs discussed in the previous chapters, we also studied QTS in ballistic graphene, and electromechanical resonances in SWCNT/graphene quantum dots. In this chapter, we first present measurements of quantum transport in strained graphene transistors which agree quantitatively with models based on strain-induced scalar and vector potentials.

A scalar potential $e\phi_\varepsilon$ was induced in-situ to modify graphene's work function by up to 25 meV. Vector potentials $\boldsymbol{A}$ suppressed the ballistic conductance of graphene by up to 30% and controlled its charge carriers' quantum interferences across the channel. The transport data were obtained with our custom experimental platform (Sec. 3.2) at low-temperature (1.3 K) over a broad range of strain (up to 2.6 %). This work was published in Advanced Materials: A. C. McRae, G. Wei, and L. Huang, *et al., Mechanical Control of Quantum Transport in Graphene*, Adv. Mater. **36** (23), 2313629 (2024), and I contributed mainly to theoretical calculations to model the experimental data.

We next present our latest measurements showing strain-tunable self-sustained electromechanical resonances in SWCNT and graphene QDs. Mechanical strain can widely tune both the coupling strength g and the range ΔV_G where we observed the electromechanical resonances. This ongoing work opens new opportunities to explore dynamical QTS, where oscillations can be described as time-dependent strains.

5.1 Mechanical control of quantum transport in graphene

Graphene has attracted extensive attention in recent years owing to its ability to form two-dimensional heterostructures and enable twistronics, as well as its ease of fabrication through exfoliation of graphite. In the following, we briefly summarize the main results from our published work on the mechanical control of quantum transport in graphene.

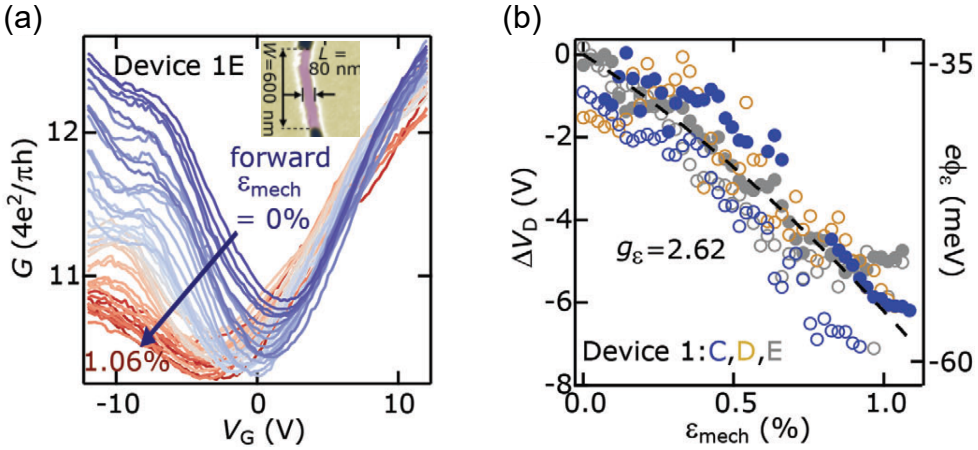

Figure 5.1: Mechanically-tunable scalar potential and work function in graphene. (a) G-V_{G} data in Device 1E, for a forward sweep (increasing $\varepsilon_{\mathrm{mech}}$) from 0% to 1.06%. The inset shows the dimensions of the graphene device. (b) The relative Dirac point shift ΔV_{D} (left axis) and scalar potential $e\phi_{\varepsilon}$ versus $\varepsilon_{\mathrm{mech}}$ in Device 1C, 1D and 1E. The open/solid markers are from forward and reverse sweeps. The dashed black line is a theoretical fit. Figure adapted from [52].

Unlike SWCNT devices, our graphene devices had short and wide channel to minimize the impact from edge disorder. The inset of Fig. 5.1(a) shows the dimensions of Device 1E, with length $L = 80$ nm and width $W = 600$ nm (width-to-length ratio ≈ 8). The main panel presents G–V_{G} curves over a range of mechanical strain increasing from 0% (dark blue) to 1.06% (dark red). The minimum conductance point corresponds to the Dirac point (also referred to as the charge neutrality point). The Dirac point clearly shifts leftward, indicating a downward shift of the Dirac cone in the channel, which is described by the scalar potential term $e\phi_{\varepsilon}$ in the Hamiltonian (the same as in SWCNTs). By extracting the gate voltage shift of Dirac point under strain, we find the same linear dependence for different devices, as shown in Fig. 5.1(b). C, D, E represents different anneals for the graphene device in (a). We can then determine g_{ε} by fitting the data to

$$\Delta V_{\mathrm{D}} = -\frac{e}{C_{\mathrm{G}}\pi(\hbar v_{\mathrm{F}})^2} g_{\varepsilon}^2 (1-\nu)^2 \varepsilon_{\mathrm{total}}^2 \tag{5.1}$$

where C_{G} is the capacitance per unit area and can be calculated using the parallel-plate capacitor model, v_{F} is the Fermi velocity, ν is the Poisson ratio, and $\varepsilon_{\mathrm{total}}$ is the total strain considering all sources of strain. g_{ε} is then extracted to be 2.62, in good agreement with theory [67, 100]. Figure 5.1(b) shows that we could *in-situ* tune the scalar potential by up to 25 meV with 1% strain.

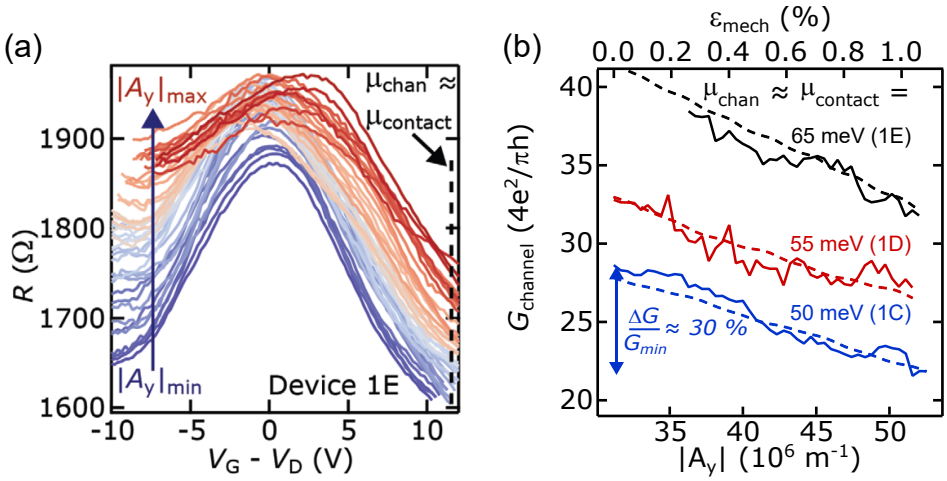

Figure 5.2: Mechanically-tunable conductance and vector potentials in quantum transport. (a) $R-(V_{\mathrm{G}}-V_{\mathrm{D}})$ in Device 1E for a forward $\varepsilon_{\mathrm{mech}}$ sweep from 0% (dark blue) to 1.06% (dark red). (b) G_{channel}-$|A_{\mathrm{y}}|$ for data extracted at $\mu_{\mathrm{chan}} \approx \mu_{\mathrm{contact}}$ (e.g. black dash line in (a)) for Device 1C, 1D, 1E. The conductance could be suppressed by up to 30%. Figure adapted from [52].

To isolate the effect of the mechanically induced gauge potentials A_y on our transport data, we removed the ΔV_{D} shifts from the raw data. Figure 5.2(a) shows the resulting R–$(V_{\mathrm{G}}-V_{\mathrm{D}})$ for $\varepsilon_{\mathrm{mech}}$ ranging from 0% (dark blue) to 1.06% (dark red) in Device 1E. We see that R changes smoothly over the full mechanical range. R along the vertical dash line, where $\mu_{\mathrm{channel}} \approx \mu_{\mathrm{contact}}$, is given by

$$R \approx \frac{h}{e^2 W}\left(\frac{4}{\pi}\tilde{k}_{\mathrm{F}} - |A_y|\right)^{-1} \tag{5.2}$$

The extracted (calculated) G_{channel} are solid (dashed) lines in Figure 5.2(b) for different anneals. We see that G_{channel} decreased almost linearly with increasing $|A_y|$. The relative decrease could reach up to 30% in Device 1C. We demonstrated that we can change the ballistic conductance, and create uniform gauge vector potential, in graphene using mechanical

strain. Beyond the effect of strain on the magnitude of conductance, we are also interested in its effect on the quantum phase of ballistic charge carriers.

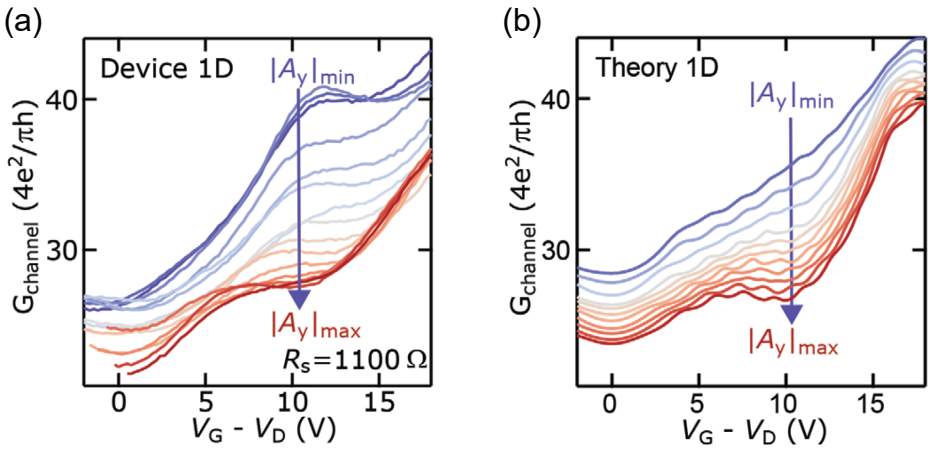

Figure 5.3: Mechanically-tunable quantum interferences. (a) G_{channel}-$(V_G - V_D)$ data for $\varepsilon_{\text{mech}}$ sweep ranging from 0% (dark blue trace) to 1.04% (dark red trace) in Device 1D. The vertical arrow shows the location of a strain-tunable quantum interference. (b) Theoretical modeling of the data in (a). Figure adapted from [52].

Figure 5.3 shows experimental and theoretical G_{channel}–$(V_G - V_D)$ data with increasing vector potential $|A_y|$ in Device 1D. We observe the mechanical tuning of quantum interference from constructive to destructive. However, because the conductance reflects the combined contribution of many conduction modes in graphene, the quantum interference phase cannot be exactly determined as in SWCNTs.

In summary, we measured ballistic transport in graphene under varying mechanical strain. We showed that strain can modify the work function of graphene by more than 25 meV, making this effect relevant even for room-temperature 2DM-based quantum technologies. We observed that an *in situ* uniaxial strain of approximately 1 % in graphene produces a smooth suppression of the ballistic charge conductance of up to 30 %. Finally, we observed mechanically tunable quantum transport interferences. We expect that our work will open new opportunities to control strain fields with a precision suitable for quantitative quantum transport studies in 2DMs and heterostructures.

5.2 Strain-tunable electromechanical resonances in SWCNT and graphene QDs

In a quantum dot device, electrons tunnel on and off the channel at a tunnelling rate Γ_e. Under a bias volatage, this tunnelling process induces charge pumping, i.e. electrons periodically jump on and off the channel, and modulates the electrostatic gating force and may drive self-sustained mechanical oscillations with a resonance frequency ω_m, as shown in Figure 5.4. The oscillation periodically changes the distance between the channel and the back gate, thereby modulating the channel's energy levels via capacitance variations. Such electromechanical resonances have been observed in many previous works on SWCNT quantum dots [101–106]. Here, we report how *in situ* mechanical strain tunes strength of such resonances.

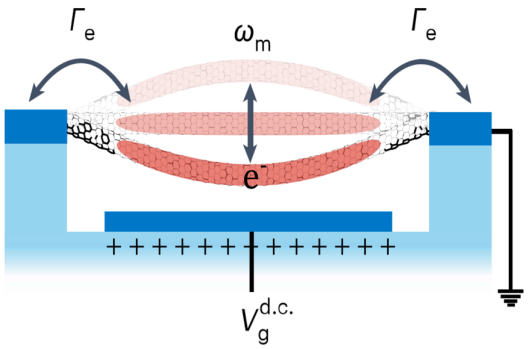

Figure 5.4: Self-oscillation in a suspended SWCNT quantum dot. A suspended SWCNT forms a quantum dot capacitively coupled to the DC gate voltage V_G and coupled to the leads via a tunneling rate Γ_e. Electrons driven on and off the dot by a DC bias modulate the electrostatic force between the dot and the gate, providing a feedback that induces self-sustained oscillations of the nanotube at its mechanical resonance frequency ω_m. Figure adapted from Ref. [101].

Figure 5.5 shows $I-V_G$ data, signature of an electromechanical resonance observed in our SWCNT-QD (Device A2), under $\Delta\varepsilon_{mech}$ ranging from 0% to 0.5% (dark blue to dark red). A clear current jump occurs at $V_G = -2$ V, and the maximum current change is denoted as ΔI_{Max}. The increased current persists over a gate voltage range ΔV_G before it starts to decrease. This current jump originates from electromechanical resonances in the SWCNT channel and depends on the strength of the electromechanical coupling. The coupling can be quantified by $g_{e,v} = e(C'_g/C_\Sigma)V_g^{d.c.}\sqrt{1/(2m\hbar\omega_{m0})}$, where C'_g is the spatial derivative of the gate capacitance, C_Σ is the QD total capacitance, $V_g^{d.c.}$ is the DC gate voltage, m is the

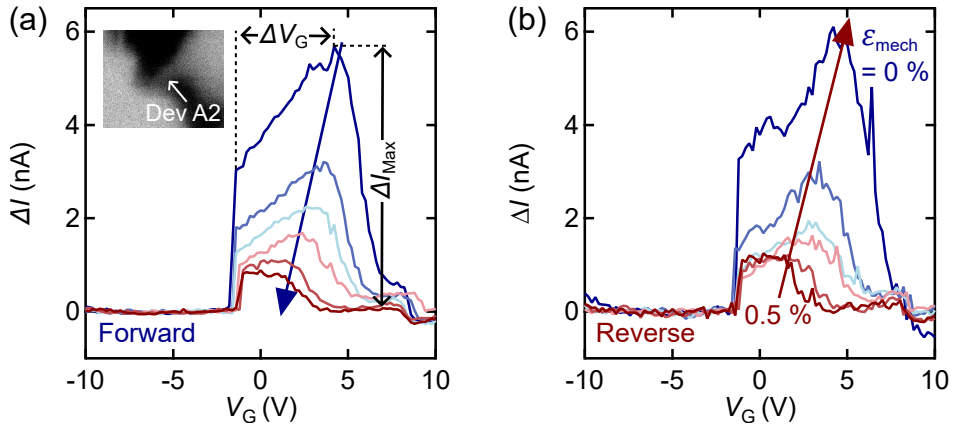

Figure 5.5: Strain-tunable electromechanical coupling in a SWCNT quantum dot. (a) ΔI–V_{G} for Device A2 at $\varepsilon_{\mathrm{mech}}$ from 0% to 0.5%. A sharp current increase occurs at $V_{\mathrm{G}} = -2$ V, with its amplitude and the corresponding gate voltage range denoted as ΔI_{Max} and ΔV_{G}, respectively. (b) Data taken during a reverse mechanical sweep show the same result as for a forward sweep.

effective mass, and ω_{m0} is the bare mechanical resonance frequency [101]. With increasing mechanical strain, ω_{m0} increases, which reduces the coupling $g_{\mathrm{e,v}}$ and consequently decreases the maximum current change ΔI_{Max}. This is qualitatively consistent with the results shown in Fig. 5.5, and the behavior is reproducible for both forward and reverse mechanical motions. It is also expected that strain increases Q (quality factor) of the oscillator, and for mismatched mechanical and tunnelling frequency, it would also reduce the effective $g_{\mathrm{e,v}}$.

To quantify the ability to tune electromechanical coupling via mechanical strain, we extracted ΔI_{Max} and ΔV_{G} as functions of $\varepsilon_{\mathrm{mech}}$ for both forward and reverse sweeps (Figure 5.6). The ΔI_{Max} decreases by more than 80 %, from 6 nA to 1 nA as the strain increases to 0.5 %. If only one electron tunnels through the channel per cycle, the tunnelling rate change could decrease from 40 GHz to 6 GHz, demonstrating a wide mechanical control. The resonance range ΔV_{G} decreases by more than 60 % from 5.5 V to 2 V, as shown in Figure 5.6(b), exhibiting a nearly linear dependence.

From the dI/dV–V_{B}–V_{G} data in Fig. 5.7, we can clearly define the resonance region as indicated by the white dashed lines. The width along the gate voltage ΔV_{G} decreases at higher mechanical strain, which is consistent with the data in Fig. 5.6. The transport behavior in this region, such as the Coulomb diamond edges, is also modified.

This strain-tunable electro-mechanical coupling is also observed in our graphene QDs. Figure 5.8(a) shows the current jumps at different V_{B} under various $\Delta\varepsilon_{\mathrm{mech}}$ in a graphene QD (inset). The differential conductance dI/dV as a function of V_{B} and $\Delta\varepsilon_{\mathrm{mech}}$ is shown

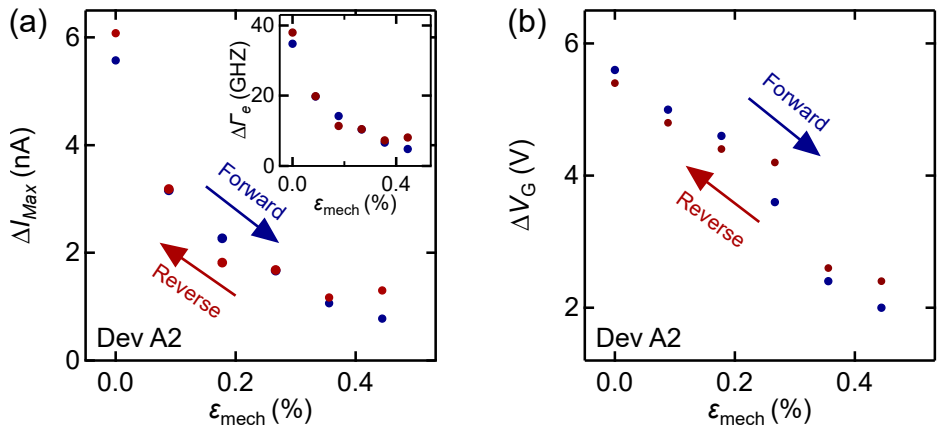

Figure 5.6: ΔI_{Max} and ΔV_{G} as a function $\varepsilon_{\mathrm{mech}}$. (a) Extracted ΔI_{Max} versus $\varepsilon_{\mathrm{mech}}$ from Fig. 5.5 are reproducible for forward and reverse mechanical sweeps. ΔI_{Max} decreases by more than 80%, from 6 nA to 1 nA, and the related tunnelling-rate change decreases from 40 GHz to 6 GHz (inset). (b) Mechanical strain reduces the resonant ΔV_{G} range for the electromechanical resonance by more than 60%, from 5.5 V to 2 V.

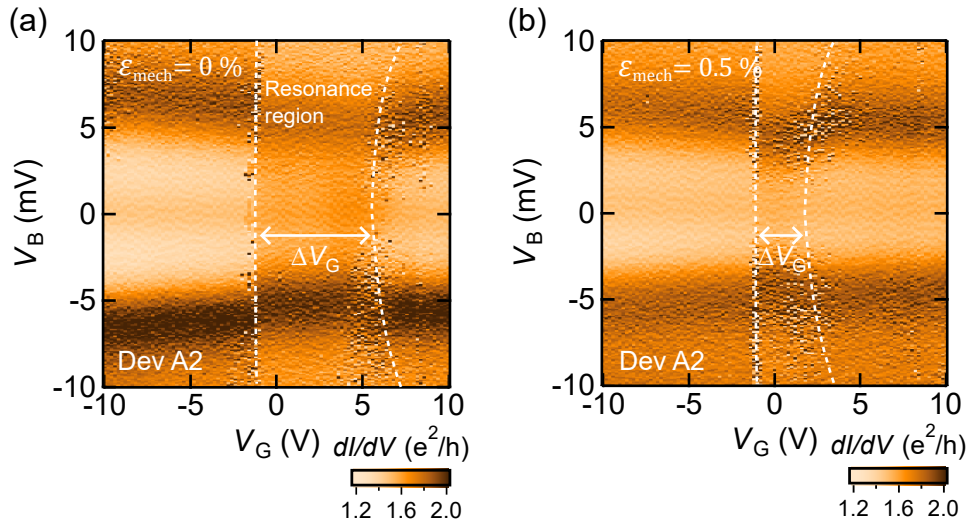

Figure 5.7: Electromechanical resonance in a strained SWCNT-QD. (a) An electromechanical resonance modifies conductance in a SWCNT-QD (Device A2) at $\varepsilon_{\mathrm{mech}} = 0$ %, as indicated by white dashed lines. (b) The resonance region ΔV_{G} becomes narrower at $\varepsilon_{\mathrm{mech}} = 0.5$ %.

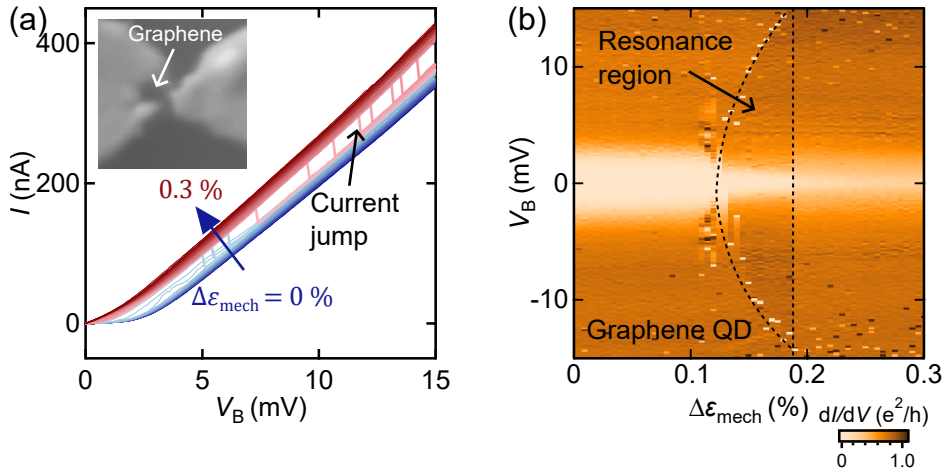

Figure 5.8: Self-oscillations in a strained graphene QD. (a) An electro-mechanical resonance in a graphene QD (inset) leads to reproducible current jumps in the I–V_{B} data under various strains. (b) The white dashed lines indicate the resonance region. The x-axis is $\Delta\varepsilon_{\mathrm{mech}}$, demonstrating the strain tunability of the resonance.

in panel (b), where the resonance region is indicated by the black dashed line. This region exhibits a similar shape (one straight boundary and one parabolic boundary) to that in Fig. 5.7, demonstrating the analogous effects of mechanical strain and gate voltage.

In this section, we reported that mechanical strain modifies the electromechanical resonances we observed in SWCNT and graphene QD devices. We showed that with a 0.5 % strain change, the resonant current change ΔI_{Max} decreased by over 80 %, and the width of the resonance region ΔV_{G} decreases by more than 60 % in a SWCNT-QD device. We observed a similar mechanical control of electromechanical coupling in a graphene QD. Further data analysis will be carried out by my colleagues. This work opens new opportunities in the field of time-dependent QTS, where oscillators create time dependent scalar and vector potentials from strain.

Chapter 6

Conclusions and Outlook

We first developed an applied theoretical model to study quantum transport straintronics (QTS) in uniaxially strained quasimetallic SWCNT transistors. Mechanical strain allowed us to tune the Hamiltonian in the channel through strain-induced scalar and vector potentials. We demonstrated that the propagation angle and quantum phase of charge carriers can be controlled purely by mechanical strain. This theoretical work opens opportunities to include quantitative quantum transport strain effects in the toolbox of quantum technologies based on two-dimensional materials and their nanotubes.

We then fabricated suspended SWCNT-QD transistors that enable both quantum transport measurements and in-situ mechanical strain control. QTS data from these SWCNT devices showed that the charge states of the QDs are tunable via strain. This mechanical gating effect agreed with our QTS theory and arises from quantitatively predictable strain-induced scalar and vector potentials. This added experimental mechanical degree of doping control in QD electronics could find applications in nanotube-based qubits and quantum devices and provide a reliable means to tune single-molecule electronic devices.

We also made transport measurements in strained graphene transistors. We demonstrated the impact of strain-induced scalar and vector potentials on charge conductance. The scalar potential shifted and tuned the work function of the graphene channels by up to 25 meV. Vector potentials suppressed the ballistic conductance by up to 30 % and controlled the quantum interferences in the channel. Finally, we showed how mechanical strain tunes electro-mechanical resonances in SWCNT and graphene-QDs. With only 0.5 % strain, we could modify by more than 80 % the resonance current and reduce by over 60 % the V_{G} range where the electromechanical resonance occurred. These works open new opportunities to harness quantitative strain effects in two-dimensional-material quantum transport and in low-dimensional quantum oscillators.

In this chapter, we first summarize the main results presented in the previous chapters. We then discuss possible technical improvements and potential future research directions for QTS in SWCNTs and graphene.

6.1 Main results

Quantum transport straintronics aims to control the system's Hamiltonian via mechanical strain and electrostatic potentials, to add new opportunities in quantum electronics. SWCNTs are ideal systems for QTS because of their absence of edge order, single transport mode, distinct mechanical properties and strong electromechanical coupling. Below we discuss the main results of our research in QTS in SWCNTs.

We start by modelling SWCNT transport behaviors under uniaxial strain. Unlike graphene devices, they have 1D quantized band structure, not negligible quantum capacitances, different strain-dependent Fermi energy vs V_{G} relationship, larger experimentally available strain range, and different shape aspect ratios. After taking into account these differences, we adapted an applied model for ballistic transport in strained SWCNTs from an existing model for ballistic transport in strained graphene. Figure 6.1(a) presents the QTS platform of our model. A push screw bends the substrate, applying mechanical strain to the suspended SWCNT channel. With Au clamps acting as cantilevers, the maximum mechanical strain could reach up to 7% for a 50 nm long SWCNT channel. Strain modifies the Hamiltonian in the channel via a scalar potential $\Delta\phi_{\varepsilon}$ and vector potentials $\boldsymbol{A}_{\mathrm{hop}}$, as shown in Fig.6.1(b). We found that these potentials can tune the propagation angle Θ of charge carriers and Fig. 6.1(c) shows that the dependence of Θ on $\varepsilon_{\mathrm{total}}$ varies with the SWCNT's chirality. By solving for transmission using longitudinal boundary conditions, we calculated the conductance G over a wide range of $\varepsilon_{\mathrm{mech}}$ and V_{G}. We observed a mechanical Aharbonov-Bohm effect, i.e. strain-tunable quantum interferences, as shown in panel (d). For instance, a full 2π phase shift could be induced in a (12,9) tube with a 0.7 % strain change.

We then fabricated suspended SWCNT-QD transistors suitable for our QTS platform (Chapter 3). Figure 6.2(a) shows the suspended SWCNT-under-gold breakjunction of Device A1 before electromigration. The suspension length is $L_{\mathrm{sus}} = 650$ nm. Figure 6.2(b) presents a zoomed-in view of the breakjunction in (a) after electromigration. The top-left inset shows the electromigration procedure for Device A1, and the top-right inset displays the small-scale SEM image of the naked SWCNT channel created during this process. The channel lengths of our devices are approximately 30 nm.

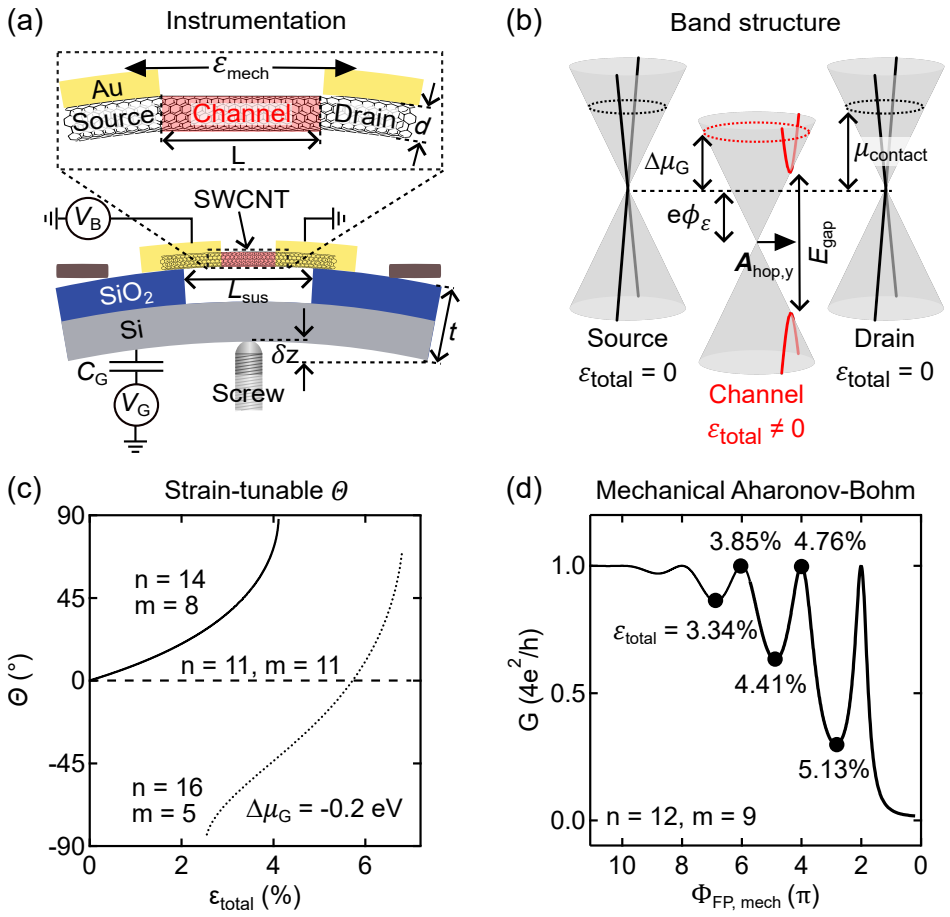

Figure 6.1: An applied theoretical model for quantum transport in strained SWCNTs. (a) Side-view diagram of the QTS platform described in our model. (b) Band structure in the source, channel, and drain sections of a strained quasi-metallic nanotube. (c) Strain controls the propagation angle Θ in all quasi-metallic (e.g. $n = 14,\ m = 8$) and semi-conducting (e.g. $n = 16,\ m = 5$) SWCNTs. However, Θ is independent from ε_{total} in armchair tubes (e.g. $n = 11,\ m = 11$). (d) Data extracted at $\Delta\mu_G = -0.2$ eV for a quasi-metallic SWCNT ($n = 12,\ m = 9$) show that the G interferences are fully tunable using only the mechanical potentials.

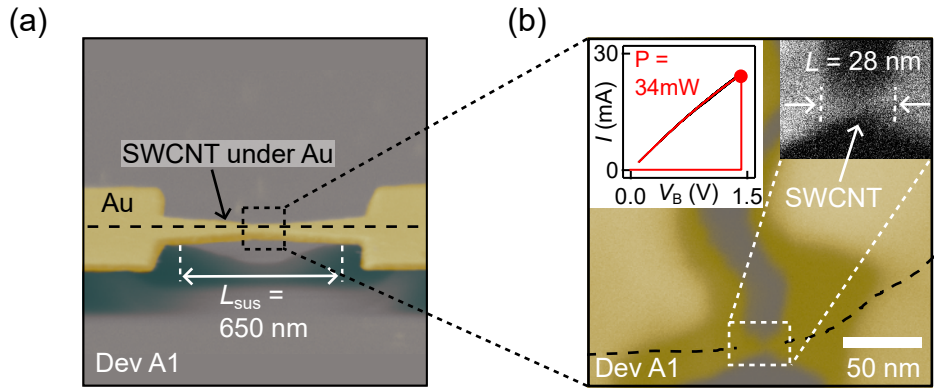

Figure 6.2: A suspended SWCNT quantum dot for QTS. (a) Tilted-SEM image (80°) of the suspended SWCNT-under-gold breakjunction in Device A1 (before electromigration). The suspension length is L_{sus} = 650 nm. (b) Zoom-in view of the breakjunction in (a) after electromigration. The top left inset shows the electromigration process for Device A1, and the top right inset the small scale SEM image of the naked-SWCNT channel created during this process.

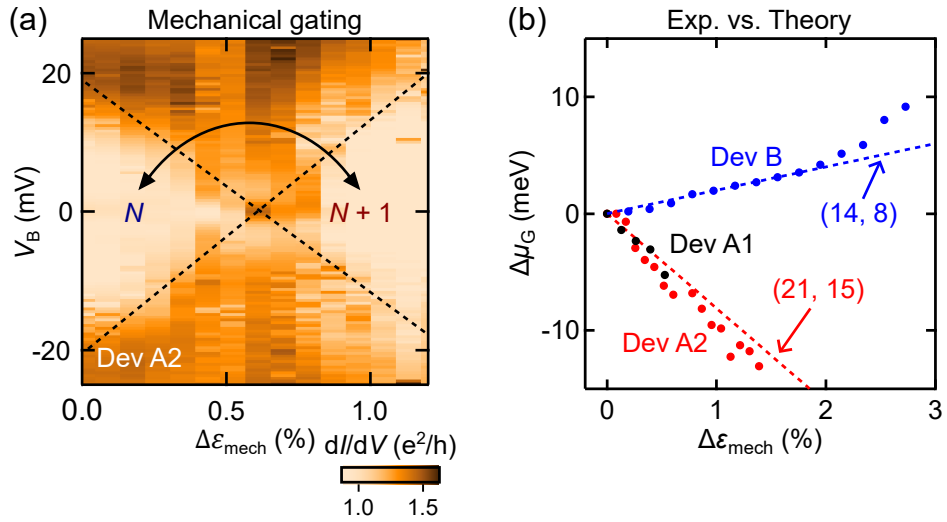

Figure 6.3: Mechanical gating and Fermi energy tuning of SWCNT-QDs. (a) dI/dV–V_B–$\Delta\varepsilon_{mech}$ data from Device A2 showing a charge-state transition induced by mechanical strain. (b) Measured $\Delta\mu_G$ vs $\Delta\varepsilon_{mech}$ in Devices A1, A2, and B. The dashed lines are theoretical calculations.

The V_G dependence of the QDs was weak due to the short channel length, and the screening from the thick electromigrated gold film surrounding the channel. However, mechanical strain provides an additional means of gating charge transport in these SWCNT QDs. The 2D map of dI/dV versus V_B and $\Delta\varepsilon_{mech}$ in Fig. 6.3(a) demonstrates that mechanical strain can add or remove a single electron from the SWCNT channel. This behavior was observed in all three SWCNT-QD transistors studied. By extracting the Fermi level change $\Delta\mu_G$ and capacitances at varying $\Delta\varepsilon_{mech}$, we found that this mechanical-gating effect does not originate from capacitance changes, as in most molecular transistors, but rather from the quantitatively predictable band-structure modification induced by strain-generated scalar and vector potentials. Devices fabricated on the same SWCNT (Devices A1 and A2) exhibited the same dependence of $\Delta\mu_G$ on $\Delta\varepsilon_{mech}$, whereas Device B, made from a different SWCNT, showed a distinct linear dependence, as illustrated in Fig. 6.3(b). These data agreed with the calculations based on our QTS theory (dashed lines).

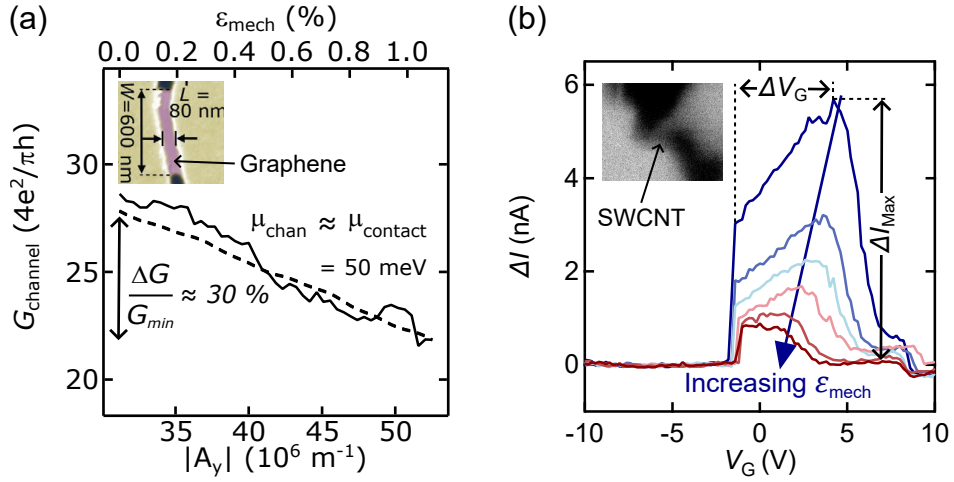

Figure 6.4: Strain-tunable ballistic conductance in graphene and electromechanical coupling in SWCNT QDs. (a) The strain-induced vector potential $|A_y|$ suppressed graphene's ballistic conductance by up to 30 % in our devices. Inset: device geometry. (b) Mechanical strain reduced electromechanical coupling in our SWCNT oscillators, decreasing the maximum current jump ΔI_{Max} and the gate-voltage width ΔV_G of the resonance.

Lastly, we discussed the mechanical control of quantum transport in ballistic graphene and the electron-mechanical coupling in SWCNT and graphene resonators. In graphene QTS, we demonstrated that the strain-induced scalar potential can modify graphene's work function by up to 25 meV, and the strain-induced vector potential can suppress its conductance by up to 30 %, as shown in Fig. 6.4(a). Mechanical strain can also control the quantum interferences of charge carriers in the graphene channel. In addition, we observed strain-tunable

electromechanical resonances in SWCNT QDs. Mechanical strain could widely control both the coupling strength g and the window ΔV_{G} where the electromechanical resonances are observed. Figure 6.4(b) shows that under 0.5% mechanical strain, the current change ΔI_{Max} associated with the onset of the electromechanical resonances decreases by more than 80%, from 6 nA to 1 nA, and the strong coupling window ΔV_{G} decreases by more than 60%, from 5.5 V to 2 V. A similar transport behavior was observed in strained graphene QDs, and further data analysis will be carried out by my colleagues.

Our work opens new opportunities to harness quantitative strain effects in the quantum transport of low-dimensional materials and could find applications in qubits, oscillators and other quantum devices.

6.2 Outlook for QTS in SWCNTs

First, to extend and improve the work reported above, we could increase the breaking power during electromigration and reduce the thickness of the electromigrated Au film to create longer channels and minimize electrostatic screening. This would allow stronger electrostatic V_{G} dependence. The additional spectroscopy range (E_{F} tuning) would provide more information about the SWCNT Hamiltonian (e.g., bandgap, chirality) and enable exploration of additional physical phenomena, such as strain-tunable Kondo effects [99]. Since mechanical strain can tune the tunnelling rate by modifying the tunnel barriers at the source/drain–channel interfaces, it can tune the Kondo temperature in a SWCNT QD, $T_K = (\sqrt{\Gamma E_C}/2), e^{\pi\mu(\mu+E_C)/\Gamma E_C}$, where Γ is the total tunnelling rate, E_C is the charging energy, and μ is the electrochemical potential [99, 107]. We could also characterize the SWCNT chirality using transmission electron microscopy (TEM) [48], or use SWCNTs with known chirality obtained from selective growth [108, 109]. This would eliminate chirality uncertainty and enable the design of devices with known doping and phase control through mechanical strain.

Another research direction would be QTS for qNEMS (quantum nano-electromechanical systems). We could first develop an applied model for QTS in SWCNT and graphene NEMS considering the time-dependent oscillations which generate time-dependent strain-induced gauge potentials. This would allow us to quantitatively describe qNEMS transport data and study electron-vibron coupling and energy dissipation in qNEMS. We could then conduct the QTS experiment by including ac actuation of the gate electrode. These strain-tunable resonators could achieve widely tunable frequencies and non-linearities [110, 111] and find applications in extremely sensitive mass or force sensing.

Bibliography

[1] A. H. Castro Neto, F. Guinea, N. M. R. Peres, K. S. Novoselov, and A. K. Geim, *The electronic properties of graphene*, Rev. Mod. Phys. **81**, 109 (2009).

[2] D. Rhodes, S. H. Chae, R. Ribeiro-Palau, and J. Hone, *Disorder in van der Waals heterostructures of 2D materials*, Nat. Mater. **18**, 541 (2019).

[3] L. Banszerus et al., *Ballistic Transport Exceeding 28 μm in CVD Grown Graphene*, Nano Lett. **16**, 1387 (2016).

[4] N. P. Kazmierczak et al., *Strain fields in twisted bilayer graphene*, Nat. Mater. **20**, 956 (2021).

[5] A. Alfieri, S. B. Anantharaman, H. Q. Zhang, and D. Jariwala, *Nanomaterials for Quantum Information Science and Engineering*, Adv. Mater. **35**, 2109621 (2023).

[6] R. Tormo-Queralt et al., *Novel Nanotube Multiquantum Dot Devices*, Nano Lett. **22**, 8541 (2022).

[7] M. Mergenthaler et al., *Circuit Quantum Electrodynamics with Carbon-Nanotube-Based Superconducting Quantum Circuits*, Phys. Rev. Appl. **15**, 064050 (2021).

[8] L. Banszerus et al., *Pulsed-gate spectroscopy of single-electron spin states in bilayer graphene quantum dots*, Phys. Rev. B **103**, L081404 (2021).

[9] I. Khivrich and S. Ilani, *Atomic-like charge qubit in a carbon nanotube enabling electric and magnetic field nano-sensing*, Nat. Commun. **11**, 2299 (2020).

[10] X. L. Liu and M. C. Hersam, *2D materials for quantum information science*, Nat. Rev. Mater. **4**, 669 (2019).

[11] J. S. Chen et al., *Long-lived electronic spin qubits in single-walled carbon nanotubes*, Nat. Commun. **14**, 848 (2023).

[12] A. Pal et al., *Quantum-Engineered Devices Based on 2D Materials for Next-Generation Information Processing and Storage*, Adv. Mater. **35**, 2109894 (2023).

[13] S. F. Wu et al., *Observation of the quantum spin Hall effect up to 100 kelvin in a monolayer crystal*, Science **359**, 76 (2018).

[14] P. Z. Hanakata, A. S. Rodin, H. S. Park, D. K. Campbell, and A. H. C. Neto, *Strain-induced gauge and Rashba fields in ferroelectric Rashba lead chalcogenide PbX monolayers (X = S, Se, Te)*, Phys. Rev. B **97**, 235312 (2018).

[15] A. Molle et al., *Buckled two-dimensional Xene sheets*, Nat. Mater. **16**, 163 (2017).

[16] F. Kuemmeth, S. Ilani, D. C. Ralph, and P. L. McEuen, *Coupling of spin and orbital motion of electrons in carbon nanotubes*, Nature **452**, 448 (2008).

[17] S. Y. Li, Y. Su, Y. N. Ren, and L. He, *Valley Polarization and Inversion in Strained Graphene via Pseudo-Landau Levels, Valley Splitting of Real Landau Levels, and Confined States*, Phys. Rev. Lett. **124**, 106802 (2020).

[18] M. Settnes, J. H. Garcia, and S. Roche, *Valley-polarized quantum transport generated by gauge fields in graphene*, 2D Mater. **4**, 031006 (2017).

[19] J. R. Schaibley et al., *Valleytronics in 2D materials*, Nat. Rev. Mater. **1**, 16055 (2016).

[20] F. Guinea, M. I. Katsnelson, and A. K. Geim, *Energy gaps and a zero-field quantum Hall effect in graphene by strain engineering*, Nat. Phys. **6**, 30 (2010).

[21] J. M. Kim et al., *Strain Engineering of Low-Dimensional Materials for Emerging Quantum Phenomena and Functionalities*, Adv. Mater. **35**, 2107362 (2023).

[22] M. Kapfer et al., *Programming twist angle and strain profiles in 2D materials*, Science **381**, 677 (2023).

[23] H. Khanjani and A. G. Moghaddam, *Anomalous quantum interference effects in graphene SNS junctions due to strain-induced gauge fields*, Phys. Rev. B **98**, 195421 (2018).

[24] L. Zhang et al., *Steady-state Peierls transition in nanotube quantum simulator*, npj Quantum Inf. **9**, 7 (2023).

[25] P. A. Pantaleón, T. Low, and F. Guinea, *Tunable large Berry dipole in strained twisted bilayer graphene*, Phys. Rev. B **103**, 205403 (2021).

[26] L. J. Du et al., *Engineering symmetry breaking in 2D layered materials*, Nat. Rev. Phys. **3**, 193 (2021).

[27] C. Moulsdale, A. Knothe, and V. Fal'ko, *Engineering of the topological magnetic moment of electrons in bilayer graphene using strain and electrical bias*, Phys. Rev. B **101**, 085118 (2020).

[28] J. Mutch et al., *Evidence for a strain-tuned topological phase transition in ZrTe5*, Sci. Adv. **5**, eaav9771 (2019).

[29] Y. Efroni, S. Ilani, and E. Berg, *Topological Transitions and Fractional Charges Induced by Strain and a Magnetic Field in Carbon Nanotubes*, Phys. Rev. Lett. **119**, 147704 (2017).

[30] J. Cenker et al., *Reversible strain-induced magnetic phase transition in a van der Waals magnet*, Nat. Nanotechnol. **17**, 256 (2022).

[31] T. X. Li et al., *Pressure-controlled interlayer magnetism in atomically thin CrI*, Nat. Mater. **18**, 1303 (2019).

[32] K. S. Burch, D. Mandrus, and J. G. Park, *Magnetism in two-dimensional van der Waals materials*, Nature **563**, 47 (2018).

[33] B. Amorim et al., *Novel effects of strains in graphene and other two dimensional materials*, Phys. Rep. **617**, 1 (2016).

[34] G. G. Naumis, S. Barraza-Lopez, M. Oliva-Leyva, and H. Terrones, *Electronic and optical properties of strained graphene and other strained 2D materials: a review*, Rep. Prog. Phys. **80**, 096501 (2017).

[35] F. Miao, S. J. Liang, and B. Cheng, *Straintronics with van der Waals materials*, npj Quantum Mater. **6**, 59 (2021).

[36] A. C. McRae, G. Wei, and A. R. Champagne, *Graphene Quantum Strain Transistors*, Phys. Rev. Appl. **11**, 054019 (2019).

[37] F. Evers, R. Korytár, S. Tewari, and J. M. van Ruitenbeek, *Advances and challenges in single-molecule electron transport*, Rev. Mod. Phys. **92**, 035001 (2020).

[38] L. Huang, G. Wei, and A. R. Champagne, *Quantum transport straintronics and mechanical Aharonov-Bohm effect in quasimetallic single-wall carbon nanotubes*, Phys. Rev. Appl. **23**, 014030 (2025).

[39] L. Yang, M. P. Anantram, J. Han, and J. P. Lu, *Band-gap change of carbon nanotubes: Effect of small uniaxial and torsional strain*, Phys. Rev. B **60**, 13874 (1999).

[40] L. Huder et al., *Electronic Spectrum of Twisted Graphene Layers under Heterostrain*, Phys. Rev. Lett. **120**, 156405 (2018).

[41] L.-Z. Yang et al., *Origami-controlled strain engineering of tunable flat bands and correlated states in folded graphene*, Phys. Rev. Mater. **6**, L041001 (2022).

[42] E. D. Minot et al., *Tuning Carbon Nanotube Band Gaps with Strain*, Phys. Rev. Lett. **90**, 156401 (2003).

[43] L. Wang et al., *Global strain-induced scalar potential in graphene devices*, Commun. Phys. **4**, 147 (2021).

[44] H. Wang et al., *Carbon Nanotube Intramolecular Junction Photodetector Via Strain Engineering*, Small **21**, 2502735 (2025).

[45] J. Cenker et al., *Engineering Robust Strain Transmission in van der Waals Heterostructure Devices*, Nano Lett. **25**, 4512 (2025).

[46] A. L. Kitt, V. M. Pereira, A. K. Swan, and B. B. Goldberg, *Lattice-corrected strain-induced vector potentials in graphene*, Phys. Rev. B **85**, 115432 (2012).

[47] J.-C. Charlier, X. Blase, and S. Roche, *Electronic and transport properties of nanotubes*, Rev. Mod. Phys. **79**, 677 (2007).

[48] E. A. Laird et al., *Quantum transport in carbon nanotubes*, Rev. Mod. Phys. **87**, 703 (2015).

[49] A. C. McRae, *Graphene Quantum Strain Transistors and Two-in-One Carbon Nanotube Quantum Transistors*, PhD Thesis, Concordia University (2018).

[50] J. Tworzydlo, B. Trauzettel, M. Titov, A. Rycerz, and C. W. Beenakker, *Sub-Poissonian shot noise in graphene*, Phys. Rev. Lett. **96**, 246802 (2006).

[51] M. M. Fogler, F. Guinea, and M. I. Katsnelson, *Pseudomagnetic fields and ballistic transport in a suspended graphene sheet*, Phys. Rev. Lett. **101**, 226804 (2008).

[52] A. C. McRae et al., *Mechanical Control of Quantum Transport in Graphene*, Adv. Mater. **36**, 2313629 (2024).

[53] Y. Hou et al., *Tuning instability in suspended monolayer 2D materials*, Nat. Commun. **15**, 4033 (2024).

[54] Q. W. An et al., *Direct growth of single-chiral-angle tungsten disulfide nanotubes using gold nanoparticle catalysts*, Nat. Mater. **23**, 347 (2024).

[55] R. T. K. Schock et al., *Non-Destructive Low-Temperature Contacts to MoS2 Nanoribbon and Nanotube Quantum Dots*, Adv. Mater. **35**, 2209333 (2023).

[56] F. Shayeganfar, *Strain engineering of electronic properties and anomalous valley hall conductivity of transition metal dichalcogenide nanoribbons*, Sci. Rep. **12**, 11285 (2022).

[57] K. Tomioka, M. Yoshimura, and T. Fukui, *A III-V nanowire channel on silicon for high-performance vertical transistors*, Nature **488**, 189 (2012).

[58] L. Banszerus et al., *Ballistic Transport Exceeding 28 mum in CVD Grown Graphene*, Nano Lett. **16**, 1387 (2016).

[59] A. S. Mayorov et al., *Micrometer-Scale Ballistic Transport in Encapsulated Graphene at Room Temperature*, Nano Lett. **11**, 2396 (2011).

[60] R. Arenal, O. Stephan, J. L. Cochon, and A. Loiseau, *Root-growth mechanism for single-walled boron nitride nanotubes in laser vaporization technique*, J. Am. Chem. Soc. **129**, 16183 (2007).

[61] M. Huang et al., *Direct Measurement of Strain-Induced Changes in the Band Structure of Carbon Nanotubes*, Phys. Rev. Lett. **100**, 136803 (2008).

[62] E. Mariani and F. von Oppen, *Electron-vibron coupling in suspended carbon nanotube quantum dots*, Phys. Rev. B **80**, 155411 (2009).

[63] A. C. McRae, V. Tayari, J. M. Porter, and A. R. Champagne, *Giant electron-hole transport asymmetry in ultra-short quantum transistors*, Nat. Commun. **8**, 15491 (2017).

[64] M. Hasegawa and K. Nishidate, *Transfer doping of a metallic carbon nanotube and graphene on metal surfaces (vol 83, 155435, 2011)*, Phys. Rev. B **84**, 155435 (2011).

[65] G. Giovannetti et al., *Doping graphene with metal contacts*, Phys. Rev. Lett. **101**, 026803 (2008).

[66] S. Heinze et al., *Carbon nanotubes as Schottky barrier transistors*, Phys. Rev. Lett. **89**, 106801 (2002).

[67] S.-M. Choi, S.-H. Jhi, and Y.-W. Son, *Effects of strain on electronic properties of graphene*, Phys. Rev. B **81**, 081407 (2010).

[68] L. Yang and J. Han, *Electronic Structure of Deformed Carbon Nanotubes*, Phys. Rev. Lett. **85**, 154 (2000).

[69] F. M. D. Pellegrino, G. G. N. Angilella, and R. Pucci, *Transport properties of graphene across strain-induced nonuniform velocity profiles*, Phys. Rev. B **84**, 195404 (2011).

[70] A. van Oudenaarden, M. H. Devoret, Y. V. Nazarov, and J. E. Mooij, *Magneto-electric Aharonov-Bohm effect in metal rings*, Nature **391**, 768 (1998).

[71] Y. Aharonov and D. Bohm, *Significance of Electromagnetic Potentials in the Quantum Theory*, Phys. Rev. **115**, 485 (1959).

[72] N. Nemec, D. Tomanek, and G. Cuniberti, *Contact dependence of carrier injection in carbon nanotubes: An ab initio study*, Phys. Rev. Lett. **96**, 076802 (2006).

[73] A. R. Champagne, A. N. Pasupathy, and D. C. Ralph, *Mechanically adjustable and electrically gated single-molecule transistors*, Nano Lett. **5**, 305 (2005).

[74] T. Ando, *Theory of Electronic States and Transport in Carbon Nanotubes*, J. Phys. Soc. Jpn. **74**, 777 (2005).

[75] E. B. Kolomeisky, H. Zaidi, and J. P. Straley, *Interplay of Aharonov-Bohm, chirality, and aspect-ratio effects in the axial conductance of a nanotube*, Phys. Rev. B **85**, 073404 (2012).

[76] S. Ilani, L. A. K. Donev, M. Kindermann, and P. L. McEuen, *Measurement of the quantum capacitance of interacting electrons in carbon nanotubes*, Nat. Phys. **2**, 687 (2006).

[77] D. Yoon, Y. W. Son, and H. Cheong, *Negative Thermal Expansion Coefficient of Graphene Measured by Raman Spectroscopy*, Nano Lett. **11**, 3227 (2011).

[78] F. C. Nix and D. MacNair, *The Thermal Expansion of Pure Metals: Copper, Gold, Aluminum, Nickel, and Iron*, Phys. Rev. **60**, 597 (1941).

[79] J. O. Island, V. Tayari, A. C. McRae, and A. R. Champagne, *Few-Hundred GHz Carbon Nanotube Nanoelectromechanical Systems (NEMS)*, Nano Lett. **12**, 4564 (2012).

[80] V. Sazonova, *A Tunable Carbon Nanotube Resonator*, PhD Thesis, Cornell University (2006).

[81] T. Yamada et al., *Size-selective growth of double-walled carbon nanotube forests from engineered iron catalysts*, Nat. Nanotechnol. **1**, 131 (2006).

[82] W. Liang et al., *Fabry - Perot interference in a nanotube electron waveguide*, Nature **411**, 665 (2001).

[83] N. Lotfizadeh, M. J. Senger, D. R. McCulley, E. D. Minot, and V. V. Deshpande, *Quantum Interferences in Ultraclean Carbon Nanotubes*, Phys. Rev. Lett. **126**, 216802 (2021).

[84] M. Oliva-Leyva and C. M. Wang, *Low-energy theory for strained graphene: an approach up to second-order in the strain tensor*, J. Phys-Condens. Mat. **29** (2017).

[85] J. O. Island, V. Tayari, S. Yigen, A. C. McRae, and A. R. Champagne, *Ultra-short suspended single-wall carbon nanotube transistors*, Appl. Phys. Lett. **99**, 243106 (2011).

[86] M. Mergenthaler et al., *Radio-frequency characterization of a supercurrent transistor made of a carbon nanotube*, Mater. Quantum Technol. **1**, 035003 (2021).

[87] D. Szombathy et al., *Collective tunneling of a Wigner necklace in carbon nanotubes*, Phys. Rev. B **109**, 245139 (2024).

[88] L. Anderson, A. Cheng, T. Taniguchi, K. Watanabe, and P. Kim, *Coulomb Drag between a Carbon Nanotube and Monolayer Graphene*, Phys. Rev. Lett. **127**, 257701 (2021).

[89] M. Kögl et al., *Moire straintronics: a universal platform for reconfigurable quantum materials*, Npj 2d Mater. Appl. **7**, 32 (2023).

[90] A. McRae, *Ultra-short carbon nanotube quantum dot transistors*, MSc Thesis, Concordia University **MSc** (2013).

[91] L. Huang, *Quantum Transport in Strained Single-wall Carbon Nanotube Transistors*, MSc Thesis, Concordia University (2021).

[92] R. Alizadegan, A. D. Liao, F. Xiong, E. Pop, and K. J. Hsia, *Effects of tip-nanotube interactions on atomic force microscopy imaging of carbon nanotubes*, Nano Res. **5**, 235 (2012).

[93] D. Vobornik, M. Chen, S. Zou, and G. P. Lopinski, *Measuring the Diameter of Single-Wall Carbon Nanotubes Using AFM*, Nanomaterials **13**, 477 (2023).

[94] F. A. Chaves, D. Jiménez, A. W. Cummings, and S. Roche, *Physical model of the contact resistivity of metal-graphene junctions*, J. Appl. Phys. **115**, 164513 (2014).

[95] C. S. Boland, Y. Sun, and D. G. Papageorgiou, *Bandgap Engineering of 2D Materials toward High-Performing Straintronics*, Nano Lett. **24**, 12722 (2024).

[96] S. van der Poel et al., *Mechanoelectric sensitivity reveals destructive quantum interference in single-molecule junctions*, Nat. Commun. **15**, 10097 (2024).

[97] P. Jarillo-Herrero, S. Sapmaz, C. Dekker, L. P. Kouwenhoven, and H. S. J. van der Zant, *Electron-hole symmetry in a semiconducting carbon nanotube quantum dot*, Nature **429**, 389 (2004).

[98] S. Caneva et al., *A Mechanically Tunable Quantum Dot in a Graphene Break Junction*, Nano Lett. **20**, 4924 (2020).

[99] J. J. Parks et al., *Tuning the Kondo Effect with a Mechanically Controllable Break Junction*, Phys. Rev. Lett. **99**, 026601 (2007).

[100] D. Grassano et al., *Work function, deformation potential, and collapse of Landau levels in strained graphene and silicene*, Phys. Rev. B **101**, 245115 (2020).

[101] C. Samanta et al., *Nonlinear nanomechanical resonators approaching the quantum ground state*, Nat. Phys. **19**, 1340 (2023).

[102] S. Rechnitz, T. Tabachnik, M. Shlafman, S. Shlafman, and Y. E. Yaish, *Mode coupling bi-stability and spectral broadening in buckled carbon nanotube mechanical resonators*, Nat. Commun. **13**, 5900 (2022).

[103] S. Rechnitz, T. Tabachnik, S. Shlafman, M. Shlafman, and Y. E. Yaish, *DC Signature of Snap-through Bistability in Carbon Nanotube Mechanical Resonators*, Nano Lett. **22**, 7304 (2022).

[104] J. Tabanera-Bravo et al., *Stability of long-sustained oscillations induced by electron tunneling*, Phys. Rev. Research **6** (2024).

[105] Y. Ying et al., *Sliding nanomechanical resonators*, Nat. Commun. **13**, 6392 (2022).

[106] B. Lassagne, Y. Tarakanov, J. Kinaret, D. Garcia-Sanchez, and A. Bachtold, *Coupling Mechanics to Charge Transport in Carbon Nanotube Mechanical Resonators*, Science **325**, 1107 (2009).

[107] J. Park, *Electron Transport in Single Molecule Transistors*, PhD Thesis, University of California (2003).

[108] Y. Li et al., *An efficient approach toward production of near-zigzag single-chirality carbon nanotubes*, Sci. Adv. **10**, eadn6519 (2024).

[109] S. Shiina et al., *Synthesis of Ultrahigh-Purity (6,5) Carbon Nanotubes Using a Trimetallic Catalyst*, ACS Nano **18**, 23979 (2024).

[110] L. Xie et al., *Carbon-nanomaterial-enabled terahertz technology*, Nat. Rev. Phys. **7**, 487 (2025).

[111] B. Xu et al., *Nanomechanical Resonators: Toward Atomic Scale*, ACS Nano **16**, 15545 (2022).